INFORMATION TO USERS

This manuscript has been reproduced from the microfilm master. UMI films the text directly from the original or copy submitted. Thus, some thesis and dissertation copies are in typewriter face, while others may be from any type of computer printer.

The quality of this reproduction is dependent upon the quality of the copy submitted. Broken or indistinct print, colored or poor quality illustrations and photographs, print bleedthrough, substandard margins, and improper alignment can adversely affect reproduction.

In the unlikely event that the author did not send UMI a complete manuscript and there are missing pages, these will be noted. Also, if unauthorized copyright material had to be removed, a note will indicate the deletion.

Oversize materials (e.g., maps, drawings, charts) are reproduced by sectioning the original, beginning at the upper left-hand corner and continuing from left to right in equal sections with small overlaps. Each original is also photographed in one exposure and is included in reduced form at the back of the book.

Photographs included in the original manuscript have been reproduced xerographically in this copy. Higher quality 6" x 9" black and white photographic prints are available for any photographs or illustrations appearing in this copy for an additional charge. Contact UMI directly to order.

UMI

A Bell & Howell Information Company
300 North Zeeb Road, Ann Arbor MI 48106-1346 USA
313/761-4700 800/521-0600

MOLECULAR BEAM EPITAXY GROWTH AND CHARACTERIZATION OF TWO-SIX MATERIALS FOR VISIBLE SEMICONDUCTOR LASERS

by

Linfei Zeng

A dissertation submitted to the Graduate Faculty in Engineering in partial fulfillment of the requirements for the degree of Doctor of Philosophy, The City University of New York.

1998

This manuscript has been read and accepted for the Graduate Faculty in Engineering in satisfaction of the dissertation requirement for the degree of Doctor of Philosophy.

4/28/98
Date

Chair of Examining Committee
Prof. Kai Shum (Advisor)

4/28/98
Date

Prof. Maria C. Tamargo (Co-Advisor)

4/29/98
Date

Executive Officer

Prof. Ying Chih Chen (Hunter College of CUNY)

Prof. Roger Dorsinville (City College of CUNY)

Dr. John Petruzzello (Philips Laboratory)

Prof. Gerald Subak-Sharp (City College of CUNY)
Supervisory Committee

THE CITY UNIVERSITY OF NEW YORK

ABSTRACT

MOLECULAR BEAM EPITAXY GROWTH AND CHARACTERIZATION OF TWO-SIX MATERIALS FOR VISIBLE SEMICONDUCTOR LASERS

by

Linfei Zeng

Thesis Advisors: Prof. Maria C. Tamargo

Prof. Kai Shum

This thesis proposes the molecular beam epitaxy (MBE) growth and characterization of a new $Zn_xCd_yMg_{(1-x-y)}Se$ based semiconductor materials system on InP substrates for visible light emitting diodes (LED) and lasers. The growth conditions for lattice-matched $Zn_xCd_yMg_{(1-x-y)}Se$ layers with the desired bandgap have been established and optimized. A chemical etching technique to measure the defect density of $Zn_xCd_yMg_{(1-x-y)}Se$ materials has been established. The accuracy of this method for revealing stacking faults and dislocations was verified by plan-view TEM. Using the techniques such as III-V buffer layer, Zn-irradiation, low-temperature growth, ZnCdSe

interfacial layer and growth interruption to improve the quality of the interface of III-V and II-VI, the material quality of $Zn_xCd_yMg_{(1-x-y)}Se$ has been improved dramatically. Defect density has been reduced from 10^{10} cm^{-2} to ~ 5×10^4 cm^{-2}. The properties of this material system such as the quality and strain state in the epilayer, the dependence of bandgap on temperature, and the band offset have been studied by using double crystal x-ray diffraction, photoluminescence and capacitance voltage measurements.

The ZnCdSe/ZnCdMgSe based quantum well (QW) structures have been grown and studied. Optically pumped lasing with emission range from red to blue has been obtained from ZnCdSe/ZnCdMgSe based separate-confinement single QW laser structures. The results demonstrate the potential for these materials as integrated full color display devices. Preliminary studies of the degradation behavior of ZnCdSe/ZnCdMgSe QW were performed. No dark line defects (DLDs) were observed during the degradation.

A very strong room temperature differential negative resistance behavior was observed from $Al/Zn_{0.61}Cd_{0.39}Se/n^+$-InP devices, which is useful in millimeter-wave applications. We also found that these devices can be set to either in highly conductive or nonconductive state within a given probing voltage region, which can be used as nonvolatile memories.

ACKNOWLEDGMENTS

This thesis would not be completed without the guidance of my advisor Prof. Maria C. Tamargo, who provides encouragement, inspiration, and, most important, an excellent physical environment in the past four years. I would like to present my deep appreciation to her. I would also like to present my deep appreciation to my advisor Prof. Kai Shum for his invaluable guidance and support.

I am also deeply indebted to Dr. N. Dai, Dr. A. Cavus and Dr. B. X. Yang, from whom I have learned many experimental skills and gained more knowledge about the growth and characterization. I also want to thank other members in the MBE group, Ms. Y. Y. Luo, Mr. W. Lin, Ms. B. Shewareged, Ms. D. Hunte, Ms. P. Mcwilliams, Mr. A. Elmoumni for their significant assistance.

Many thanks to Dr. E. Snoeks and Dr. L. Zhao in the Philips Laboratories for TEM and initial double crystal x-ray measurements, to Prof. Y. C. Chen and Mr. Y. M. Guo in the Hunter College-CUNY for the manufacturing and characterization of optically pumped lasers, to Prof. Fred

H. Pollak and Dr. J. Z. Wan in the Brooklyn College-CUNY for the AFM measurements, to Dr. L. L. Chao, Ms. Huilin Xing and Prof. S. Cargill in the Lehigh University for the cathodoluminescence measurements, to Prof. J. Zhou, Mr. W. Zhang in the Electrical Engineering Department of CCNY for the C-V and I-V measurements. The support of the National Science Foundation through grants ECS93-20415, ECS97-07213 and HRD-9353488 is gratefully acknowledged.

I am very grateful to my wife, Peijing Zhang, for the support without which I could not concentrate on my research. Finally I want to thank my parents for their support in the last three decades.

CONTENTS

LIST OF TABLES

Chapter 3.

Chapter 4.

Chapter 5.

LIST OF ILLUSTRATIONS

Chapter 1.

Chapter 2.

Chapter 3.

Chapter 4.

Chapter 5.

Chapter 6.

CHAPTER 1

INTRODUCTION

Molecular beam epitaxy (MBE) is an advanced and complex technology to grow semiconductor epilayers. Its implementation and use involve a wide range of research in the fields of physics, chemistry, electrical engineering, and material science. With the ability to control the growth with atomic layer accuracy, it has proven strength in fabricating heterostructure devices, such as IMPATT diodes, modulation doped field effect transistors, optical detectors, light-emitting diodes (LEDs), double heterostructure lasers, quantum well lasers. Today, high quality devices are routinely fabricated in laboratories and factories by MBE. In this work, we will study the MBE growth of a new semiconductor material system $Zn_xCd_yMg_{(1-x-y)}Se$ for LEDs and lasers in the visible range.

Semiconductor lasers and LEDs emitting in the visible range have potential applications in full color displays, high speed laser printing, and high density digital recording.[1,2] Currently, the lasers used in laser printing and digital recording are infrared or red lasers. By reducing the wavelength to blue, the speed of the printing and the density of the recording will increase

about four times.[1] Currently, LED-based full color display panels use LEDs based on different material for the three primary colors (red, green and blue).[3] In order to fabricate integrated systems, it is of interest to find a single material that can be used for the full color range. For the green and blue lasers, most people are working on the ZnSe/GaAs based II-VI material system[4] and the GaN based III-V material system. Although blue LEDs and lasers with projected lifetime of more than 10000 hours[5] have been made from GaN-based materials, the results are limited to a few laboratories and their fabrication is still a subject of much active research. One of the problems with both systems is that the structures can't be grown totally lattice matched. This certainly will affect the behavior of the lasers. Therefore, it is interesting to explore other materials that may be used to design entirely lattice matched structures that also meet the band structure requirements of this complex devices.

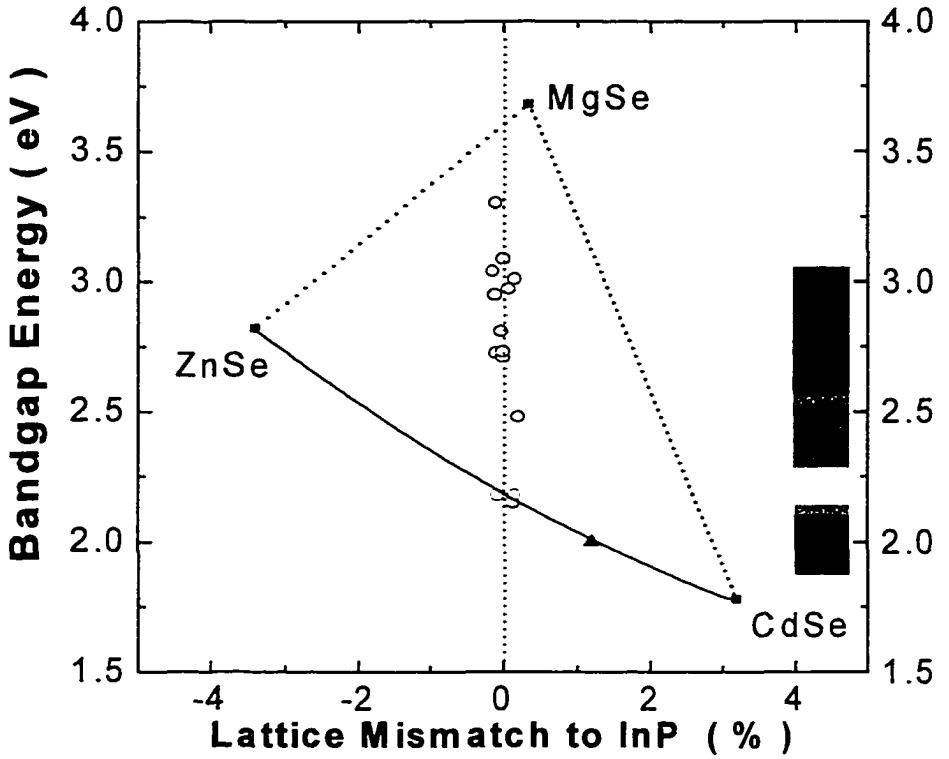

Fig. 1-1. Bandgap versus percent lattice-mismatch to InP for ZnCdMgSe quaternary layers grown on InP substrates.

Wide bandgap $Zn_xCd_yMg_{(1-x-y)}Se$ material system lattice-matched to InP is a new quaternary materials system that can be used in the design and fabrication of red, green and blue (R-G-B) visible lasers and LEDs.[6-9] Figure 1-1 shows the relationship between the bandgap of $Zn_xCd_yMg_{(1-x-y)}Se$ at 77K and the lattice-mismatch to InP substrates ($\Delta a/a_s \times 100$), where $\Delta a = a_l - a_s$, a_l and a_s are the lattice-constant of the epilayer and substrate, respectively. The

zero-mismatch position is indicated by a vertical dashed-line. The three solid squares represent the position of binary materials ZnSe, CdSe and MgSe. The solid line represents the empirical fit to the ZnCdSe data reported in the literature.[10] The lattice matched ZnCdSe material has a 77K bandgap of about 2.18 eV. The solid line and two dashed-lines representing ZnMgSe and CdMgSe are the boundaries of the $Zn_xCd_yMg_{(1-x-y)}Se$ quaternary material. We have assumed linear dependencies for the ZnMgSe and MgCdSe ternaries. From this figure, it is clear that by adding Mg into the ZnCdSe ternary and keeping lattice matched condition, the bandgap of the $Zn_xCd_yMg_{(1-x-y)}Se$ quaternary material can be varied from 2.18 eV to above 3.5 eV. By using different bandgap $Zn_xCd_yMg_{(1-x-y)}Se$ layers as cladding and waveguiding layers and lattice-matched ZnCdSe layer as the active layer, we can design a totally lattice-matched laser structure which can emit throughout most of the visible range, from blue to yellow. By adding some excess Cd into the ZnCdSe active layer, the emission range can be extended to the red with a small lattice-mismatch (at 610 nm, the mismatch is about 1.2%). With this mismatch the active layer can be grown coherently strained (pseudomorphic) to the entire structure. The use of InP substrates also allows the growth of a symmetrically strained ZnSe/ZnTe superlattice or lattice-matched ZnSeTe[11, 12] alloys for the ohmic contact, eliminating the formation of misfit dislocations in

the contact layer. Furthermore it is expected that incorporating large amounts of Mg in $Zn_xCd_yMg_{(1-x-y)}Se$ will make this material harder[13] than the ZnSe/GaAs based material, so this material may be less prone to degradation than the ZnSe based materials. All of these features are expected to improve the over-all material quality and the performance of the laser structure. The work I have done involves the growth, optimization and characterization of $Zn_xCd_yMg_{(1-x-y)}Se$/InP layers and related quantum well and laser structures.

Our group at the City College of New York was the first group to report work on $Zn_xCd_yMg_{(1-x-y)}Se$ material system grown on InP substrates. A few notable advances have been achieved since I undertook my research. High quality lattice-matched $Zn_xCd_{(1-x)}Se$,[14-17] $Zn_xCd_yMg_{(1-x-y)}Se$[18, 19] and their quantum well structures[20] have been grown. The defect density for both $Zn_xCd_{(1-x)}Se$ and $Zn_xCd_yMg_{(1-x-y)}Se$ has been reduced to the mid-10^4 cm^{-2}. Optically pumped lasing of this structure at room temperature from blue to red has been also observed.[21, 22] High carrier concentration (~10^{18} cm^{-3}) n-type doping of $Zn_xCd_yMg_{(1-x-y)}Se$ has also been achieved.[23] In the following chapters, I will discuss these results in detail.

In chapter 2, the basics of MBE growth and sample characterization are introduced first. Then, the principles used to design semiconductor lasers are shown.

Chapter 3 focuses on the MBE growth of high quality $Zn_xCd_yMg_{(1-x-y)}Se$ materials on InP substrates. The improvements of the interface of II-VI and III-V are the main issue. The techniques to measure and reduce the defect density in this material system will be discussed in detail. The growth conditions for lattice matched $Zn_xCd_yMg_{(1-x-y)}Se$ with required bandgaps and the method to calculate the composition of $Zn_xCd_yMg_{(1-x-y)}Se$ will be given also in this chapter.

In chapter 4, we will discuss the detailed characterization of $Zn_xCd_yMg_{(1-x-y)}Se$ materials. Section 4-1 describes the measurements of double crystal x-ray rocking curves in both (400) and {511} reflections to evaluate the quality and the strain state of $Zn_xCd_yMg_{(1-x-y)}Se$ epilayers. Section 4-2 focuses on the measurements of photoluminescence at various temperature for $Zn_xCd_yMg_{(1-x-y)}Se$ layers with bandgap from 2.2 eV (ternary) to 3.05 eV. The dependence of bandgap on temperature will be given. The last section discusses the capacitance voltage measurements. The band offset between ZnCdSe and InP will be evaluated.

Chapters 5 and 6 discuss device issues. Chapter 5 will report the results of ZnCdSe/ZnCdMgSe based quantum well and optical pumped laser structures. The degradation study of these structures is also included. Other

potential applications, such as resonant tunneling diodes and electrical memory cells, will be presented in Chapter 6.

Finally, the summary chapter and the list of publications high-light the key achievements of this dissertation.

CHAPTER 2

BACKGROUND

2-1. Basics of Molecular Beam Epitaxy (MBE)

2-1-1. MBE principle

The MBE process[24] achieves epitaxial growth in an ultra-high vacuum (UHV) environment through the chemical reaction of one or more thermal molecular beams with a crystalline surface of the substrate. This process is illustrated schematically in figure 2-1 which shows the essential components necessary for MBE growth of ZnCdSe. All these components are in a UHV environment. Molecular beams are provided by thermal Knudsen effusion cells. Each cell contains a crucible which in turn contains one of the constituent chemical elements or compounds of the desired epilayer. The temperature of each cell is chosen so that the vapor pressures of the materials are sufficiently high for generation of thermal energy molecular beams by free evaporation. The cells are arranged so that the central portion of the beam flux distribution from each cell intersects the substrate. Each cell has a shutter between the cell and the substrate. Operation of these shutters permits abrupt

cessation or initiation of any given beam flux to the substrate. By choosing the appropriate cell through the opening of its shutter and the appropriate substrate temperature, epitaxial films of the desired chemical components can be obtained. The extremely high precision in beam flux control allows the growth of very thin layers, even mono-layers. This distinguishing characteristics has enabled MBE to become one of the main growth technologies for heterostructures including quantum wells and superlattices. While the UHV environment allows the growth of very pure materials, it is also ideal for in-situ analytical instrumentation. In Fig. 2-1, the in-situ reflection high energy electron diffraction (RHEED) technique is shown, which is a powerful technique to monitor the growth process. We will discuss this issue later.

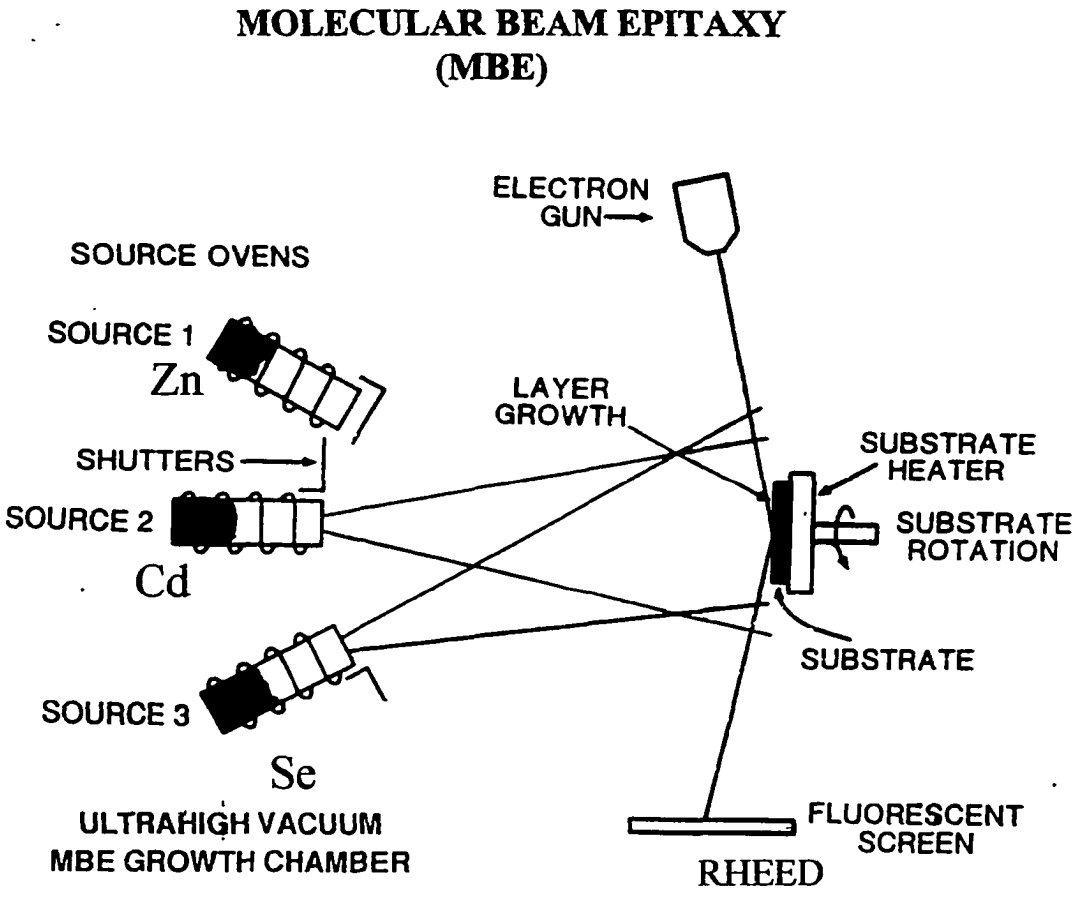

Figure 2-1. Illustration of MBE process

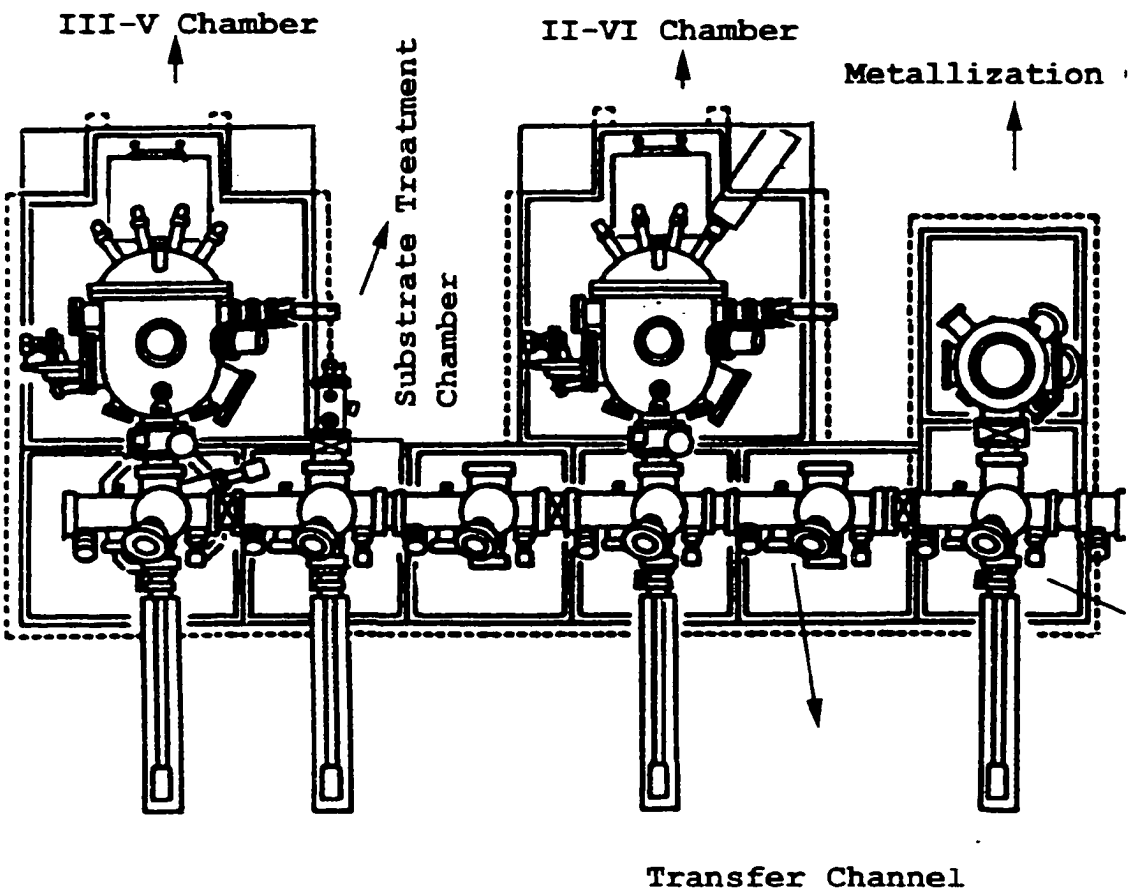

Figure 2-2. Top view of the MBE system

2-1-2. MBE system

The experiments in this dissertation were done in a Riber 2300P MBE system in Prof. Tamargo's laboratory. Figure 2-2 shows the schematic of the top-view of the system. The system includes 6 chambers: loading chamber, transfer channel, substrate treatment chamber, metallization chamber, and two growth chambers. Chamber 1 is for III-V materials and chamber 2 for II-VI materials. There are several gate valves to separate all the chambers to insure that unintentional cross contamination between them does not occur. In order to avoid contamination and achieve ultra-high vacuum, all the chambers are pumped by an ion-pump and a Ti sublimation pump except the loading chamber which is pumped by a turbo-molecular pump with a mechanical pump as the first stage and the substrate treatment chamber which is pumped by a cryo-pump. Besides the ion pump, the II-VI chamber and the metallization chamber are each pumped by an additional cryo-pump. The loading chamber is used for loading substrates. There is a gate valve between the loading chamber and the other chambers which allows us to vent the loading chamber by using ultra pure nitrogen gas to load substrates and not affect the vacuum in other chambers. This allow the vacuum in the other chambers to remain in the range of 10^{-10} Torr. The substrates or samples can

be transferred within the system through the transfer channel. The substrate treatment chamber is used to out-gas the substrates before transferring them to the growth chamber. The metallization chamber is equipped with an e-beam evaporator, which can deposit metal layers in situ on the sample to fabricate a device.

The chambers for the growth of III-V and II-VI semiconductor materials are similar. Each is equipped with a substrate manipulator (holder, rotator, heater and temperature sensor of the substrates), RHEED, quadrupole mass spectrometer, and cryo-shrouds around the manipulator and the cells. These cryo-shrouds will have a flow of liquid nitrogen (LN) through them during growth to prevent the thermal interference between the sources and also trap the residual molecules inside the chamber to obtain UHV vacuum. There are 8 cells in the III-V chamber equipped for Ga, In, Al, Mn, As, InP (for P flux), Si (for n-type doping) and Be (for p-type doping), and 8 cells in the II-VI chamber for Zn, Cd, Mg, Se, Te, CdTe, $ZnCl_2$ (for Cl flux used for n-type doping) and a radio frequency (RF) nitrogen cell for p-type doping. Very high purity materials from 6N to 8N have been used as the source materials to ensure high purity films are grown. Each time new sources were charged, the temperatures of all the sources were elevated to at least 100°C (except Se and $ZnCl_2$, whose temperature is 80°C and 60°C, respectively)

without introducing LN in the cryo-shrouds for ~ 6 hours to roughly outgas the source materials. Then the sources were elevated to a temperature ~ 20°C higher than the temperature required during the growth, with the LN cooling of the chamber, for ~6 hours to insure the source materials were thoroughly out-gassed before the actual growth took place. All the pyrolytic boron nitride (PBN) crucibles used in the chambers were out-gassed in the transferring channel or substrate treatment chamber by heating to ~ 1200°C for ~ 24 hours before they were used.

2-1-3. Growth procedure of MBE

InP (100) substrates from Sumitomo Electric, having defect density of ~ 10^3 cm^{-2}, were used in this dissertation. Prior to use, the substrates were degreased by using trichloroethylene (TCE), acetone and methanol and etched in H_2SO_4:H_2O_2:H_2O (4:1:1) for 1 minute to remove the residual polishing damage. Then an oxide layer was formed on the surface by flushing the wafers with deionized water to protect the fresh InP surface from contamination of carbon. The wafers were then In-bonded onto a Mo block to load into the loading chamber in the MBE system. The loading chamber was first pumped by an oil-free mechanical pump, then it was pumped by two

sorption pumps to ~ 10^{-3} Torr. After that, the turbo-pump system was opened and the loading chamber was pumped down very quickly to 10^{-8} Torr. The substrates were transferred to the substrate treatment chamber to out-gas at 150°C for 20 min. The oxide desorption of the substrate was performed in the III-V chamber by heating the substrate with an As flux inpingent on the InP surface. The details of oxide desorption will be discussed in chapter 3. After the growth of the III-V buffer layer, the substrate was transferred very quickly to the II-VI chamber to start the growth of II-VI layer. The contamination or damage during the transfer is expected not to be severe.[25]

2-1-4. In-situ monitoring of the deoxidization and the growth

Because of the ultra-high vacuum environment, MBE is compatible with in-situ electron diffraction techniques to monitor the surface during the oxide desorption and growth. The RHEED is the typical method for that.[26, 43] As shown in Fig. 2-1, RHEED uses very high energy electrons and glancing incidence. This geometry allows the diffraction pattern to be observed while the growth is going on as the molecular beams are directed normal to the surface. The glancing incidence also ensures that the high energy electrons only penetrate to a very thin layer on the surface. This is true because the

penetration depth of the incident electron beam depends on the energy component normal to the surface. This normal component is very small (~ 150 eV) in RHEED even though the electrons have an energy of ~10 keV and the diffraction gives information of a very thin layer near the surface. Therefore RHEED is very sensitive to the surface and is an ideal method to monitor the surface in-situ. The RHEED pattern depends on the atomic arrangement, flatness of the surface and the direction of the growth surface. Typical RHEED pattern for a disordered surface (for example before the deoxidization) is a diffuse pattern or rings due to the thin amorphous oxide layer on the surface;[27] for a clean surface after deoxidization it is streaky lines or ordered spots.[27] For three dimensional growth it is ordered spots such as a bulk crystal pattern; for two dimensional growth it is streaky with a surface reconstruction. The typical surface reconstructions for an As-rich (001) GaAs surface are (2×4) or c(4×4) or c(2×8) depending on how much excess As is on the surface;[26, 43] for a Ga-rich (001) GaAs surface they are (4×2) or c(8×2); for a Se-rich (001) ZnSe the typical pattern is (2×1) and for Zn-rich (001) ZnSe the pattern is C(2×2).[43] Thus, from the RHEED pattern we can know whether the deoxidization is finished, whether the growth is two dimensional and which element terminates the surface.

2-1-5. Characterization of the epilayers

When the growth was finished, the samples were taken out from the chamber and removed from the Mo block. The surface of the samples was evaluated by using Nomarski microscopy. The thickness of the epilayer was measured by using Philtec's radial sectioning instrument. The optical properties, from which we can usually obtain the bandgap, were measured by

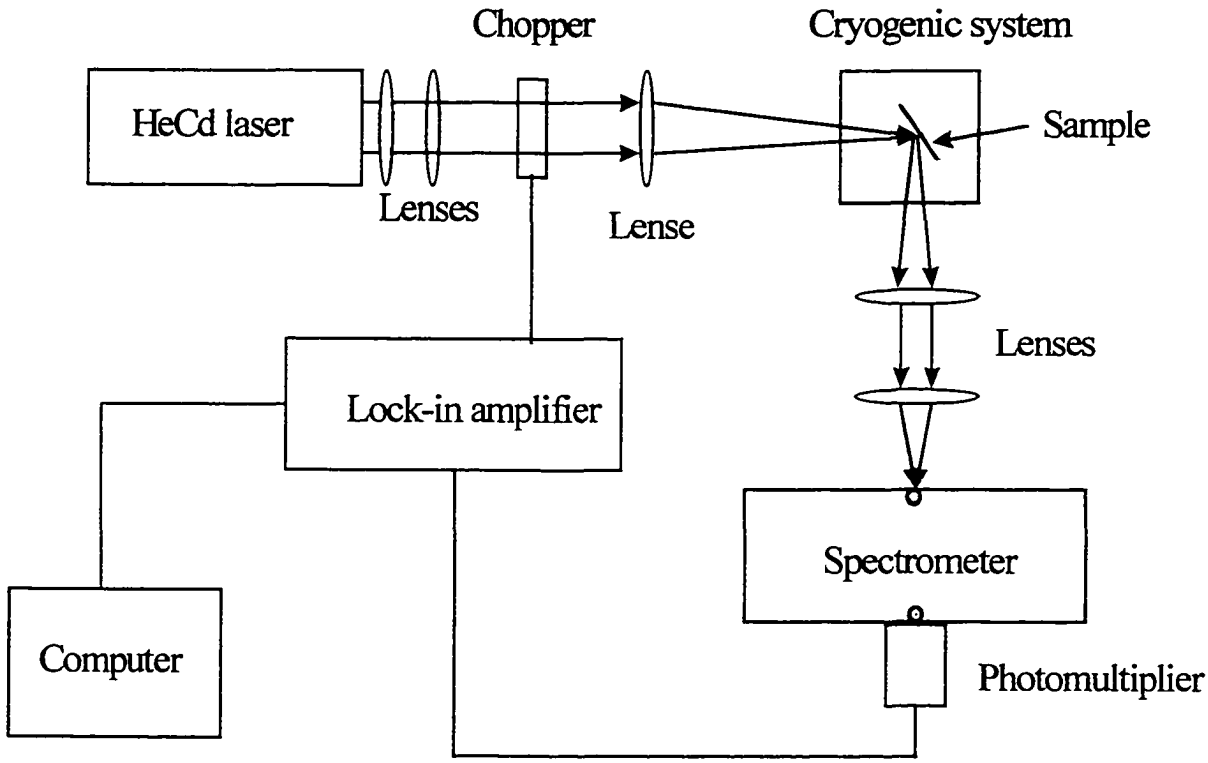

Figure 2-3. Illustration of photoluminescence setup

using photoluminescence (PL) at temperatures from 5.8 K to 300K. The crystalline quality and the lattice-mismatch were measured by single crystal x-ray diffraction, double crystal x-ray diffraction and transmission electron microscopy (TEM). The electrical properties were measured by Hall effect, capacitance voltage (C-V) and current voltage (I-V) measurements. In the following I will introduce the PL, x-ray measurements and the method for thickness measurements. The TEM, C-V and I-V will be described in detail when their results are shown in Chapters 3, 4 and 6.

1. **Photoluminescence (PL)**

The schematic of the PL system is shown in figure 2-3. The samples are mounted on the cold finger of a Janis cryogenic system. The system is pumped to ~ 10^{-5} Torr before cooling it. The cold finger can be cooled down to 5.8 K using liquid helium and 78 K using liquid nitrogen. The temperature of the cold finger can be controlled between 5.8 K to 300 K by using a heater installed on the back of the cold finger. A He-Cd laser with the emission wavelength of 325 nm is used as the excitation source. The laser beam passes through a chopper which changes the laser beam to a periodic signal (ac), then is focused to a small spot on a sample. The luminescence from the sample is collected by a lense and converted to a collimated beam. The

collimated beam is focused to a spot on the first slit of the spectrometer. The beams that pass through the SPEX 1680-B spectrometer are detected by a photomultiplier and are converted to an electrical signal. The ac signal is then fed to a lock-in amplifier to be amplified. Finally the amplified signal is inputted into the datascan connected to the computer to be collected and analyzed. The PL spectrum can give us the information about the band gap, quality and band structure of the epilayers.[28]

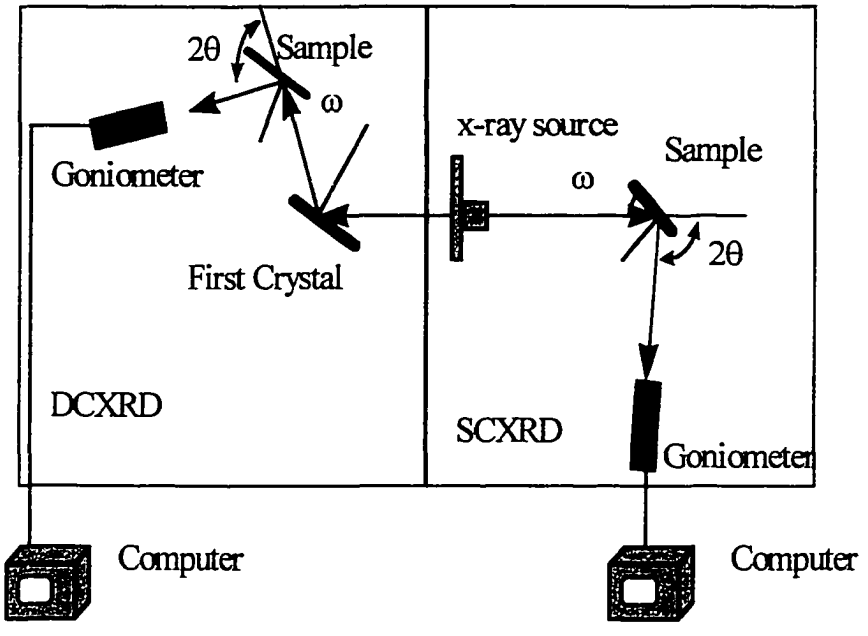

Figure 2-4. X-ray diffraction system

2. **X-ray diffraction**

X-ray diffraction is an important technique[29] used to characterize semiconductor materials. It can give information about the lattice constant,

the crystal structure, the quality and the strain in the layer. The schematic of our x-ray diffraction system is shown in fig. 2-4. It consists of an x-ray source, a single crystal x-ray diffraction system shown on the right (SCXRD) manufactured by RIGAKU and a double crystal x-ray diffraction system shown on the left (DCXRD) manufactured by Blake Industries, Inc. In both cases, the rotation of the sample holder will change the incident angle ω while rotation of the goniometer will change 2θ. In the following, I will describe them separately.

In SCXRD, only one crystal (the sample) is used, so the incident x-ray here is not monochromatic and it is difficult to eliminate the Cu $K_{\alpha 2}$ line. Therefore, the incident x-ray beam contains both Cu $K_{\alpha 1}$ and Cu $K_{\alpha 2}$ lines. In the diffraction, each layer has two peaks corresponding to Cu $K_{\alpha 1}$ and Cu $K_{\alpha 2}$. Usually the intensity of the peak corresponding to Cu $K_{\alpha 1}$ is double that of the peak corresponding to Cu $K_{\alpha 2}$. Because the beam has a broad band of wavelengths, the diffraction peaks are usually broad. In SCXRD, we usually use $\theta - 2\theta$ couple mode, which means that the ω and 2θ are moving simultaneously and ω is always half of 2θ. In the practical measurement, the back of the sample has indium and it is very hard to mount the sample exactly parallel to the sample holder. In order to make sure the ω and 2θ are coupled,

we first fix the 2θ and rotate the ω around θ (usually called a rocking curve), find the ω value corresponding to the peak and adjust the ω value to make sure the ω value corresponding to the peak is θ, which means the ω and 2θ are coupled. We then set the scan mode as the θ – 2θ couple mode to measure the diffraction. The SCXRD is good to measure large lattice-mismatch and to find the structure of the materials.

In DCXRD, a first crystal [(100) Ge in our system] is used to separate the various wavelengths of the incident x-ray beam in order to narrow the x-ray band of wavelengths before the x-ray beam reaches the sample. So the incident beam on the sample is highly monochromatic and also has only the Cu $K_{\alpha 1}$ line. The measurement sample is the second crystal. In DCXRD, the rocking curve is usually measured, that is, the 2θ is fixed and the ω is varied around θ. This method is good to measure small lattice-mismatch and to evaluate the layer quality. The full width of half maximum (FWHM) of the diffraction peaks give us information about the material quality. We will discuss more in chapter 4 about this measurement.

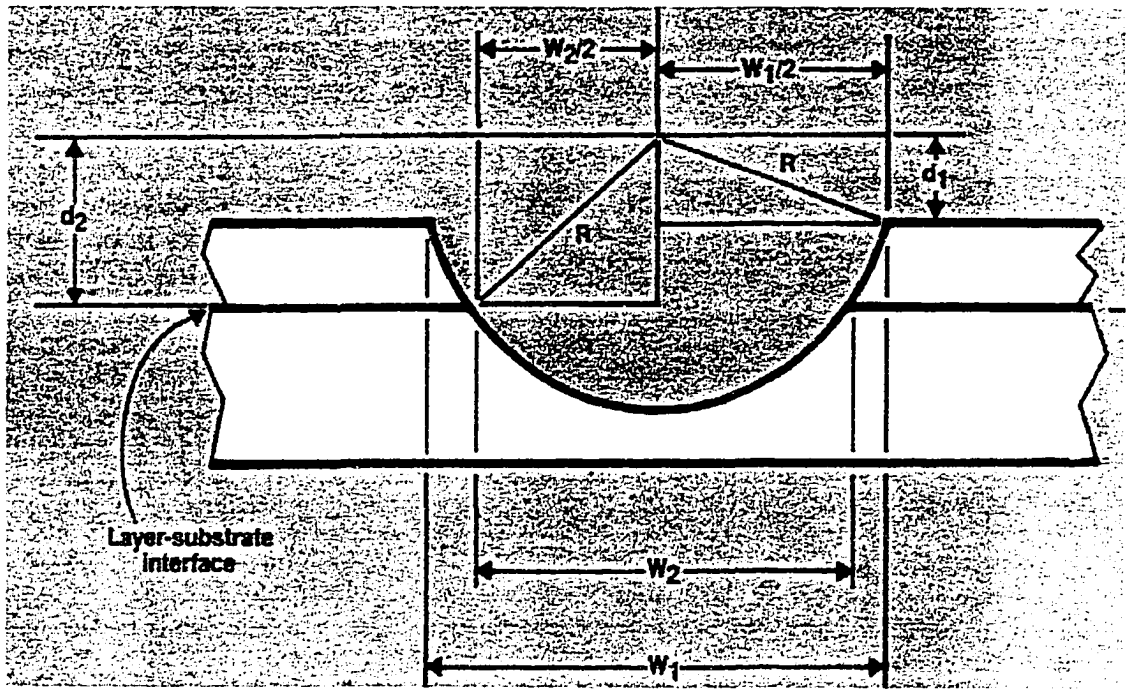

Figure 2-5. The principle of thickness measurements by using Philtec's radial sectioning machine.

3. **Thickness measurements**

In this section, I will introduce the principle of thickness measurements by using Philtec's radial sectioning machine. The basic idea is to use a spindle with known radius to make a groove on the surface in order to amplify the thickness of the epilayer. Figure 2-5 shows the cross section of the groove, where R is the radius of the spindle, W_1 is the width of the cylindrical section, W_2 is the width of the section at the level of the layer interface and X_t is the thickness of the epilayer. W_1 and W_2 can be measured

using microscopy. Mathematically, the layer thickness is the difference in the heights of two triangles having the groove radius (R) as the common hypotenuse. So the epilayer thickness, X_t, is given by:

$$X_t = [R^2 - (W_2/2)^2]^{1/2} - [R^2 - (W_1/2)^2]^{1/2} \qquad (2\text{-}1)$$

In the following, we will evaluate the errors of this method. The radius of the spindle is 19 mm, which is much larger than the values of W_1 and W_2 (on the order of a few hundred μm), so X_t can be expressed as:

$$\begin{aligned} X_t &= R\{ [1 - (W_2/2R)^2]^{1/2} - [1 - (W_1/2R)^2]^{1/2}\} \\ &\approx R\{1-1/2(W_2/2R)^2 - [1-1/2(W_1/2R)^2]\} \\ &= [1/(8R)](W_1^2 - W_2^2) \qquad (2\text{-}2) \end{aligned}$$

Then the derivative (or small change) of X_t will be:

$$dX_t = [1/(4R)](W_1 dW_1 - W_2 dW_2)$$

where dW_1 and dW_2 are the derivatives or the small changes of W_1 and W_2. When $dW_1 = -dW_2 = dW$, dX_t will be maximum:

$$dX_t|_{max} = [1/(4R)](W_1+W_2)dW \qquad (2\text{-}3)$$

Divided both sides by X_t [equation (2-2)], we get:

$$dX_t|_{max}/X_t = [2/(W_1-W_2)]dW \qquad (2\text{-}4)$$

From this expression, we can conclude that in order to reduce $dX_t|_{max}/X_t$, (W_1-W_2) should be large and dW should be small. Therefore, the

time for grooving should be optimal to get maximum (W_1-W_2). Generally, for a sample with an epilayer of thickness of ~1 μm, the (W_1-W_2) is ~ 100 μm and the error to measure W_1 and W_2 on the picture of amplification of 100 is ~ 0.05 cm, which means dW is ~ 5 μm, therefore $dX_t|_{max}/X_t$ is about 0.1, meaning that the error is ~ 10%.

2-2. Principles of semiconductor laser design

In this section, a brief introduction about the principles involved in semiconductor lasers will be given in order to understand what are the requirements of the semiconductor materials and how we choose the structure to grow in order to fabricate optically pumped lasers as will be described in chapter 5.

As we know, lasing only occurs under two essential conditions:[30, 31] the presence of a gain medium that can amplify the light passing through it and a feedback mechanism which forms a resonator. In a semiconductor laser, the gain medium is the semiconductor itself and the feedback mechanism is usually a Fabry-Perot cavity formed by the two natural cleavage planes of the semiconductor.

The light amplification is accomplished by a process called stimulated emission. There are three processes of interaction between the electromagnetic wave and matter: spontaneous emission, stimulated emission and absorption. The Einstein relations show that the absorption and stimulated emission probabilities are equal and are both related to the spontaneous emission probability. These expressions lead to the necessary condition for stimulated emission, which is that the separation in quasi-Fermi levels should exceed the photon emission energy, i.e. $F_n - F_p > h\nu$. The separation of quasi-Fermi levels can be achieved by the injection of electrons and holes using either electrical or optical pumping to disturb the thermal equilibrium. When the electrons and holes are injected into the active region, they will distribute in the conduction band minimum and valence band maximum associated with their density of state function, respectively. The distribution of both carriers can be described using their quasi-Fermi levels assuming that they are in quasi-thermal equilibrium. When the injected electrons and holes reach certain concentration, the separation of the quasi-Fermi levels will be larger than the bandgap. Then the stimulated emission will occur and dominate.

In order to efficiently collect the injected carriers, heterostructures in which the active region is sandwiched by two larger bandgap materials are

used in all the semiconductor lasers. The conduction band offset between the active layer and the two larger bandgap layers should be able to prevent the electrons from flowing out of the active region while the valence band offset between the active layer and the two larger bandgap layers should be able to prevent the holes from flowing out of the active region. So a type I interface is required. A band offset of at least 100 meV is required to provide effective carrier confinement.[31]

The heterostructure also provides the optical confinement of the laser. In order to enhance the coupling between light and active region, a waveguide structure which confines the light within the active region is preferred. Because larger bandgap material has a smaller index of refraction, the double heterostructure (DH) constitutes a suitable waveguide, which overlaps the most intense part of the light with the gain region. A figure of merit measuring the confinement of the light within the active region is called confinement factor, Γ, defined by the ratio of the power in the active region to the total power of the light. The typical confinement factor of DH lasers with a active layer thickness of 1000 Å is ~ 30%.

When the thickness of the active layer is reduced to the dimension comparable with the de Broglie wavelength of the carriers, the quantum size effect emerges. The motion of carriers perpendicular to the junction must

satisfy the standing-wave pattern, which means the energy of the carriers along the vertical direction is quantized. The quantization of energy changes the three dimensional bulk property into two dimensional. The quantum size effect makes at least two contributions to semiconductor lasers. First, the step function of density of states provides a larger gain coefficient than that of the double heterostructure. So less carriers are needed to provide the same optical gain than its bulk counterpart. Second, due to the higher energy level of the heavy hole with respect to the valence band edge compared with the light hole, most of the holes will populate in the heavy hole bands. Thus, most of the radiative recombination comes from the transition between the electron and the heavy hole bands, which results in the radiation of pure transverse electric (TE) wave in the waveguide configuration.

Although QW lasers seem to have better gain property, the thin QW reduces the confinement factor.[31] So the structure needs some modification. In designing the QW laser, a pair of waveguide layers with intermediate bandgap are always inserted between the active layer (QW) and the two cladding layers. If it is a uniform layer, we call it separate confinement double heterostructure single QW laser (SCDH). Sometimes a layer with graded variation in bandgap is used, then it is called graded index separate confinement heterostructure single QW laser (GRINSCH). The introduction

of the waveguide layers improves both the wave and carrier confinements. Since the wave confinement factor is proportional to the square of the thickness of active layer, with 10 nm width, the confinement factor of a QW is about 0.1%, which is far less than that of the DH lasers. Using the waveguide layers to focus the intensity distribution to the center, a confinement factor of 3% can be achieved with optimal design. Another function of the two waveguide layers is to help the carriers to be scattered into the well. Because the width of QW is smaller than the mean free path of the carriers, an intermediate stage is necessary to collect the carriers efficiently. From the point of view of carrier confinement, a wider waveguide layer is preferred. However, once the waveguide can accommodate a second mode, the wave confinement starts to decrease. Usually 1000 to 2000 Å waveguide layer will not accommodate a second mode in the waveguide. Finally the thickness of the cladding layer must be thick enough to prevent the wave from spreading out of the cladding layer.

As described in chapter 1, the $Zn_xCd_yMg_{(1-x-y)}Se$ system is a suitable system to design lasers emitting within all the visible range. In chapter 5, a structure of SCDH quantum well laser for optical pumping will be given. In that structure, two ZnCdMgSe layers with bandgap of 3.0 eV were used as

the cladding layers, two 1000 -2000 Å thick ZnCdMgSe layers with intermediate bandgap of 2.7 eV were used as the waveguide layers, a ZnCdSe QW layer was used as the active layer. We have obtained optical pumped laser emission from this structure with emission ranging from red to blue.

CHAPTER 3

MBE Growth of High Quality $Zn_xCd_yMg_{(1-x-y)}Se$ Layers on InP Substrates

3-1. Introduction

In order to grow lasers and LEDs for full color displays, it is necessary to grow high quality lattice matched $Zn_xCd_yMg_{(1-x-y)}Se$ layers with different bandgaps. In this chapter, I will first report the lattice-matched growth conditions for $Zn_xCd_yMg_{(1-x-y)}Se$ layers with the required bandgap to avoid misfit dislocations. Then I will focus on the quality improvements of these layers, which include techniques to measure the defect density and techniques to improve the II-VI/III-V interface.

3-2. Growth Conditions of $Zn_xCd_yMg_{(1-x-y)}Se$ Layers Lattice-matched to InP Substrates

$Zn_xCd_yMg_{(1-x-y)}Se$ is a quaternary material. In order to grow lattice matched $Zn_xCd_yMg_{(1-x-y)}Se$ layers with required bandgaps, we need to know

the dependencies of the bandgap and lattice constant of $Zn_xCd_yMg_{(1-x-y)}Se$ layers on the composition x and y in the solid and we need to know how to control the bandgap and lattice constant of $Zn_xCd_yMg_{(1-x-y)}Se$ layers by controlling the growth parameters such as fluxes of Zn, Cd, Mg and Se.

The composition of $Zn_xCd_yMg_{(1-x-y)}Se$ quaternaries is an important parameter of the materials. From the composition, we can adjust the growth conditions to get the desired bandgap and lattice-mismatch. Similar to calculations reported previously for ZnCdSeTe,[10] we assume the dependence of bandgap at 10 K on x and y as:

$$Eg(x, y) = ax^2 + by^2 + cxy + dx + ey + f$$

When x = 0, the material is $Cd_yMg_{(1-y)}Se$. Its bandgap is: $Eg = by^2 + ey + f$. Assuming linear dependence of the bandgap for the $Cd_yMg_{(1-y)}Se$ ternary on y and using the bandgaps of MgSe[32] and CdSe at 10 K (3.65 eV and 1.78 eV, respectively), we obtain: b=0, e= -1.87 and f=3.65. Similarly, when y=0, we obtain a=0 and d=-0.83 by assuming linear dependence of bandgap for the $Mg_{(1-x)}Zn_xSe$ ternary on x and using the bandgap of ZnSe at 10 K (2.82 eV). So at this point, the equation becomes:

$$Eg(x, y) = cxy - 0.83x - 1.87y + 3.65$$

When x + y =1, the material is the Zn_xCd_ySe ternary. By using the known relationship[10] of $Zn_{(1-y)}Cd_ySe$: $Eg(y) = 0.35\ y^2 - 1.39\ y + 2.82$, we

obtain c = -0.35. Finally, combining the three relationships, the expression to describe the dependence of bandgap for $Zn_xCd_yMg_{(1-x-y)}Se$ on the composition x and y is:

$$Eg\ (x, y) = -0.35\ xy - 0.83\ x - 1.87\ y + 3.65 \qquad \text{at 10K} \qquad (3\text{-}1)$$

Using Vegard's law: the lattice-constant in the alloy will depend linearly on the composition, we assume the relationship between the lattice-constant and the composition for $Zn_xCd_yMg_{(1-x-y)}Se$ is:

$$a\ (x, y) = ax + by + c(1-x-y)$$

The a (0, 1), a (0, 0) and a (1, 0) should be equal to the lattice constant of CdSe, MgSe and ZnSe, respectively. By using the lattice-constant of ZnSe (5.667 Å), CdSe (6.076 Å) and MgSe (5.89 Å),[32] the constants a, b and c can be calculated:

$$a = 5.667,\ b = 6.076 \text{ and } c = 5.89.$$

So a(x, y) for $Zn_xCd_yMg_{(1-x-y)}Se$ can be expressed as:

$$a\ (x, y) = 5.667x + 6.076y + 5.89\ (1-x-y)$$

$$= -0.223\ x + 0.186\ y + 5.89 \qquad (3\text{-}2)$$

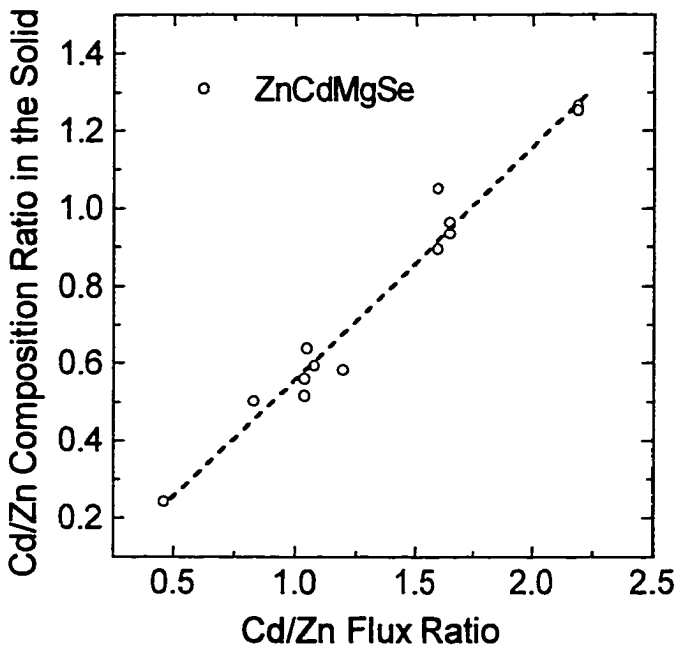

Figure 3-1. Relationship between the Cd to Zn composition ratio in the solid, calculated as described in the text, to the experimental Cd to Zn flux ratios.

By using equations (3-1) and (3-2), we can calculate the composition x and y from the bandgap data measured by PL and lattice-constant evaluated from x-ray (400) diffraction, assuming the epilayer is fully relaxed. The relationship between the calculated Cd/Zn composition ratio in the solid and the Cd/Zn flux ratio used during growth is shown on figure 3-1 for samples grown with different Mg cell temperatures.[18] We note that the calculated Cd/Zn composition ratio is proportional to the measured Cd/Zn flux ratio used during growth which suggests that incorporation of Mg does not affect the sticking efficiency of Zn and Cd. Taking advantage of this observation we have grown $Zn_xCd_{(1-x)}Se$ ternary and $Zn_xCd_yMg_{(1-x-y)}Se$ quaternary layers under the same growth conditions (including the growth time, Zn and Cd fluxes etc.), and used the thickness difference between the $Zn_xCd_{(1-x)}Se$ and $Zn_xCd_yMg_{(1-x-y)}Se$ layers (i.e., the difference in growth rate) to estimate the

Mg composition. If we take the growth rate measured for $Zn_xCd_{(1-x)}Se$ and $Zn_xCd_yMg_{(1-x-y)}Se$ as R_t and R_q, respectively, then the composition of Mg can be estimated by using the following expression:

$$\text{Mg composition } (1\text{-}x\text{-}y) = (R_q - R_t)/R_q \qquad (3\text{-}3)$$

Table I compares the calculated Mg composition based on our mathematical expressions (3-1) and (3-2) with the Mg composition estimated from the thickness measurements by using expression (3-3). Good agreement (better than 10%) between the two values was observed. We conclude that these equations can now be used to predict the composition of a layer of a given bandgap and lattice constant.

Table I: Comparison of the calculated Mg composition in the layer and measured Mg composition, as described in the text.

Sample	Mg composition	
	Calculated	Measured
1	0.57	0.62
2	0.47	0.53
3	0.43	0.45
4	0.39	0.43
5	0.5	0.52

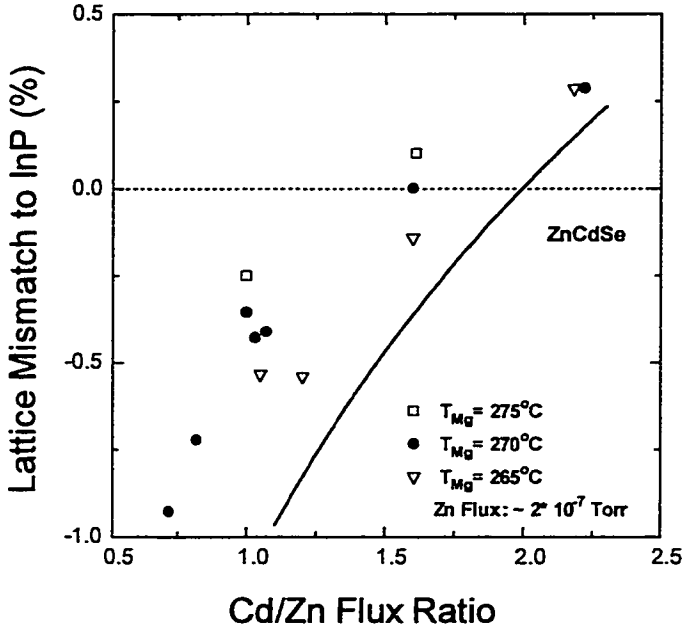

Fig. 3-2.Dependence of Cd to Zn flux ratio on the lattice-mismatch of ZnCdMgSe grown on InP with various Mg fluxes.

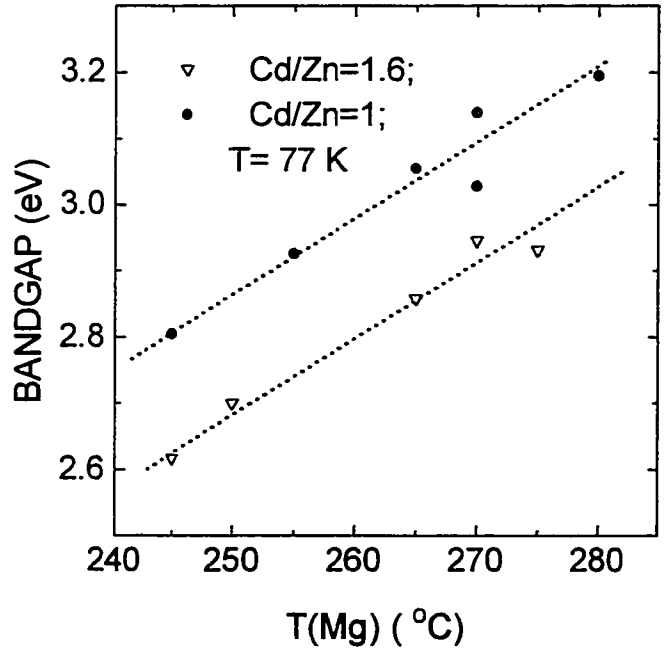

Figure 3-3. Dependence of quaternary bandgap on Mg cell temperature (flux) for two Cd to Zn flux ratios.

Figure 3-2 shows the percent lattice mismatch of the $Zn_xCd_yMg_{(1-x-y)}Se$ quaternary layer to InP (%Δa/a) as a function of Cd/Zn flux ratio used during growth for various Mg fluxes. The zero mismatch position is indicated in the figure by a dashed-line. The solid line represents the empirical fit to the ZnCdSe ternary. For Cd/Zn =2 which is the condition for ZnCdSe lattice-matched to InP, changing the Mg flux does not affect the mismatch very much, but it is always greater than 0, and experimentally, the layers tend to have spotty RHEED patterns. Therefore to obtain lattice-

matched quaternaries we must reduce the Cd/Zn ratio: in order to incorporate more Mg and get higher bandgaps, one must lower the Cd/Zn ratio further.

Figure 3-3 shows the dependence of the quaternary bandgap on Mg flux for two different Cd/Zn flux ratios both of which are less than 2. The bandgap energy was estimated from the photoluminescence spectra at 77 K. A comparison between the PL emission wavelength and photoreflectance signals for several samples confirmed that the PL spectra are in fact dominated by bandedge emission. For the bandgap estimates we did not account for any exciton binding energy at 77K. We feel that this will not have a significant influence on our results. For Cd/Zn=1, changing the Mg temperature from 245°C to 275°C causes the mismatch to change from -0.7 % to -0.2 % and the bandgap to change from 2.6 eV to 2.9 eV. For this Cd/Zn ratio, in order to get less mismatch and higher bandgap, one must increase the Mg flux further. However, when we increase the Mg temperature above 280°C, the layer quality degrades. When the Cd/Zn flux ratio is about 1.6, if we change the Mg temperature from 245°C to 280°C, the mismatch changes from -0.2 % to 0.1%, and the bandgap changes from 2.8 eV to 3.2 eV. At this flux ratio, for small changes in mismatch we can obtain a wide range of bandgaps, making it useful for the laser design.

3-3. Quality Improvements of $Zn_xCd_yMg_{(1-x-y)}Se$ Layers

3-3-1. Determination of defect density in $Zn_xCd_yMg_{(1-x-y)}Se$ layers using a chemical etch

In order to improve the quality of $Zn_xCd_yMg_{(1-x-y)}Se$ layers, we need to find a method to measure the defect density of $Zn_xCd_yMg_{(1-x-y)}Se$ layers. There are a number of methods for characterizing the defect density and the distribution of defects in a crystal. TEM is an accurate way to measure defect density. But it is complicated and expensive. Furthermore, in the low defect density ranges ($<10^6$ cm^{-2}), it is no longer accurate. Chemical etching can reveal defects by formation of etch pits. Both defect density as well as distribution can be determined even in low defect density range ($<10^6$ cm^{-2}) where TEM is no longer accurate. The key to this technique is to find an etching solution that can selectively etch the defects. Bromine-methanol solution has been used to reveal the defects in ZnSe,[33-35] ZnSSe[34] and ZnMgSSe,[36] but we found that it did not work for the etch pit density measurements of $Zn_xCd_yMg_{(1-x-y)}Se$ layers.

In this work we have developed a chemical etching technique[37] suitable for revealing defects in $Zn_xCd_yMg_{(1-x-y)}Se$ epitaxial layers. We found that a

hydrobromic acid and acetic acid solution, which was used to measure the defect density of InP layers,[38] worked well for the etch pity density (EPD) measurements of $Zn_xCd_yMg_{(1-x-y)}Se$ layers. The accuracy of the etchant for revealing stacking faults and dislocations was verified by plan-view transmission electron microscopy (TEM). Surface scanning and profiling by atomic force microscopy (AFM) were used for the first time to characterize the morphology of the etched samples as a function of etch time. The results showed that the pit depth became constant after a depth corresponding to approximately the II-VI layer thickness. The TEM and AFM results also showed that the etch solution is very selective.

A hydrobromic acid and acetic acid solution at a concentration of 1 : 7 by volume was used at room temperature for the etch pit evaluation of the $Zn_xCd_yMg_{(1-x-y)}Se$ epilayers. The suitability of the etching conditions and the stability of the results were established by measuring the etch rate and investigating the effects of the etching time. The surface morphology before and after etching was observed with Nomarski microscopy and AFM, both performed at room temperature. The AFM images were obtained in the contact mode with a tracking force < 5 nanonewtons using a TopoMetrix TMX2000 AFM system. The layers with and without etching were also characterized by plan-view TEM to compare with the EPD results. The

samples were prepared for TEM by mechanical polishing and chemically thinned to perforation with bromine-methanol.[14-15] All micrographs were obtained with a Philips EM430 operating at 300kV, with two-beam conditions. The layer thickness was measured using a Philtec sectioner. The etch rate of the flat surface (~2 Å/sec.) was determined using alpha-step by etching with one part of the sample masked with wax.

The etching behavior was examined in detail by changing the etching time using a $Zn_xCd_yMg_{(1-x-y)}Se$ layer with thickness of 0.15 μm. In order to make sure we were always monitoring the same part of the sample, we marked the sample area with a scratch. Figure 3.4 (a)-(d) shows the Normarski micrographs of the surface after etching for times of 20, 40, 60 and 80 seconds, respectively. No defects were seen on the as grown surface. When etched for 20 seconds, as shown Fig. 3-4(a), the etch pits were already resolvable, with a density of 1.8×10^6 cm^{-2}. After 40 seconds of etching [Fig. 3-4(b)] the etch pits developed into small squares with the edge along the <110> directions, which is the typical feature of etch pits on the (001) surface.[39] Furthermore, more etch pits were resolvable, the density now became 3.3×10^6 cm^{-2}. Etching for 60 seconds [Fig. 3-4(c)] made the squares very clear, some of them appeared to elongate or line up along one of the <110> directions. However, the density of the squares did not change

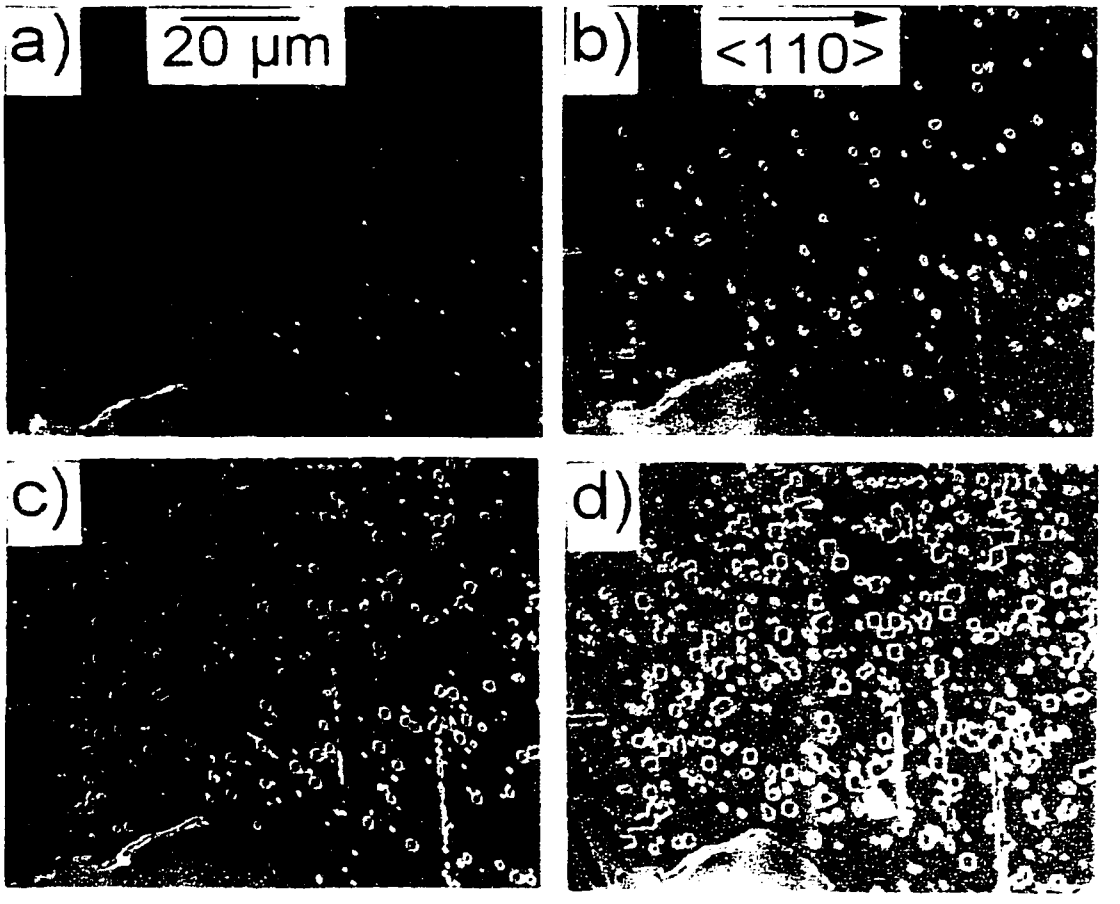

Figure 3-4. Nomarski micrographs of the surface of a 0.15-μm-thick ZnCdMgSe layer that was etched for (a) 20 s, (b) 40 s, (c) 60 s, and (d) 80 s.

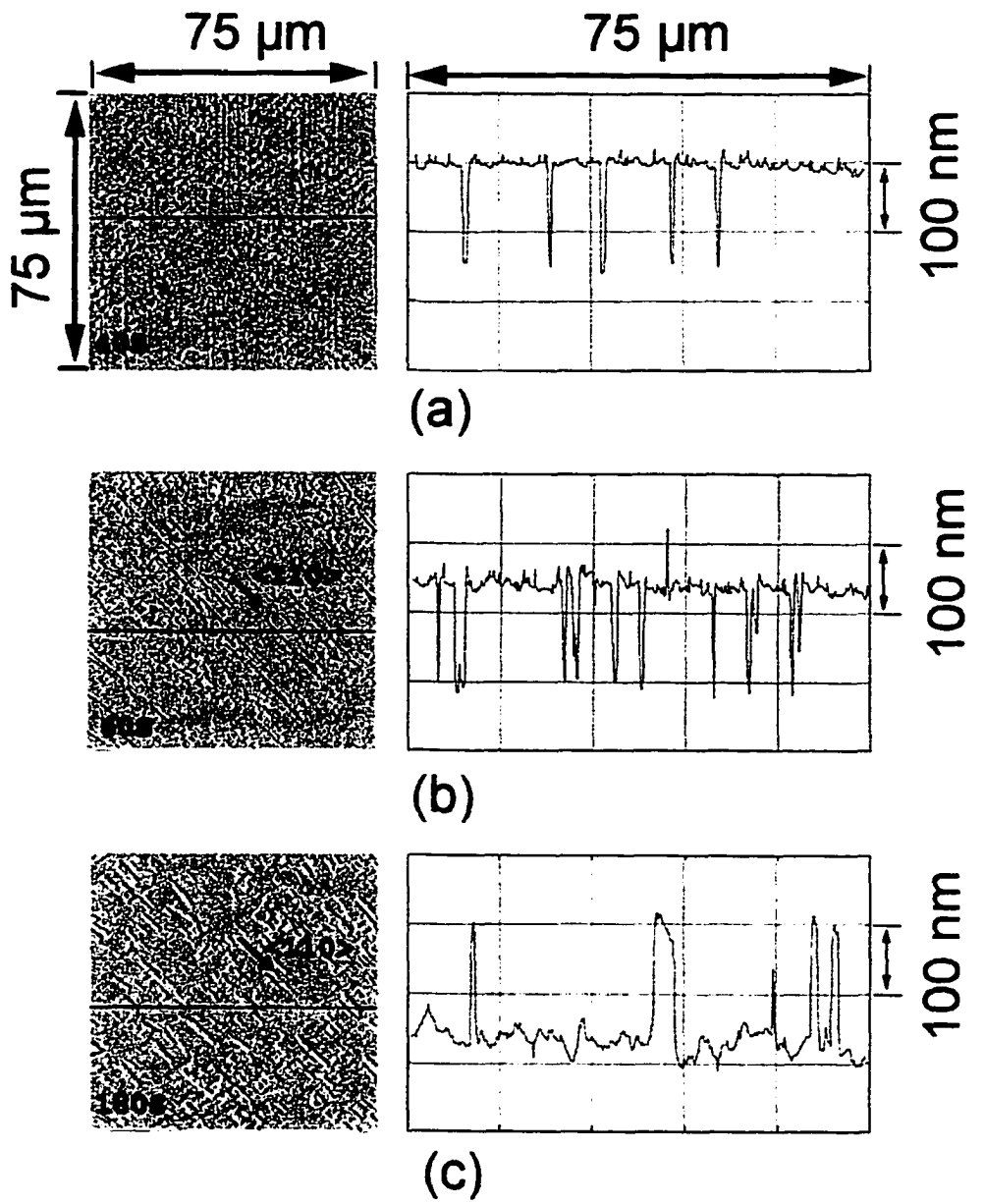

Figure 3-5. Atomic force micrographs (shown on the left) and line profiles (shown on the right) for a 0.15-µm-thick ZnCdMgSe layer that was etched for (a) 40 s, (b) 60 s, and (c) 180 s.

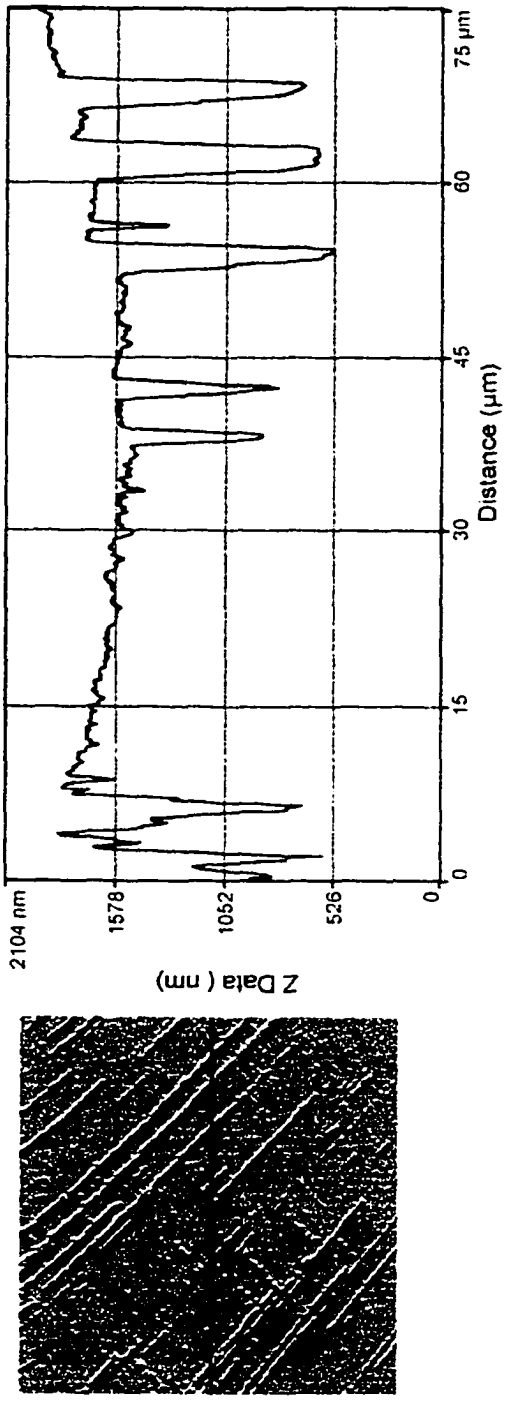

Figure 3-6. AFM scan and line profile for etched surface of 1.0-µm-thick ZnCdMgSe layer. The etch time is 1 min.

compared with Fig. 3-4(b). Thus the density of the squares reached a maximum after 40 to 60 seconds etching. Increased etching times, i.e., 80 seconds, shown in Fig. 3-4(d), produced the result that the square pits continued to increase in size and started to merge. At this point, it is very hard to count the number of the squares. These results indicate that a suitable etching time should be about 40 to 60 seconds. We also think that it is reasonable to count each square as only one defect since each square was developed from one small point.

Figure 3-5(a)-(c) shows the AFM images and line profiles for pieces of the same layer as above, etched with fresh solutions of the etchant for 40 , 60 and 180 seconds, respectively. The left hand side of these figures displays the surface morphology while on the right hand side is shown the profile along the line indicated on the left. Since in AFM it is difficult to focus on the same position of the sample after it has been removed from the instrument, these three etched samples were actually from slightly different but representative regions of the sample. Although the etching rate appeared somewhat faster, the surface morphology displayed similar changes as those observed from the Nomarski micrographs. The pits developed from small points to squares with edges along the <110> directions which eventually lined up. An interesting result is that even after only 40 seconds, the pits were very deep, about 150

nm, as can be seen from the profiling on the right hand portion of Fig. 3-5(a). The etching rate of the defect was very fast compared with the etch rate of 2 Å/sec. for the layer surface measured by alpha-step. This demonstrates that the solution is very selective. Fig. 3-5(a) gives a defect density of 6×10^6 cm^{-2} similar to that obtained from Nomarski micrograph. As illustrated in Figs. 3-5(b) and (c), the etching depth (150 nm) did not change significantly with continuous etching. Even though the EPD in Fig. 3-5(a) and (b) is the same, the number of etch pits sampled by the line profile shown on Fig. 3-5(b) is higher. This is because the etch pits have become larger, thus the line crosses more etch pits. After 180 seconds of etching, as shown in Fig. 3-5(c), the epilayer was almost removed. The AFM profile shows that there are only small regions where the layer is left. These regions are still about 150 nm thick. TEM indicates that the dominant defects in this sample are perfect misfit dislocation segments. Therefore it appears that the threading ends of these segments are the defects we observed by EPD.

Figure 3-6 shows the AFM image and line profile for a sample with 1μm $Zn_xCd_yMg_{(1-x-y)}Se$ layer after 1 min etch. It is clear that the etch depth of the pits is already ~ 1 μm, reaching the interface of the II-VI and III-V. Again, we conclude that the etch solution is very selective.

To check whether stacking faults were revealed by the EPD technique, we performed etching on another sample with a very thin $Zn_xCd_yMg_{(1-x-y)}Se$ layer (about 600 Å thick), which is expected to be pseudomorphic. We performed plan-view TEM measurements after various stages of defect etching on this sample. Fig. 3-7(a) shows the TEM image of the unetched piece. The defects indicated by SF are Shockley partial dislocations that thread through the layer on {111} planes. These dislocations bound grown-in stacking faults, which nucleated in one single point on the II-VI/III-V interface. (Under orthogonal reflection conditions, the stacking fault fringes were observed as in Ref. 14.) The density of stacking fault sets is $4\text{-}8\times10^6$ cm^{-2}. Although not visible in this image the sample also shows some perfect misfit dislocations of the 60° type with a spacing ~ 10 μm. Fig. 3-7(b) is the TEM image of another piece etched for 25 seconds. In this case some of the stacking faults have been etched into pits, but for others the etch pits could not yet be resolved. In Fig. 3-7(c) after 35 seconds etching, all of the stacking faults have been etched and the etch pits for all the stacking faults are resolvable. This is consistent with the observation by Nomarski microscopy that the EPD increased initially somewhat with etching time and then became constant. It is not clear why some of the stacking faults were etched faster than others.

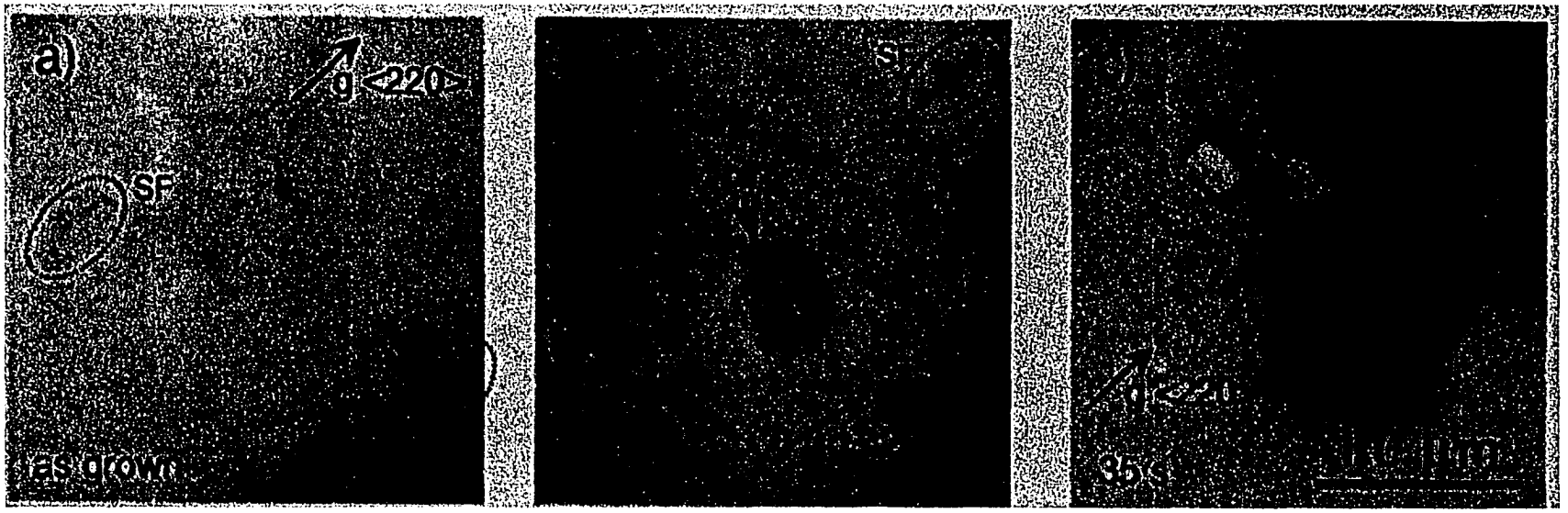

Figure 3-7. Plan-view TEM images for three pieces of a very thin ZnCdMgSe layer. (a) Shows the image for the as-grown surface while (b) and (c) show the images of pieces etched for 25 and 35 s, respectively.

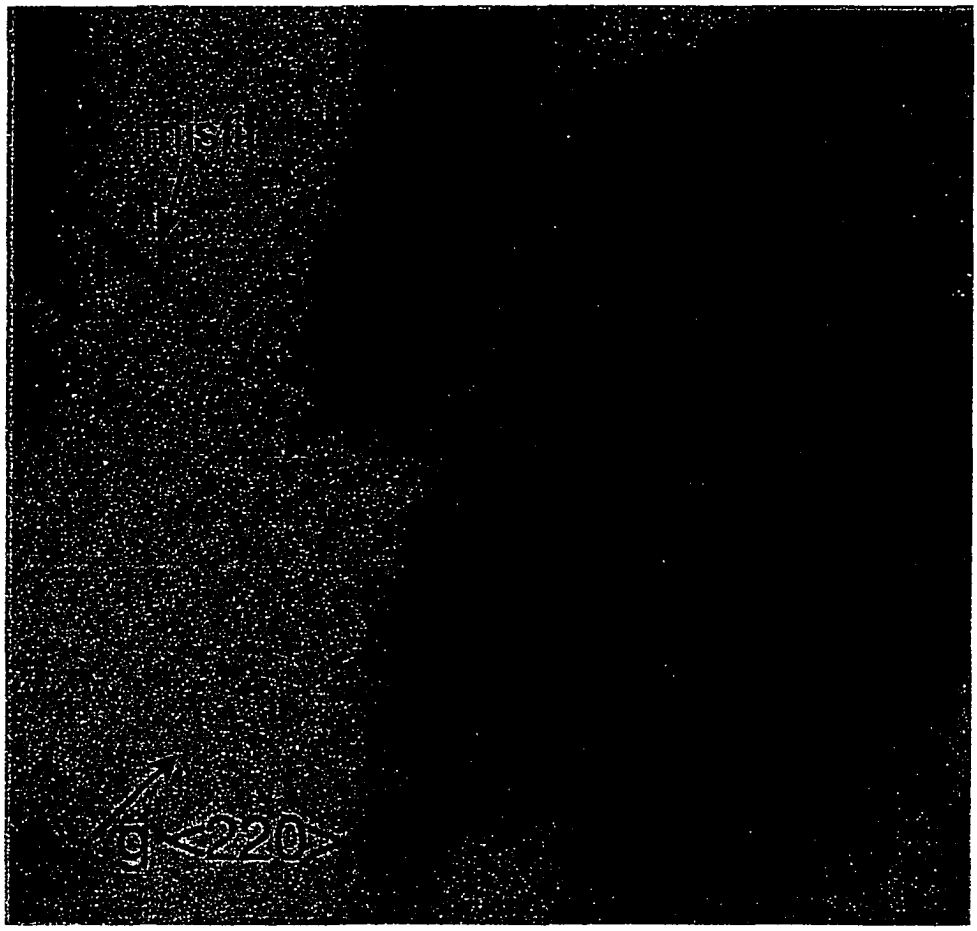

Figure 3-8. Plan-view TEM image for another piece of the sample in Fig. 3-7 also etched 35 s, showing etch pits for both the stacking faults and misfit dislocations.

Figure 3-8 shows the TEM image for another area of the same sample etched for 35 sec. In this case two pits originated from stacking faults like those described above are seen. In addition an etch pit has formed at the threading segment of a misfit dislocation. Thus we conclude that both stacking faults and misfit dislocations are revealed by this etchant. The formation of lines in the later stage of the etch seen in Figures 3-4 and 3-5 indicates that accelerated etching occurs near the strain field of the misfit dislocations.

The good agreement between these two methods (TEM and EPD) suggests that the solution we chose is suitable for the EPD evaluation of $Zn_xCd_yMg_{(1-x-y)}Se$ and that EPD is a useful technique to characterize the lower defect density epilayers where TEM is no longer accurate. It is worth mentioning that this solution does not work on $Zn_xCd_{(1-x)}Se$ or on $Zn_xCd_yMg_{(1-x-y)}Se$ layers with less Mg (for example when the Mg composition is less than 20%).

3-3-2. Improvements of II-VI/III-V interface

The II-VI/III-V interface quality is important to the growth of II-VI material on III-V surface. In the ZnSe/GaAs system, the increasing of the lifetime from a few seconds to more than 100 hours[4] has been achieved by the reduction of defect density in the materials from 10^7 to 10^4 cm^{-2}. It has been shown that improvement of the II-VI/III-V interface is the main reason of the reduction of the defect density. In the case of the growth of ZnSe based materials on GaAs substrates, it is important to avoid any tendency to form a well-ordered Se-(2×1) structure[40] on the GaAs surface. On such surface, the II-VI nucleation is not favorable, isolated islands are easily formed, very high density of stacking faults will be formed from these islands.[41] The methods that have addressed this problem to date have aimed at suppressing this interaction by adjusting the III-V surface stoichiometry.[42] Surface stoichiometry was first proposed as a critical parameter in II-VI/III-V heteroepitaxy by Farrell and Tamargo.[43] By careful adjustment of the surface stoichiometry of the GaAs buffer layer prior to II-VI growth, a defect density in the range of 10^4 cm^{-2} has been reported. Basically, the methods used to adjust the surface stoichiometry of the III-V substrates are: 1). Suitable preparation of the substrate to form a group-V rich surface. 2). Zn irradiation

of the III-V surface before the initial growth of II-VI material.[44, 45] 3). Using migration enhanced epitaxy (MEE) technique.[45]

The II-VI/III-V interface is even more difficult to control in the growth of II-VI materials on InP substrates. The reason is that the congruent evaporation temperature of InP is low compared with the InP deoxidization temperature.[46] So it is harder to get a clean and smooth surface with the correct stoichiometry. Therefore it is hard[16] to initialize the II-VI growth on InP substrates in two dimensional nucleation growth mode at optimized growth temperature. In the following I will describe the progress I have made to improve the quality of II-VI/III-V interface to reduce the defect density.

A. **The preparation of InP substrates**

An important process of the preparation of InP substrates is the deoxidization of InP substrates before the growth. Their deoxidization is more difficult than that of GaAs substrates.[46] GaAs has a congruent evaporation temperature of 650°C while the deoxidization temperature is about 580°C. The use of an As flux is sufficient to protect the GaAs substrate and maintain As-rich conditions. InP has a congruent evaporation temperature of 363°C, but the deoxidization process requires to heat the substrate to about 450-

500°C. In vacuum, this would give rise to the loss of P atoms and formation of In-rich surface on the InP substrate.[46] The excess In may react with Se to form various undesirable interfacial layers.[47] Use of an As flux during deoxidization is expected to minimize this problem. In an ambient of arsenic flux, the phosphorus lost by thermal desorption is replaced by the impinging flux.[48] The use of an As flux during thermal cleaning of InP substrates has been shown to produce a thin InAs layer on the surface.[49-51] This may affect the growth of II-VI layer. One way to solve this problem is to grow a III-V buffer layer which will be discussed later. Because of the easy damage of the surface, it appeared reasonable not to heat the substrates to too high temperature. In the early studies,[16] the substrate was only heated to ~ 420°C and left at this temperature for ~20 to 30 minutes until the RHEED pattern became streaky and bright with a (2×1) reconstruction, indicating the absence of the oxide layer. Later, we found that it is better to heat the substrate quickly to ~470°C and then carefully heat the substrate until the 2-fold in the RHEED pattern changes to 4-fold. Then very quickly reduce the temperature. A clean As stabilized surface can be routinely obtained by using this technique.[17]

B. Initial two-dimensional nucleation growth conditions of II-VI layers

Dai et al[16] found that it is necessary to start the growth of the II-VI epilayer on InP substrate at a low temperature to obtain initial two-dimensional nucleation. In practice, the initial growth temperature was set to 170°C. After 1 min low temperature growth, the growth temperature was increased to 270°C without interruption of the growth. The initial low temperature growth of II-VI layer is expected to reduce the reaction between the Se atoms and the In atoms and allow an ordered II-VI layer to deposit on the III-V surface. Low initial growth temperature has recently been adopted in the growth of ZnSSe on GaAs for the reduction of stacking faults at the interface.[52] We found that after one minute of growth, the growth must be interrupted while increasing the temperature to the optimum growth temperature of 270°C. The rest of the growth is performed at 270°C. Growth interruptions may have two functions: 1). to avoid deposition at low temperatures any longer than necessary. Low temperature growth for too long was found to roughen the growth surface and result in poor quality materials. 2). to smoothen the growth surfaces. Growth interruptions have been used in other materials as a means of smoothening the growth surfaces. [17, 53]

By using the new technique to deoxidize and using growth interruption, the quality of ZnCdSe has been improved. Figure 3-9 shows the 10 K PL and

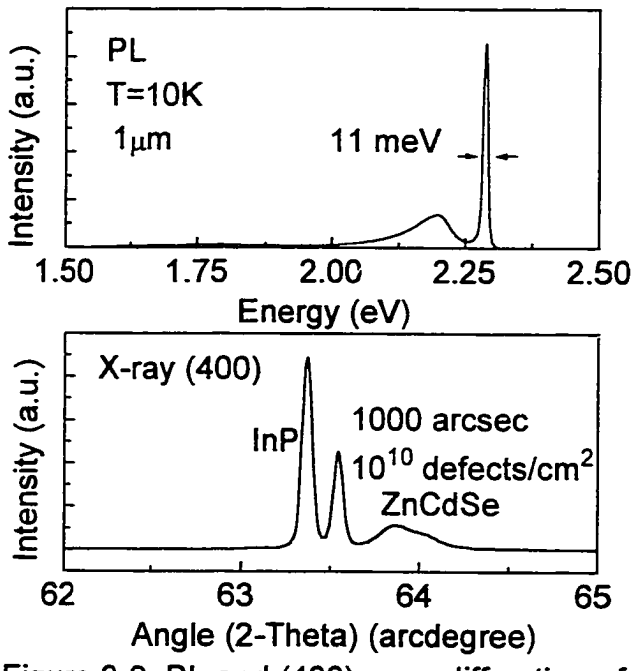

Figure 3-9. PL and (400) x-ray diffraction of ZnCdSe grown without interruption and deoxided at 420°C.

single crystal x-ray diffraction (SCXRD) of 1 μm thick ZnCdSe samples grown without growth interruption and deoxidized at 420°C. The linewidth of band edge emission was ~11 meV. A broad second peak about 100 meV below the band gap was observed, suggesting some impurities in the epilayer. SCXRD exhibits unresolved $K_{\alpha 1}$ and $K_{\alpha 2}$ peaks as shown in Fig. 3-9(b). FWHM of the x-ray peaks were determined from double-crystal X-ray rocking curves to be greater than 1000 arcsec.

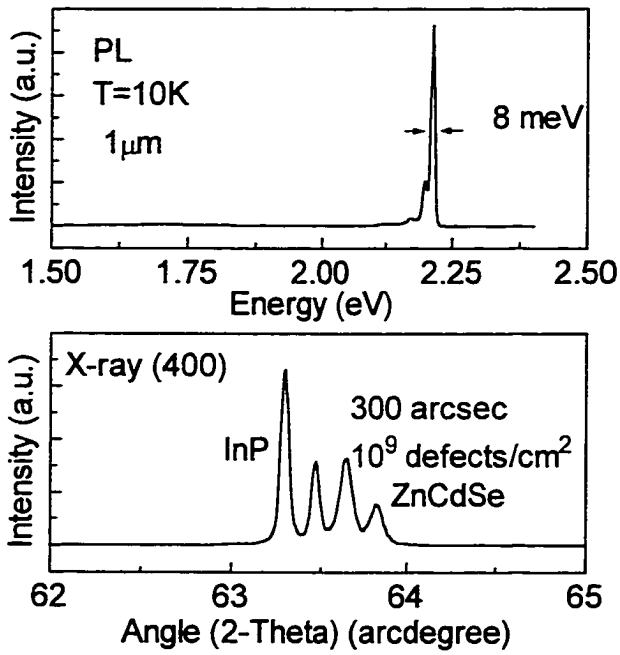

Figure 3-10. PL and (400) x-ray diffraction of ZnCdSe grown with interruption and deoxided at 490°C.

As a comparison, sharp and intense band edge emission with a linewidth of 8 meV was obtained from 1 μm thick ZnCdSe samples grown with growth interruption and deoxidized at 490°C as shown in Fig. 3-10 (a). No deep level was observed, indicating good optical quality in these epilayers, Fig. 3-10(b) shows the SCXRD of this sample. The $K_{\alpha 1}$ and $K_{\alpha 2}$ peaks are well resolved, meaning much narrower peaks. Double crystal x-ray rocking curves (DCXRC) exhibit FWHM of ~300 arcsec. Defect densities were determined by plan-view TEM to be 5×10^9 defects/cm^2.

C. II-VI growth with III-V buffer layers

Although improved layer quality was achieved with the conditions described above, accurate control of the III-V surface is best achieved by using InGaAs or InP as buffer layers.[14-15] The InGaAs buffer layers were grown at 460°C with As beam equivalent pressure of ~2×10^{-5} Torr and

growth rate of 1 μm per hour. RHEED patterns during and after the growth were streaky (2×4). For InP growth, polycrystalline InP was used as the P source. The substrates were deoxidized also under As beam. After the deoxidization, in order to avoid unintentional incorporation of As into the InP buffer layer, the As cell temperature was reduced to a standby temperature (less than 150°C) and the substrate temperature was decreased to ~ 200°C to wait for 30 minutes until the As background in the chamber was reduced. Then the substrate temperature was increased to the growth temperature of ~400 °C and growth was started. The P pressure was 5×10^{-6} Torr. The growth rate was 0.5 μm. The RHEED pattern was very bright and remained very streaky (2×4) throughout the growth. The thickness for both kinds of buffer layers was in the range of 500-1000 Å. Once the growth of buffer layers was finished, the shutters of group III elements were closed, the substrates with the buffer layers were protected under the group V elements (either As or P) while the substrate temperature was reduced. At 300°C, the shutter of group V element was closed. The substrates with the buffer layer were transferred immediately in vacuum to the II-VI chamber for the growth of II-VI materials.

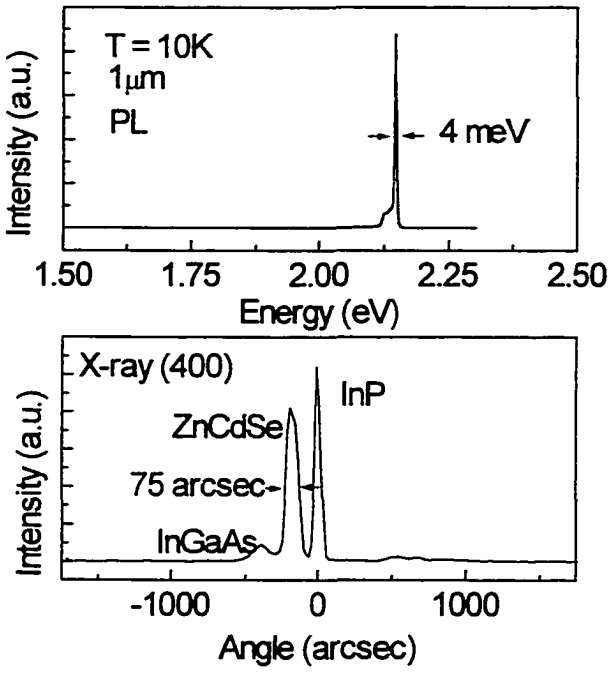

Fig. 3-11. PL and double crystal x-ray (400) rocking curve of ZnCdSe layer grown with InGaAs buffer layer.

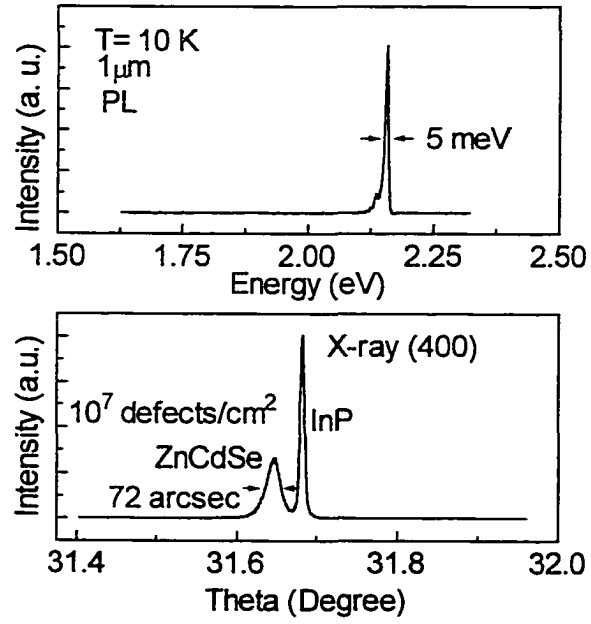

Fig. 3-12. PL and double crystal x-ray (400) rocking curves of ZnCdSe layer grown with InP buffer layer.

Characterization of ZnCdSe epilayers grown on the III-V buffer layers showed dramatic improvements in epilayer quality. Figure 3-11 shows an x-ray rocking curve and a 10 K PL spectrum for a 1 μm thick ZnCdSe layer grown on an InGaAs buffer layer. Figure 3-12 shows a x-ray rocking curve and a 10 K PL spectrum for a 1 μm thick ZnCdSe layer grown on an InP buffer layer. The quality of ZnCdSe layers grown on either InGaAs or InP buffer layer is similar. PL data exhibited bandedge emissions with FWHM of 4-5 meV and no deep level emission. The DCXRC curves revealed peaks with FWHM of ~70 arcsec.

Figure 3-13 shows plan view bright field TEM images of a ZnCdSe layer grown on (001) InP substrate (a) without and (b) with an InP buffer layer. The scale is the same for both images. A high density (5×10^9 defects/cm^2) of stacking faults is present in the film in Fig. 3-13(a). They appear in the image as either a V-shaped set of partial dislocations or a triangle of interference fringes. The faults lie on {111} planes. They start in a point at the III-V/II-VI heterointerface and grow wider towards the surface of the film. The defect density in Fig. 3-13(b) forms a sharp contrast with the image in Fig. 3-13(a). The density of stacking fault pyramids in the layer is 5×10^7 cm^{-2}, two orders of magnitude lower than in the film grown without the InP buffer layer. In both films, the stacking faults are determined to be of Shockley type.[54] No misfit dislocations [which in (001) zinc-blend are directed in <110>] are observed in either sample, indicating that the layers are pseudomorphic to the substrates. The ZnCdSe samples grown with InGaAs buffer layers have similar defect density, in the range of 10^7 cm^{-2}. This suggests that the chemical differences between phosphides and arsenides are not significant at the II-VI/III-V heterointerface when a smooth, high quality epitaxial surface is provided for the II-VI growth.

As seen from the above results, both the crystalline quality and optical quality of ZnCdSe grown on InP can be remarkably improved by inserting

either an InGaAs or an InP buffer layer. This clearly indicates that the III-V buffer layers play an important role in improving II-VI material quality. The III-V buffer layer has two effects: 1). To produce a clean, smooth and less-defected growth surface for the subsequent two-dimensional layer-by-layer growth. The stacking faults all nucleate in pairs at the interface between the InP and the ZnCdSe layer. Surface imperfections such as small amounts of residual oxide, vacancies and roughness might act as nucleation sites for stacking faults, because they impede two-dimensional growth. By growing a III-V buffer layer, imperfections may be buried and structural quality is restored. 2). To control the III-V surface stoichiometry before the II-VI growth. As we have mentioned in the introduction section, surface stoichiometry is a critical parameter in II-VI/III-V heteroepitaxy. It has been reported that, in MBE growth of ZnSe on (001) GaAs, high quality ZnSe can be obtained only when the growth is performed on an As-stabilized (2×4) surface.[55, 56] The growth on a Ga-stabilized surface or an excess As covered c(4×4) surface gives poor quality and high defect density. For our materials grown on InP, a similar behavior is expected. When the (001)InP surface is thermally deoxidized under an As beam, several monolayers of InAs form by the exchange between As and P.[49-51] Although (001) InAs shows a similar reconstruction as GaAs, the (2×4) RHEED pattern of InAs formed on the InP

surface by thermal deoxidization frequently shows a disordered feature such that the 4-fold pattern can not be observed.[51] With a III-V buffer layer, very well defined RHEED patterns with precise surface reconstructions can be obtained for either InGaAs or InP surface.

In conclusion, by growing a III-V buffer layer (either InGaAs or InP) to control the surface stoichiometry and to produce a clean, smooth surface, the quality of ZnCdSe layers has been improved dramatically. The linewidth of band edge emission for a 1μm thick ZnCdSe sample was ~ 5 meV while DCXR curves revealed peaks with FWHM of 70 arcsec. Defect densities were reduced two orders of magnitude, to 10^7 cm^{-2}.

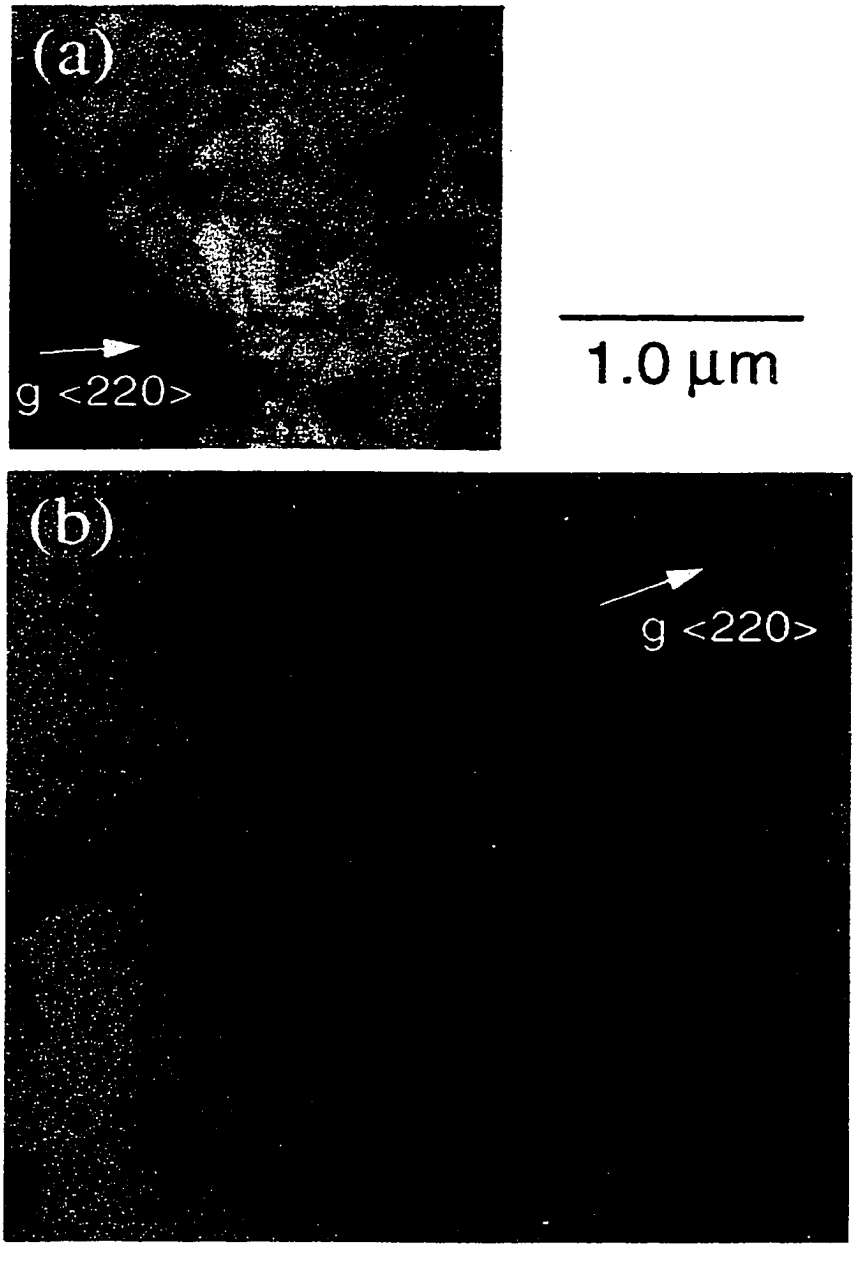

Figure 3-13. Plan-view TEM images of a ZnCdSe layer grown on (001) InP substrate (a) without and (b) with an InP buffer layer.

D. ZnCdSe interfacial layer

We have shown that the III-V buffer layer,[14, 15] low temperature growth[16] and growth interruption[17] are essential to improve the quality of ZnCdSe ternary layers. By using these techniques, the quality of ZnCdSe was dramatically improved. The FWHM of DCXRC for a typical ZnCdSe layer was about 70 arcsec, the PL linewidth was about 5 meV at 10K and the defect density was about 10^6-10^7 cm^{-2}. But using the same techniques to grow $Zn_xCd_yMg_{(1-x-y)}Se$ layers, the quality of the quaternaries is not as good, and it is necessary to further improve the quality of $Zn_xCd_yMg_{(1-x-y)}Se$ layers grown on InP substrates.

The $Zn_xCd_yMg_{(1-x-y)}Se$ quality was optimized further by initiating the II-VI growth with a lattice-matched ZnCdSe interfacial layer.[19] This layer was grown during the initial growth at 170°C, followed by a growth interruption. Once the substrate temperature reached 270°C, the $Zn_xCd_yMg_{(1-x-y)}Se$ layer growth started. With these changes a dramatic narrowing of the x-ray peaks was observed.

Figure 3-14 shows the 77K photoluminescence (PL) and double crystal x-ray rocking curve (DCXRC) for a typical $Zn_xCd_yMg_{(1-x-y)}Se$ layer with a InP buffer layer grown without the ZnCdSe interfacial layer. The PL shown in Fig. 3-14(a) had a strong and narrow bandedge emission peak. In the low energy side, there was a very small and weak deep-level peak. The $Zn_xCd_yMg_{(1-x-y)}Se$ epilayer was almost lattice-matched to the InP substrate and had a full width at half maximum of double crystal x-ray rocking curves (DCXRC) of about 460 arcsec, shown in Fig. 3-14(b). The defect density evaluated from the etch pity density study was about 10^9 cm^{-2}.

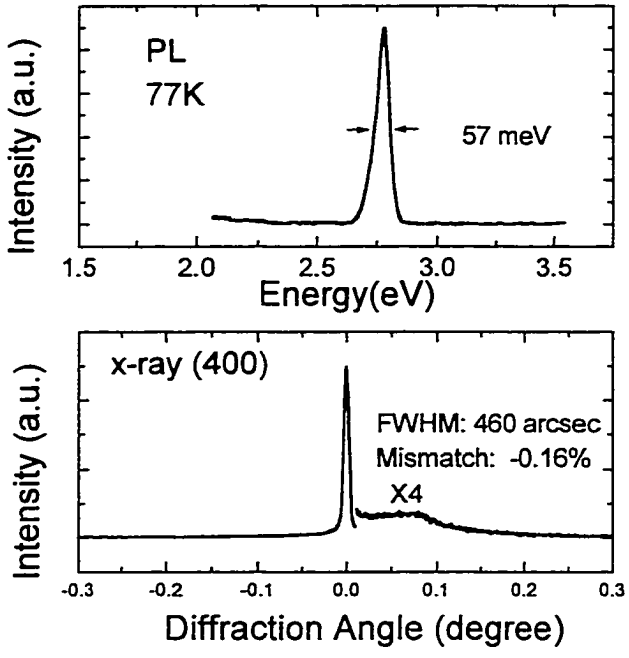

Fig. 3-14. PL and double crystal x-ray (400) rocking curves of ZnCdMgSe layer with only III-V buffer layer.

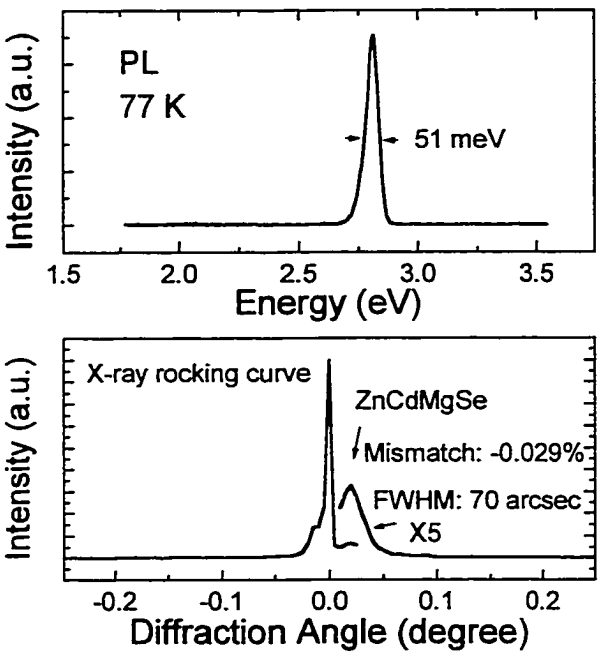

Fig. 3-15. PL and double crystal x-ray (400) rocking curves of ZnCdMgSe layer with both III-V buffer layer and ZnCdSe interfacial layer.

As a comparison, Figure 3-15 shows the 77K photoluminescence and DCXRC for a typical $Zn_xCd_yMg_{(1-x-y)}Se$ epilayer grown with both InP buffer layer and ZnCdSe interfacial layer. The bandgap and lattice mismatch were similar to the sample shown in figure 3-14. The 77K PL shown in Fig. 3-15(a) had strong symmetrical bandedge emission peak with a slightly narrower linewidth. There was no any deep-level peak. The DCXRC (Fig. 3-15(b)) showed strong peak of the $Zn_xCd_yMg_{(1-x-y)}Se$ layer with a full width at half maximum of about 70 arcsec which was much less than the 460 arcsec shown in figure 3-14. The defect density of this sample was about 10^6 cm^{-2}.

Figure 3-16 shows plan view TEM images of two $Zn_xCd_yMg_{(1-x-y)}Se$ layers similar to those of Fig. 3-14 and 3-15. The two samples have a comparable bandgap of ~3.0 eV, a similar lattice mismatch (~0.2%) and the Mg fraction of ~0.54. Fig. 3-16(a) shows the TEM image of the sample with

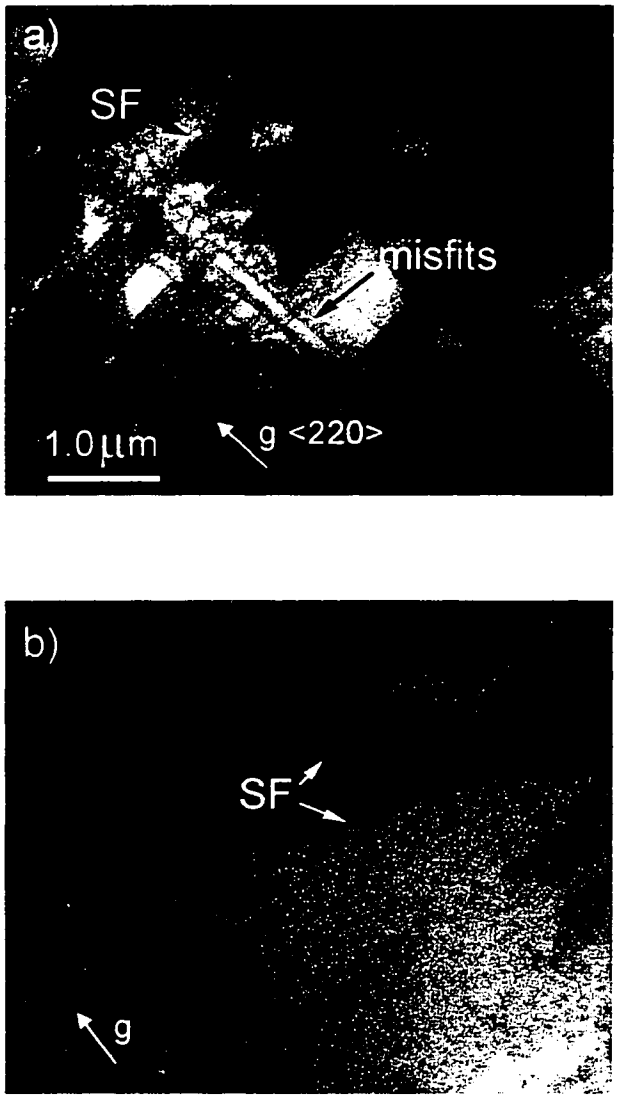

Figure 3-16. Plan-view TEM for ZnCdMgSe layers without (a) and with (b) ZnCdSe interfacial layer.

a quaternary interfacial layer. A high density of stacking faults and threading dislocations associated with misfit dislocations are observed. The density of stacking faults is in the 10^9 cm^{-2} range. Threading dislocations associated with misfit dislocations may be suggestive of three dimensional nucleation. The plan-view TEM image [Fig. 3-16(b)] of the quaternary layer with a ternary interfacial layer shows a strong contrast with Fig. 3-16(a). The density of stacking faults is much less, $\sim 10^7$ cm^{-2}, and no threading dislocations associated with misfit dislocations are seen. This suggests[57] that two-dimensional nucleation has been achieved in the II-VI layer by the use of a thin ZnCdSe interfacial layer.

The Mg fraction has strong effect on the $Zn_xCd_yMg_{(1-x-y)}Se$ PL linewidths.[18, 58] In order to examine the effect of the thin ZnCdSe interfacial layer on the quality of $Zn_xCd_yMg_{(1-x-y)}Se$ with various Mg fractions (and thus various bandgaps), we measured the relationships of the 77K PL linewidths and FWHM of DCXRC with Mg fraction for two sets of $Zn_xCd_yMg_{(1-x-y)}Se$ layers, one set grown with quaternary interfacial layers and the other with ternary interfacial layers. The data are shown in figure 3-17. The Mg fractions were calculated from the PL and x-ray data by assuming the epilayer is fully relaxed. From Fig. 3-17(a), it is clear that the PL linewidths of the band edge emission for both sets of samples increase linearly with increasing Mg

fraction. However, for the same Mg fraction, the PL linewidths for samples with a ternary interfacial layer are slightly smaller than those for the samples with a quaternary interfacial layer, but the difference is very small. From Fig. 3-17(b), we note that, for Mg fractions from 0 to 0.55, the FWHM of DCXRC for the $Zn_xCd_yMg_{(1-x-y)}Se$ epilayers with the ternary interfacial layer is invariant and almost the same as that of ZnCdSe ternary layers.[14, 15] EPD and TEM data show that these quaternaries all have similar defect densities, in the 10^6 -10^7 cm^{-2} range. When the Mg fraction increases above 0.55 (for bandgap of 3.1 eV and higher), the FWHM appears to increase very rapidly. By contrast, the FWHM of DCXRC for $Zn_xCd_yMg_{(1-x-y)}Se$ layers with quaternary interfacial layer increases rapidly even when the Mg fraction is as low as about 0.15. We conclude that the range of Mg composition, for which the $Zn_xCd_yMg_{(1-x-y)}Se$ layers have the same quality as ZnCdSe layers, has been greatly extended by incorporating a ZnCdSe interfacial layer at the II-VI/III-V interface. At present, we have grown $Zn_xCd_yMg_{(1-x-y)}Se$ epilayers with bandgaps up to 3.05 eV with similar quality as ZnCdSe layers.

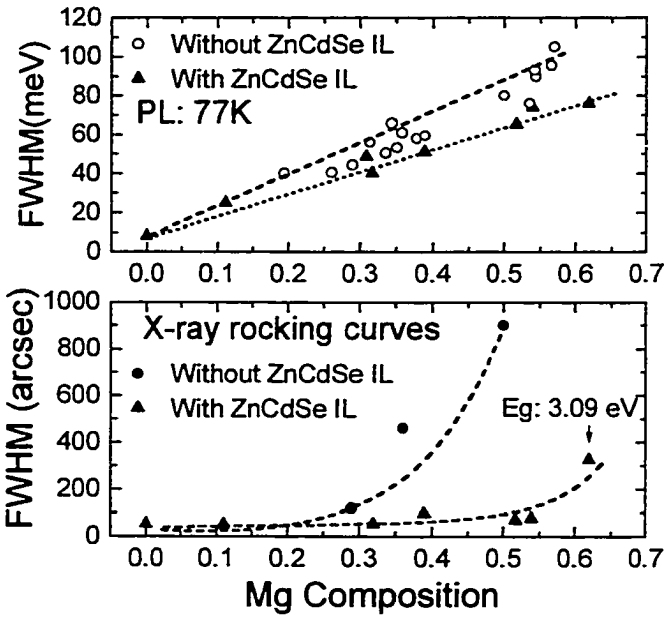

Figure 3-17. Dependence of PL linewidth and FWHM of x-ray (400) rocking curves on Mg composition for ZnCdMgSe grown without and with ZnCdSe interfacial layer (IL).

As shown in figure 3-17, the PL emission linewidth did not improve very much with the ternary interfacial layer. In addition, these linewidths are broader than expected based on alloy broadening considerations. On the other hand, the FWHM of the DCXRC for the $Zn_xCd_yMg_{(1-x-y)}Se$ layers with Mg fraction below 0.55 and the defect density was reduced dramatically. This suggests that the stacking faults in the epilayers are not causing the broadening of the PL linewidths. We will discuss this issue further in chapter 4.

In summary, by incorporating a thin ZnCdSe interfacial layer grown at low temperature on the III-V buffer layer, the quality of $Zn_xCd_yMg_{(1-x-y)}Se$ epilayers with bandgaps as high as 3.05 eV has been greatly improved and has become equivalent to that of ZnCdSe layers. In terms of stacking faults, the quality of the quaternary layers appears to be limited to that of the ZnCdSe interfacial layer. This suggests that further improvements in quality

will require that the ZnCdSe nucleation be optimized. Some steps that may achieve this are the use of migration enhanced epitaxy (MEE)[59] or Zn irradation[57, 59, 60] steps at the initiation of growth.

E. Zn irradiation and MEE growth

In the growth of ZnSe on GaAs, it has been found that the interaction of Se with the substrate surface, forming Ga_2Se_3,[61] reduces the epilayer and interface quality. One of the techniques to avoid this problem is using Zn irradiation,[57, 59, 60] that is, exposure of the III-V surface to Zn before the II-VI growth to avoid the interaction of Se with the III-V surface. In our case, we expect that a similar interfacial compound such as In_2Se_3 and Ga_2Se_3 may form at the II-VI/III-V interface and maybe limit the quality of the layer. Therefore using Zn irradiation to further avoid this kind of interaction should improve the surface quality and thus the epilayer quality. MEE[59] is a modification of the MBE growth technique in which the growing surface is alternately exposed to the beams that compose the alloy by alternately opening the cell shutters. Exposure of the surface to only one element at a time can allow for increased surface migration of that species. It is a very useful technique to achieve a two-dimensional nucleation growth. In the growth of II-VI on InP substrates, a low temperature initial growth is

necessary. To guarantee that excessive Zn does not deposit at these low temperatures, a modification of the Zn irradiation process and MEE growth have been developed.

In this work, we have tried both Zn irradiation and MEE growth at 170°C. One period of MEE growth included the opening of shutters of Zn, Se, Cd, Se in order, each for 10 seconds. After each shutter was closed and before the next shutter was open, there was ~ 5 seconds waiting time to allow the excess atoms or molecules on the surface to evaporate. It was noted that, once the MEE growth started, the RHEED pattern became less well defined and slightly spotty. After the MEE growth, the growth was interrupted and the substrate temperature was increased to 270°C to start the growth under normal conditions. As soon as the normal growth started, the RHEED pattern changed to a good (2×1) pattern. We have grown $Zn_xCd_yMg_{(1-x-y)}Se$ samples with MEE periods from 4 to 10 and found that the MEE growth performed under these conditions did not have much affect to the quality of the II-VI layer. Too low migration rates of Zn and Cd atoms on the surface at our low temperature may be the reason.

Because of the low growth temperature (170°C), the time of Zn irradiation was set to only 15 sec to avoid excess Zn condensation on the surface. In order to avoid the Se background in the II-VI chamber, the Se

shutter was closed at least 5 minutes before transferring the substrate with the buffer to the II-VI chamber. The Zn shutter was kept open (the main shutter was closed). The Zn irradiation was done as follows: once the substrate with the buffer layer was transferred to the II-VI chamber, the substrate was heated to 170°C. When the temperature was stable, the main shutter was opened (the Zn shutter was already open) for 15 seconds. Then the Cd and Se shutters were opened to start the growth of ZnCdSe interfacial layer. The rest of the growth procedure was the same as before. In order to avoid forming misfit dislocations, thin $Zn_xCd_yMg_{(1-x-y)}Se$ samples (~1000 Å) with bandgaps of ~ 3.0 eV were grown in this experiment. At this thickness, the samples are expected to be pseudomorphic. We found that very short time Zn irradiation before the II-VI growth improves the quality of II-VI layers dramatically. The defect density of $Zn_xCd_yMg_{(1-x-y)}Se$ layers with bandgap of 3.1 eV at 77K has been reduced to mid-10^4 cm^{-2} range by this technique.

Figure 3-18 shows Nomarski micrographs of the etched surface of a $Zn_xCd_yMg_{(1-x-y)}Se$ sample grown (a)without Zn irradiation and (b) with Zn irradiation. The etchant is hydrobromic acid and acetic acid solution at a concentration of 1:7 by volume. The etch time was the same for both samples, ~ 1 min. It is clear that the shape of the etch pits for both samples is the same. The etch pit density evaluated from Fig. 3-18(a) for a $Zn_xCd_yMg_{(1-x-y)}Se$

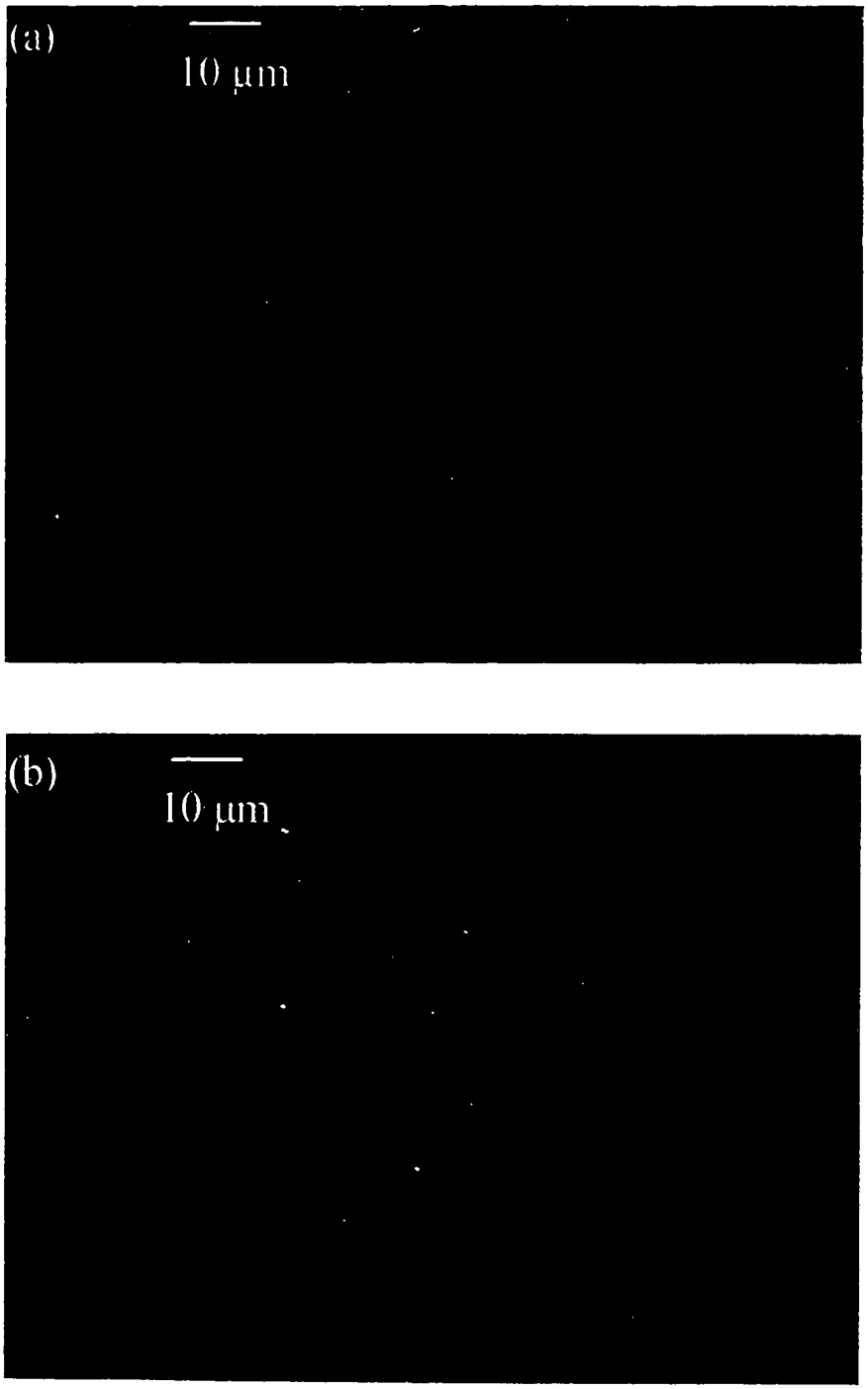

Figure 3-18. The Nomarski micrographs of the etched surface of ZnCdMgSe samples (a) without Zn irradiation and (b) with Zn irradiation.

epilayer without Zn irradiation is ~ 5×10^6 cm^{-2}. In contrast, the EPD evaluated from Fig. 3-18(b) for a $Zn_xCd_yMg_{(1-x-y)}Se$ sample with 15 second Zn irradiation is much less, ~ 5×10^4 cm^{-2}. So, by using Zn irradiation, the EPD of $Zn_xCd_yMg_{(1-x-y)}Se$ epilayers has been reduced about two orders of magnitude. For these improved samples the PL intensity appears to be stronger even though the width does not change much. The x-ray peak is strong and sharp. The FWHM has been reduced to ~ 50 arcsec (see Fig. 5-10).

3-3-3. Summary of quality improvements of $Zn_xCd_yMg_{(1-x-y)}Se$ materials

The quality improvements of ZnCdSe and $Zn_xCd_yMg_{(1-x-y)}Se$ layers are summarized in table II. We conclude that:

1. By using III-V buffer layer, low temperature growth and growth interruption, the quality of ZnCdSe layers has been improved dramatically. The PL line width has been reduced to 4-5 meV. The FWHM of x-ray rocking curves has been reduced to ~70 arcsec. The defect density has been reduced to ~10^7 cm^{-2}.
2. By using the same techniques as above to grow $Zn_xCd_yMg_{(1-x-y)}Se$ layers, the quality improvements are not so pronounced. A typical $Zn_xCd_yMg_{(1-x-}$

$_{y)}$Se layer with bandgap of 2.8 eV has the PL line width of ~57 meV, the FWHM of x-ray rocking curves of ~ 460 arcsec and EPD of 10^9 cm^{-2}.

3. By using a ZnCdSe interfacial layer, the quality of $Zn_xCd_yMg_{(1-x-y)}Se$ layers has been improved dramatically and has reached the same quality of ZnCdSe layers.
4. Further quality improvements of $Zn_xCd_yMg_{(1-x-y)}Se$ layers have been obtained by using Zn-irradiation. By this step, the EPD has been reduced to mid - 10^4 cm^{-2}.

Table II Quality of ZnCdSe and $Zn_xCd_yMg_{(1-x-y)}Se$ layers grown with different initial growth conditions

		Line width of PL (meV)	FWHM of x-ray (arcsec)	Defect density (cm^{-2})
ZnCdSe (1 μm)	LT	11	900	$>10^9$
	LT + GI	8	300	10^8 - 10^9
	III-V + LT + GI	4 - 5	60 - 70	10^6 - 10^7
ZnCdMgSe (1 μm with band-gap of 2.8 eV)	LT + GI	60	no peak	$>10^{10}$
	III-V + LT + GI	57	460	$\sim10^9$
	III-V+LT-ZnCdSe + GI	51	70	10^6 - 10^7
	III-V + ZI+ LT-ZnCdSe + GI		50-60	10^4-10^5

where LT means low-temperature growth; GI means growth interruption; III-V means III-V buffer layer; LT-ZnCdSe means low temperature grown ZnCdSe interfacial layer; ZI means Zn-irradiation.

CHAPTER 4

Characterization of $Zn_xCd_yMg_{(1-x-y)}Se$ layers

4-1. Double crystal x-ray rocking curve measurements

The double crystal x-ray rocking curve (DCXR) measurement is a very direct and useful way to evaluate the quality of the epitaxial layer and the lattice mismatch between the epitaxial layer and the substrate.[62] This technique is particularly useful for epitaxial layers grown on a thick substrate. In general, for such cases, two diffraction peaks are observed, one from the substrate and one from the epilayer. From the peak width, we can evaluate the material quality. From the peak separation, we can obtain information about the lattice-mismatch. We have measured double crystal x-ray rocking curves for our samples to evaluate their quality. We have also used the peak separation between the substrate and the epilayer in the (400) reflection to evaluate the lattice-mismatch by assuming the epilayer is fully relaxed. From the lattice-mismatch and the PL peak energy which corresponds to the bandgap, the composition in our $Zn_xCd_yMg_{(1-x-y)}Se$ was calculated. In this part of the work, besides continuing to use double crystal x-ray rocking curves to

evaluate the quality of the epilayers, we will also use this technique to evaluate the level of strain or strain state of the epitaxial layers.

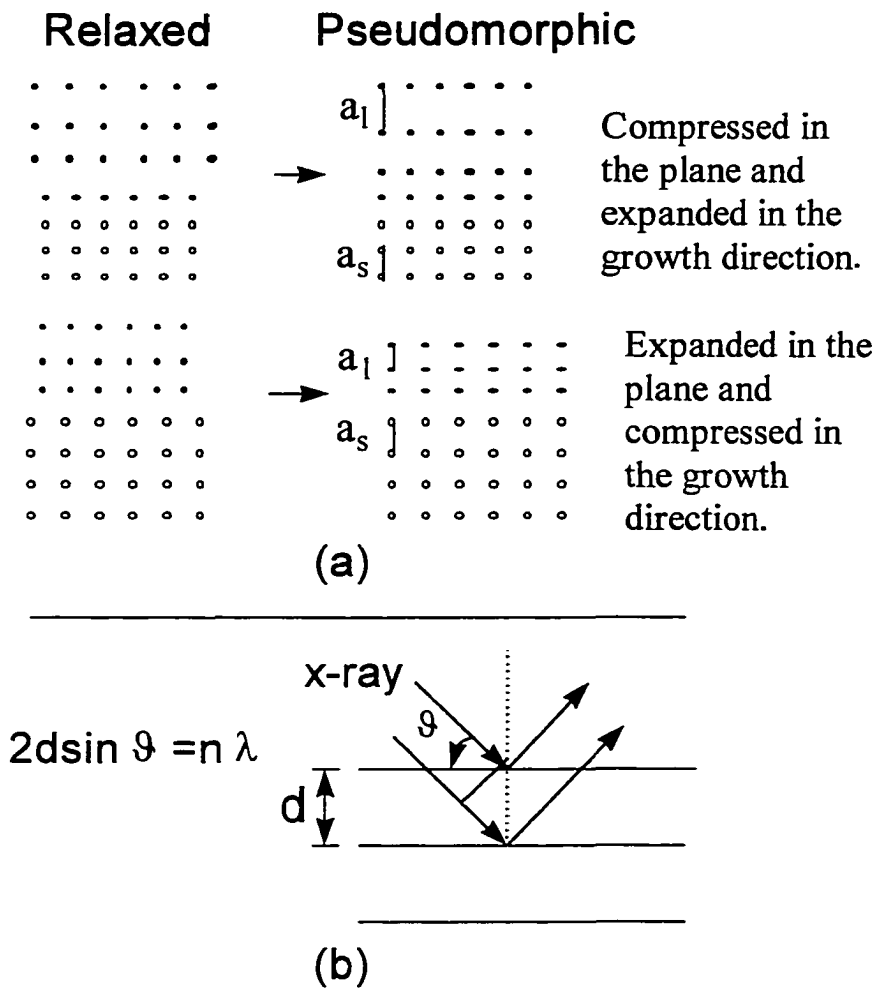

Fig. 4-1. (a) Possible strain states in the epilayers. (b) Principle of x-ray diffraction.

The strain state of the epitaxial layer is an important parameter. With the same thickness and lattice-mismatch, the layer that is pseudomorphic has better quality than a relaxed or partially relaxed layer. In the laser structure, we need to make sure the whole structure is pseudomorphic. In the

calculation of composition, we also need to know the strain state in the epilayer. Usually, for a system consisting of an epilayer and a substrate with a different lattice-constant, the epilayer could be either fully strained, partially strained, or fully relaxed. When the thickness of the epilayer is less than a certain thickness (critical thickness), the epilayer will be pseudomorphic or fully strained, and the tetragonal structure will be distorted, as shown in figure 4-1(a). The parallel lattice-mismatch in the plane between the epilayer and the substrate will be zero. The perpendicular lattice mismatch $[\Delta a/a_s|_\perp = (a_\perp - a_s)/a_s]$ in the growth direction will be approximately two times larger for a fully strained layer than the relaxed (real) lattice-mismatch between the epilayer and the substrate. When the thickness of the epilayer is larger than the critical thickness, the epilayer will be partially or fully relaxed. In the case of a fully relaxed layer, the parallel and perpendicular lattice-mismatch will be the same and equal to the real lattice-mismatch between the epilayer and the substrate. Depending on whether the epilayer is fully strained or fully relaxed, the peak separation between the substrate and the epilayer in the (400) reflection will differ by about a factor of two, i.e., the relaxed layer will have a peak separation which is about half the separation that would be observed if that layer was fully strained. Therefore, it is important to know the strain state of the epilayer when using the measured peak separation in the (400)

reflection to calculate the composition. Since the x-ray diffraction measures the spacing of the reflection planes, as shown in figure 4-1(b), the rocking curves from different reflections will give different information. In this work, both symmetric (400) and asymmetric {511} x-ray rocking curves have been used to study the strain state of our $Zn_xCd_yMg_{(1-x-y)}Se$/InP materials. The rocking curves from the (400) reflection contain only the information of perpendicular lattice mismatch. While the rocking curves from the {511} reflections contain the information of both perpendicular and parallel lattice mismatch.[63] From these data, we have calculated both the perpendicular and parallel lattice mismatch.

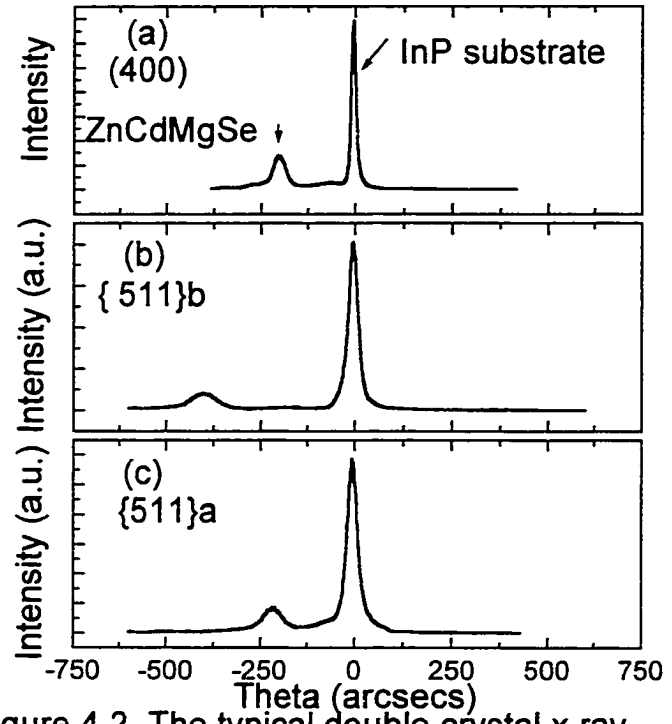

Figure 4-2. The typical double crystal x-ray rocking curves in reflections of (400), $\{511\}_a$ and $\{511\}_b$ from a pseudomorphic ZnCdMgSe layer grown on InP.

The typical (004), $\{511\}_a$ and $\{511\}_b$ x-ray rocking curves are shown in figure 4-2(a), (b) and (c), respectively. When doing the x-ray (004) and {511} measurements, attention has been paid to the film tilt by rotating the samples. No film tilt was observed. The subscripts a and b represent {511} reflection geometries with x-ray incident angle of $\vartheta+\varphi$ and $\vartheta-\varphi$, respectively. It is clear that the peaks from the {511} reflection were broader than the peaks from the (400) reflection. The peak separation from $\{511\}_a$ was very close to the peak separation from (400). The peak separation from $\{511\}_b$ was almost double the peak separation from $\{511\}_a$. By measuring peak separations ω_a and ω_b, both representing angles separating the epilayer and the substrate in the corresponding $\{511\}_a$ and $\{511\}_b$ x-ray rocking

curves, the perpendicular and parallel lattice mismatches can be determined as follows:[63]

$$(\Delta a/a_s)_\perp = (a_\perp - a_s)/ a_s$$

$$= \sin \vartheta \times \cos \varphi /[\sin\{\vartheta+(\omega_a+ \omega_b)/2\}\times\cos\{\varphi+(\omega_b- \omega_a)/2\}]-1 \qquad (4\text{-}1)$$

$$(\Delta a/a_s)_\parallel = (a_\parallel - a_s)/ a_s$$

$$= \sin \vartheta \times \sin \varphi /[\sin\{\vartheta+(\omega_a+ \omega_b)/2\}\times\sin\{\varphi+(\omega_b- \omega_a)/2\}]-1 \qquad (4\text{-}2)$$

where ϑ=43.0031° and φ=15.7932° are the Bragg angle and the angle spanning the (001) and {511} diffraction planes of the substrate, respectively.

The perpendicular and parallel lattice mismatches evaluated from {511} x-ray measurements for a few samples with ~ 0.85 μm thick $Zn_xCd_yMg_{(1-x-y)}Se$ layer grown on InP are listed in Table I. From (400) x-ray measurements, we also can calculate the perpendicular mismatch:

$$(\Delta a/a_s)_\perp = (a_\perp - a_s)/ a_s$$

$$= \sin \vartheta/\sin(\vartheta+\omega)-1 \qquad (4\text{-}3)$$

where ω is the peak separation in the x-ray (400) rocking curve. The data are also listed in Table I to compare to the perpendicular mismatches evaluated from {511} measurements. It can be seen that the results from the two methods agree well (better than 10%). From the Table, we also can see that

due to the lattice mismatch, the epilayer was deformed from cubic to tetragonal with $a_{\perp}>a_{\parallel}$. In these samples, $(\Delta a/a_s)_{\parallel} \approx 0$, which implies that the lattice in the plane of the epilayer is completely accommodated by the internal strain and that the whole structure is coherently grown on the InP substrate without relaxation. Because the layer thickness of $Zn_xCd_yMg_{(1-x-y)}Se$ in those samples is ~ 0.85 μm and the $(\Delta a/a_s)_{\perp}$ is as high as 0.589%, the fact that the whole structure is still pseudomorphic means the critical thickness is very large. In order to accommodate such large level of strain we conclude that the crystal is highly perfect and the growth conditions are good. As those layers are still pseudomorphic, the strain-free lattice constant can not be obtained from only the (400) x-ray rocking curves. So the composition of the $Zn_xCd_yMg_{(1-x-y)}Se$ layers can't be calculated from the (400) x-ray rocking curves and PL. To obtain the strain-free lattice constant, we must use the x-ray results from {511} reflections and the elastic theory. According to the solution of Hooke's law with biaxial stresses, the perpendicular and parallel strains in the epilayer are related by the Poisson effect so that:

$$\varepsilon_{\perp}/\varepsilon_{\parallel} = -2\nu/(1-\nu),$$

$$\varepsilon_{\perp} = (a_{\perp}-a_f)/a_f$$

$$\varepsilon_{\parallel} = (a_{\parallel}-a_f)/a_f$$

$$a_f=[(1-\nu)/(1+\nu)]\, a_{\perp}+[(2\nu/(1+\nu)]\, a_{\parallel} \qquad (4\text{-}4)$$

where ν is the Poisson ratio of the film and a_f is the free standing lattice constant of the $Zn_xCd_yMg_{(1-x-y)}Se$ layers. By assuming ν=0.28 which is the value for ZnSe,[64] a_f can be obtained: $a_f = 0.5625\, a_{\perp} + 0.4375\, a_{\parallel}$. Using a_f and the PL data, the composition can be calculated. The data of a_f and strain-free lattice mismatch $\Delta a/a_s$ are also listed in Table I, where we have used the lattice constant of InP (5.8682 Å).

In summary, by measuring the x-ray in the {511} reflection, we obtained information about the strain state in $Zn_xCd_yMg_{(1-x-y)}Se$ layers and found that thick $Zn_xCd_yMg_{(1-x-y)}Se$ epilayers with as much as ~0.59% perpendicular lattice-mismatch (~0.34% for the strain-free lattice-mismatch) are still pseudomorphic, which suggests good quality and near-optimal growth conditions. Similar measurements for ZnMgSSe materials suggest that relaxation occurs at much smaller strains (<0.2%). From the x-ray data in the {511} reflection, we have calculated the strain-free lattice constant which is required in the calculation of the composition.

Table I. Calculated perpendicular and parallel lattice mismatches from {511} x-ray measurements compared with the perpendicular lattice mismatches from (400) x-ray measurements.

	Raw data			Calculated mismatch			Strain-free	
Sample	$\omega_{(400)}$ (arc s)	$\omega_{\{511\}b}$ (arc s)	$\omega_{\{511\}a}$ (arc s)	$(\Delta a/a)_{\parallel\{511\}}$ (10^{-3})	$(\Delta a/a)_{\perp\{511\}}$ (10^{-3})	$(\Delta a/a_s)_{\perp(400)}$ (10^{-3})	a_f (Å)	$\Delta a/a_s$ (10^{-3})
1	-281.9	-478.4	-225.5	-0.33	2.01	2.23	5.874	0.99
2	-198.3	-398.7	-212.3	-0.0	1.72	1.56	5.874	0.99
3	-456.8	-404.0	-824.1	-0.04	3.40	3.60	5.878	1.67
4	-749.0	-1365.0	-735.0	0.1	5.94	5.89	5.888	3.37

4-2. Temperature dependence of the photoluminescence

From the study of the temperature dependence of the photoluminescence one can learn about the material properties and the expected device performance. For example, from the temperature dependence of the PL peak energy, we have obtained the bandgap dependence on temperature for $Zn_xCd_yMg_{(1-x-y)}Se$ layers with various composition which is useful for the design of lasers and light emitters. Furthermore, we have shown that the PL linewidths increase linearly with increasing Mg composition and that even though the material quality measured by EPD and FWHM of x-ray diffraction has been improved dramatically by using a ZnCdSe interfacial layer and Zn-irradiation, the PL linewidths do not change much. In this section, we will present our PL measurements at various temperatures on four $Zn_xCd_yMg_{(1-x-y)}Se$ samples with bandgap ranging from 2.2 eV (ternary) to 3.05 eV in an attempt to enhance our understanding about the carrier recombination processes in this material system. The samples studied in this section were grown without a ZnCdSe interfacial layer and without a Zn-irradiation step, so defect densities were not optimized.

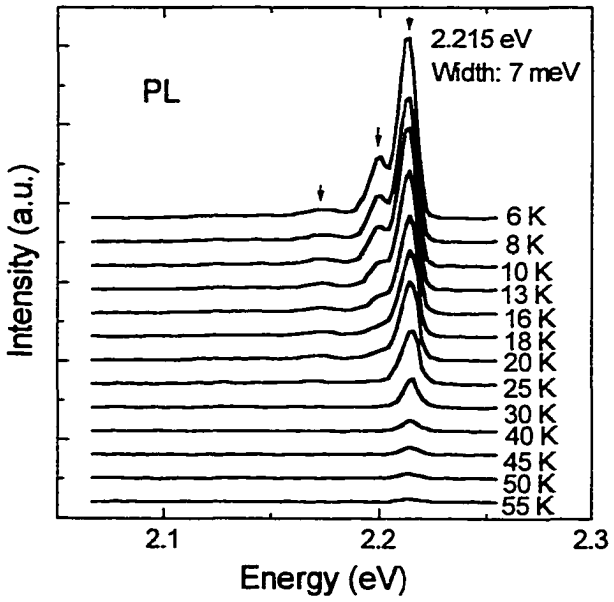

Figure 4-3. The PL spectra at various temperatures for a ZnCdSe layer grown on InP.

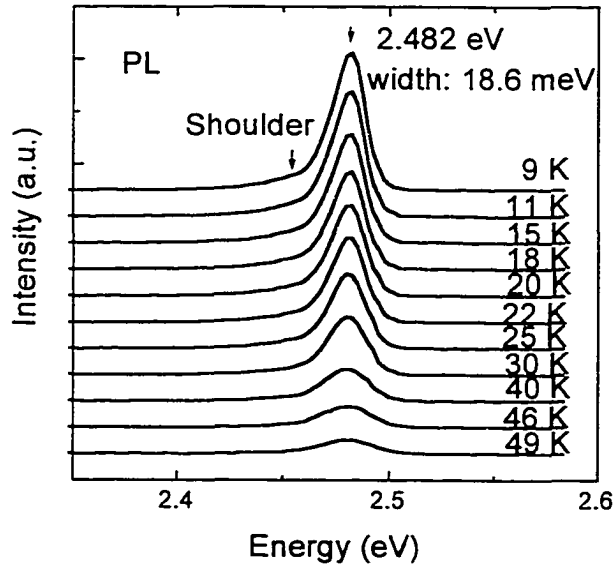

Figure 4-4. The PL spectra at various temperatures for a ZnCdMgSe layer with Mg composition of 0.22.

Figure 4-3 shows the PL spectra of a ZnCdSe layer (sample A) from 6 K to 55 K. At 6 K, three peaks (marked in Fig. 4-3 by arrows) are observed. The dominant peak located at 2.215 eV has a width of ~ 7 meV. When the temperature was increased, the PL intensity decreased very quickly, but the line width did not change very much. On considering these facts, we conclude that this peak is most likely associated with the neutral donor bound exciton.[65] Since in our chamber, Cl has been used as the n-type dopant, we propose it may be the Cl donor-bound exciton. The second emission peak ~ 13 meV below the bound exciton is likely to be an acceptor bound exciton, which usually exists in ZnSe and related compounds.[65] The

very weak peak about 34 meV below the excitonic emission is assumed to be a phonon replica of the dominant peak, since 34 meV is just the LO phonon energy.

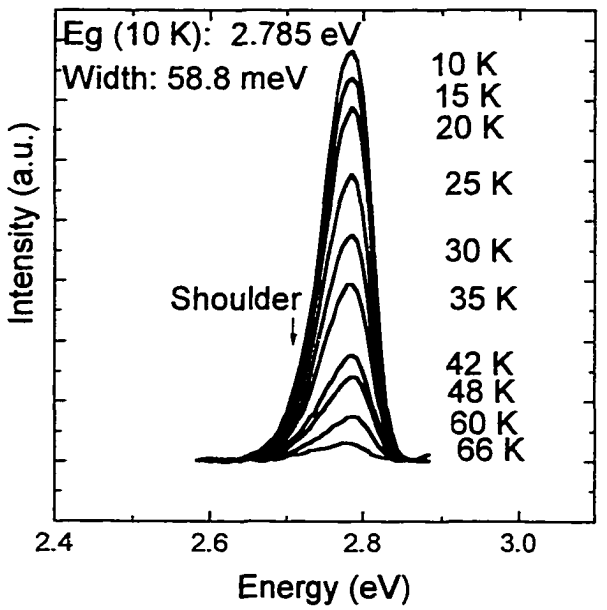

Figure 4-5. The PL spectra at various temperatures for a ZnCdMgSe layer with Mg composition of 0.36.

Figure 4-4 shows the PL spectra at various temperatures for a $Zn_xCd_yMg_{(1-x-y)}Se$ layer (sample B) with a small amount of Mg [(1-x-y)=0.22]. In this case, only one peak was observed. At 9 K, the peak is located at 2.482 eV with width of 18.6 meV and there is a small shoulder at the low energy side. As the temperature increased, the PL intensity decreased and the peak shape became more symmetric but the peak energy did not change significantly.

The PL spectra at various temperatures for a $Zn_xCd_yMg_{(1-x-y)}Se$ layer with Mg composition of 0.36 (sample C) are shown on figure 4-5. At 10 K, the emission peak is located at 2.785 eV with width of 58.8 meV. The shoulder in the low energy side is clear and it could be seen even when the temperature increased to 66 K. As the temperature increased, the dominant

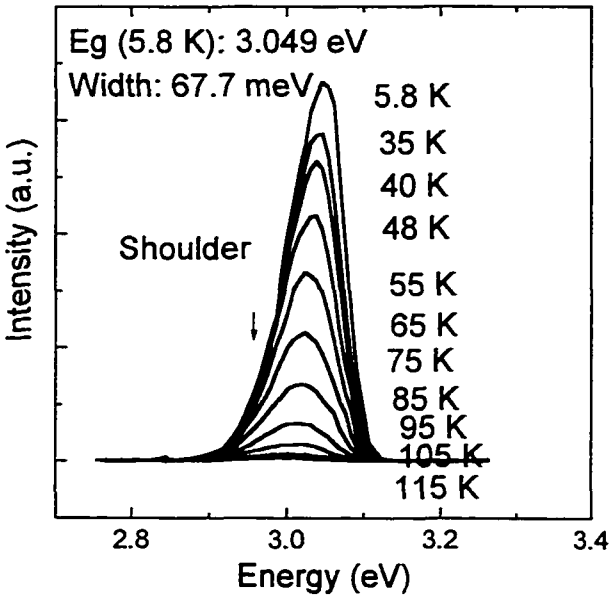

Figure 4-6. The PL spectra at various temperature for a ZnCdMgSe layer with Mg composition of 0.53.

peak intensity decreased, but not as quickly as that of the samples with less Mg, shown in figures 4-3 and 4-4. Figure 4-6 shows the PL spectra at various temperatures for another sample with more Mg [(1-x-y)=0.53] (sample D). At 5.8 K, the emission peak energy is 3.049 eV with a width of 67.7 meV. When the temperature increased, the reduction of the PL intensity is even more slow than in the previous samples. In this case, the shoulder at the low energy side did not disappear at any temperature studied.

In order to understand the behavior of the PL intensity as a function of temperature of $Zn_xCd_yMg_{(1-x-y)}Se$ layers with various Mg content, we have plotted the peak intensity of the PL in a log scale versus 1000/T for the four samples described above. This plot is shown in figure 4-7. The black solid circles are from sample A (ZnCdSe). The intensity decreases very rapidly when 1000/T is ~ 42.5 which corresponds to T of 23.5 K. Below that temperature, the PL intensity remains nearly constant with the increasing

temperature. Above that temperature, the intensity plotted on a log scale, decreases linearly with 1/T. An activation energy was calculated from the slope of this curve to be ~12.0 meV. When some Mg was incorporated in the $Zn_xCd_yMg_{(1-x-y)}Se$ layers, the temperature at which the intensity decreases rapidly with 1/T shifted to higher temperatures. These temperatures are 27.2 K, 33.7 K and 46.5 K, respectively, for samples B, C, and D. The activation energies evaluated from the slopes of the curves are 18.4 meV, 24.6 meV and 26.4 meV for samples B, C, and D, respectively.

To understand this behavior, we perform the following analysis. The donor bound exciton, (D^o, X) complex, can dissociate thermally by two processes involving different activation energies:[66, 67]

$$(D^o, X) \rightarrow D^o + X \qquad (4\text{-}5)$$

where the activation energy (E_a) for this process is the binding energy of the neutral donor-bound exciton, and

$$(D^o, X) \rightarrow D^+ + 2e + h \qquad (4\text{-}6)$$

where the activation energy for this process is the donor binding energy.

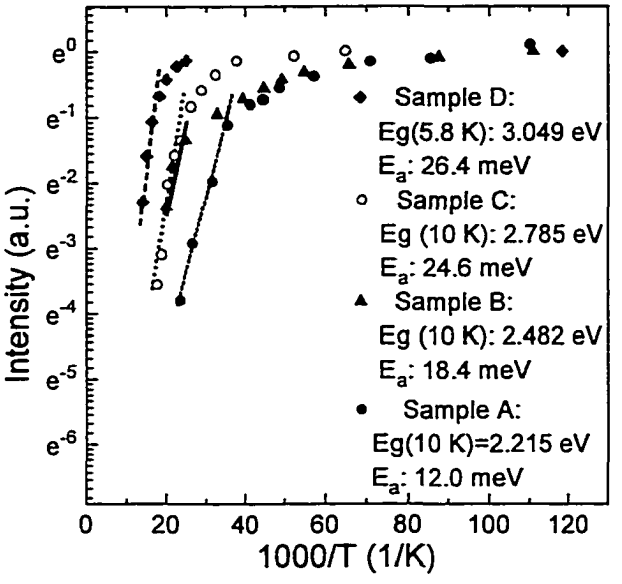

Figure 4-7. The dependence of PL intensity on (1000/T) for the $Zn_xCd_yMg_{1-x-y}Se$ layers with various bandgaps.

For ZnSe, the neutral Cl donor-bound exciton has a binding energy of ~ 5 meV.[68] The Cl donor binding energy is ~ 24 meV.[68] In the case of ZnCdSe and ZnCdMgSe, we expect that the neutral Cl donor-bound exciton should have a similar value of binding energy (~ 5 meV). Since the activation energies we observed are much larger than 5 meV, we expect that process (4-6) is most possibly the one we are observing on our experiment. Thus we propose that these activation energies are indicative of the donor binding energies in these materials. The values of the activation energies obtained are comparable to the value of Cl-donor binding energy in ZnSe (24 meV). Since ZnCdSe has a smaller bandgap (2.2 eV) than ZnSe (2.8 eV), and its conduction band minimum is lower than that of ZnSe, a smaller donor binding energy (12 meV) for ZnCdSe is reasonable. Further studies are needed to confirm this interpretation of our temperature dependent PL intensity measurements.

The dependence of peak energy on temperature for samples D and C is shown in figure 4-8. We fitted the data to a Bose-Einstein type equation:[69, 70]

$$E_{peak}(T)= E_{peak}(0) - 2|a_B|/[e^{\theta/T}-1] \quad (4\text{-}7)$$

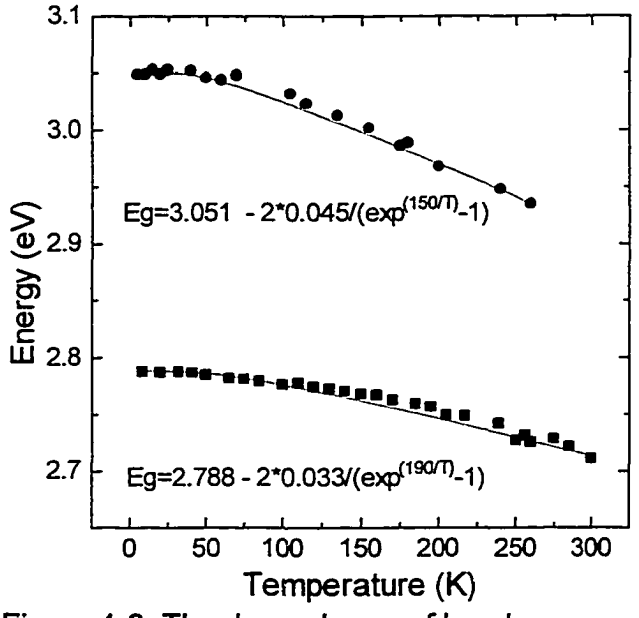

Figure 4-8. The dependence of bandgaps on temperature for ZnCdMgSe layers with two different bandgaps. The solid circle and square are the experimental data while the lines are the fitting data.

where $E_{peak}(0)$ is the bandgap at T=0 K, $|a_B|$ represents the strength of the electron-average phonon interaction and θ corresponds to the average phonon temperature. The fitted curves were plotted by the line in figure 4-8. The two fitted equations we obtained for the data from samples C and D are:

$$Eg=3.051 - 2*0.045/[e^{(150/T)}-1] \quad (4\text{-}8)$$

$$Eg=2.788 - 2*0.033/[e^{(190/T)}-1] \quad (4\text{-}9)$$

Table II lists the values of the parameters obtained for our $Zn_xCd_yMg_{(1-x-y)}Se$ materials and the values for ZnSe[69], $Zn_{0.56}Cd_{0.44}Se$,[69] CdSe,[71] InP and GaAs reported in the literature.[72] It should be noted that the values of a_B and θ for the quaternary materials are very close to the values for CdSe, while the values of the ZnCdSe ternary are similar to that of ZnSe.

Table II. Values of the fit parameters which describe the temperature dependence of the bandgaps of $Zn_xCd_yMg_{(1-x-y)}Se$ obtained in this experiment. For comparison, the relevant parameters for ZnSe, $Zn_{0.56}Cd_{0.44}Se$, CdSe, InP and GaAs are also listed.

Material	$E_{peak}(0)$ (eV)	a_B (meV)	θ (K)
$Zn_{0.37}Cd_{0.27}Mg_{0.36}Se$	2.788	33	190
$Zn_{0.27}Cd_{0.20}Mg_{0.53}Se$	3.051	45	150
$Zn_{0.56}Cd_{0.44}Se$[69]	2.267	62	236
ZnSe[69]	2.800	73	260
CdSe[71]	1.830	36	179
InP	1.423	51	259
GaAs[72]	1.512	57	240

From Fig. 4-3 to 4-6, it is clear that even at temperature below 10 K, the emission peaks for the quaternary layers are still very broad. Thus, we conclude that phonon broadening due to the increased interaction between the phonons and excitons is not the reason for such broad peaks. The linewidths increase linearly with increasing of Mg content, suggesting the broadening is related to Mg content. Nasibov et al,[73] studied the PL and reflection at 2 K of $Zn_xCd_{1-x}Se$ bulk crystals with x varying from 0 to 1. They found that the emission peaks became broad when x was reduced from 1 to 0.7. Between $0.5<x<0.7$, the peaks remained very broad while from 0.5 to 0, the peaks became narrow again. In their work, they concluded that large-scale composition fluctuations[74-76] and 1-dimensional structural disorder in ZnCdSe in the region of the structural phase transition [because of the different structures of ZnSe (Zinc-blend) and CdSe (Wurtzite)] were the main reasons for the PL broadening. In our case, the broadening may be caused by similar reasons since MgSe and CdSe both have hexagonal structures. The total content of Mg and Cd in our $Zn_xCd_yMg_{(1-x-y)}Se$ sample with bandgap of 3 eV has reached ~75%, so the compositions may be near or in the range of the phase transition. Additional measurements to probe this possibility are

planned. For example, we plan to measure Raman spectra to identify the presence of hexagonal and cubic structures in our samples.

In conclusion, we have measured the temperature dependence of the PL spectra for a set of $Zn_xCd_yMg_{(1-x-y)}Se$ samples with Mg fraction (1-x-y) ranging from 0 to 0.53. The intensity of the dominant emission peak decreased when the temperature increased, but the temperature at which the PL intensity decreases rapidly with temperature shifts to higher temperature when the Mg fraction of the quaternary increased. The temperature dependence of bandgaps for two $Zn_xCd_yMg_{(1-x-y)}Se$ samples with 10 K bandgaps of 2.8 and 3.05 eV has been obtained which is a useful property in the design of laser structures. At 10 K, the linewidth of the dominant emission peak was broad for the samples with high Mg fraction. Large scale composition fluctuations and/or the presence of 1-dimensional structural disorder in the region of structural phase transition are proposed as possible reasons for these broad linewidths.

4-3. Capacitance-voltage (C-V) measurements

In the design of laser structures, the band offsets between the various layers and between the epitaxial layer and the substrate are important

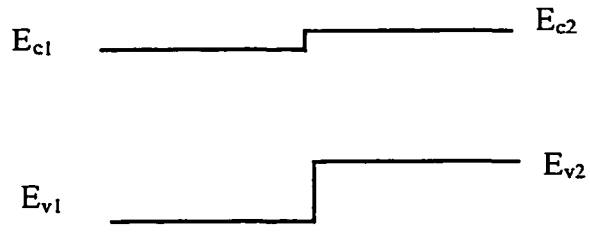

Conduction band offset = $E_{c1} - E_{c2}$

Valence band offset = $E_{v1} - E_{v2}$

Fig. 4-9. The band offset between two semiconductor materials with type II alignment.

parameters. Band offsets show the alignment of the conduction band and valence band edges at the junction between two different materials. As shown in figure 4-9, ΔE_c (E_{c1}-E_{c2}) and ΔE_v (E_{v1}-E_{v2}) are the conduction band offset and valence band offset between the two materials, respectively. The "staggered" alignment shown in Fig. 4-9 is referred to as type II. We have studied the band offset between the ZnCdSe and the InP substrate by using the capacitance-voltage profiling technique. From the plot of the carrier concentration derived from the C-V data versus the depletion depth, we observed quantum carrier confinement near the interface, which gave evidence for a type II alignment of the bands. The conduction band discontinuity at the heterointerface was estimated to be -102 meV.[77] In the following, I will report these results in detail.

Capacitance-voltage (C-V) profiling is a well-established electrical characterization technique to spatially resolve free carrier distribution in

semiconductors.[78] The capacitance of a Schottky junction, a p^+n-, or a n^+p-junction, is measured as a function of the applied reverse bias. For such junctions, the CV concentration, n(z), is inferred from the measured CV profile using the equation

$$n(z) = (C^3/q\varepsilon A^2)(dV/dC), \quad (4\text{-}10)$$

with the CV depth, z, given by

$$z = \varepsilon A/C, \quad (4\text{-}11)$$

where q is the charge of the electron, ε is the dielectric constant, A is the junction area, and C is the diode capacitance, respectively. For a semiconductor at room temperature, the CV concentration is equal to the density of available free carriers. The spatial resolution of the CV concentration can be on order of 20 Å as demonstrated by Schubert et al. for a p-type (Be) δ-doped GaAs sample.[79]

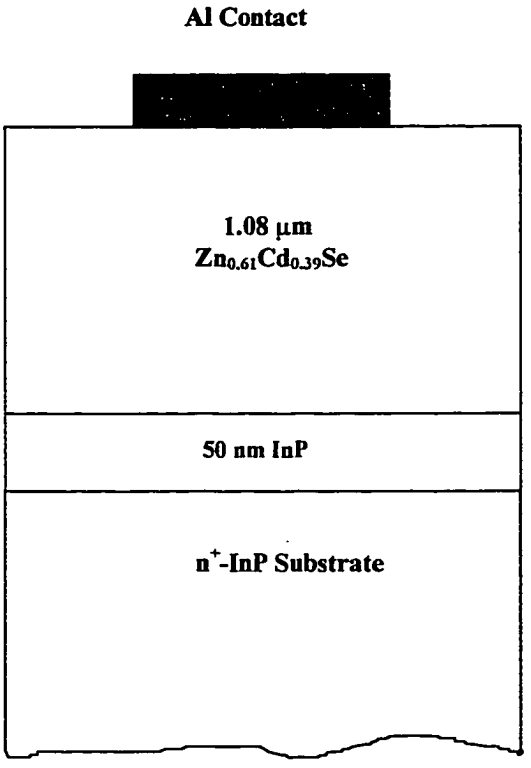

Figure 4-10. The schematic diagram of the devices for C-V measurements.

The schematic diagram of the measured device is displayed in Fig.4-10. The epitaxy structure consists of a 1.08 ± 0.02 μm layer of $Zn_xCd_{1-x}Se$ and 50 nm InP buffer layer. Both layers were intentionally undoped. The Zinc composition x = 0.61 was determined from the single crystal x-ray diffraction. The epitaxial layer was studied by PL. PL and x-ray diffraction data confirmed good crystal quality. Schottky diodes were fabricated by depositing round-shaped Al contacts with a thickness of 3000 Å and a diameter of 2 mm using a high vacuum e-beam evaporator through a mask onto the $Zn_{0.61}Cd_{0.39}Se$ epilayer. Individual diodes are then cleaved from the wafer and bonded to a device holder. C-V measurements were performed in the dark at room temperature using a computerized HP4248A Precision LCR meter.

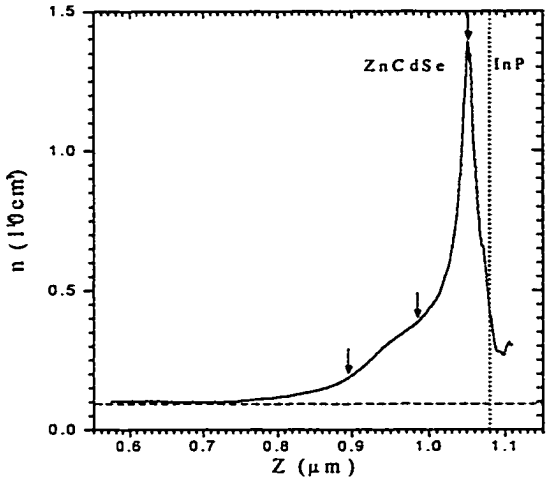

Figure 4-11. Capacitance - Voltage concentration profile of a Al/ZnCdSe/n^+-InP device.

Figure 4-11 shows the CV concentration n(z) obtained from one of our best devices measured at 1 MHz. Several salient features in this CV profile can be described. First, there is an obvious concentration plateau (n_{ZnCdSe}) between 0.57 to 0.75 μm with a value of 1 x 10^{15} cm^{-3}. Second, the CV profile peaks at 1.05 μm and two additional shoulders on the CV profile can be identified at the positions of z = 0.90 and 0.98 μm. They are indicated in the figure by downward arrows. Third, the measured maximum concentration is in the ZnCdSe epitaxial layer side and very close to the ZnCdSe/InP heterointerface. The concentration then sharply decreases and eventually becomes unmeasurable by further increasing the reverse bias due to the increase of leakage current.

What the measured CV concentration profile stands for is to be discussed. Since the ZnCdSe layer was intentionally undoped, it can be donor-rich, acceptor-rich, or compensated dependent on chamber's history and growth conditions. The impurity density should be on the order of the chamber

background density, 10^{14} to10^{15} cm^{-3}. An electron density on order of 10^{15} cm^{-3} was obtained from Hall measurements on several similar epitaxial layers to the one used in this study. To independently determine the level and type of background doping for the epitaxial layer used in this study, we plotted $1/C^2$ versus applied voltage (V_a) and found a positive value of built-in potential V_{bi} = 0.125 V. This polarity of V_{bi} reflects that the electrons originating from donor states in the ZnCdSe layer are depleted when a reverse bias is applied. Hence, the measured CV concentration is the electron density which is equal to the electrically activated donor density away from the ZnCdSe/InP heterointerface. Using the equation of $C_0 = A\ (2V_{bi} / q\varepsilon N_d)^{1/2}$ derived from the *depletion approximation*, where C_0 is the diode capacitance at zero bias, and the measured values of C_0 and V_{bi}, a value of 3.64×10^{14} cm^{-3} for N_d is calculated. This value is consistent with the electron density measured by the Hall effect and CV technique. It indicates (1) the donor-acceptor compensation is negligible and (2) the electron trap density is low in this epitaxial layer.

The most important information contained in the Fig. 4-11 is a clear manifestation of quantum carrier confinement in a quasi-triangular quantum well near the ZnCdSe/InP heterointerface. The observed spatial position-expectation values for the ground state, first excited state, and second excited state are located at z = 1.05, 0.98, and 0.90 μm, respectively. The spatial width of the wave function is about 300 Å for the ground state and gradually increases for higher excited states. The electron density at the position-expectation value is 1.4, 0.4, and 0.2 (10^{16} cm^{-3}) for the ground(n_0), first(n_1), and second (n_2) subband state, respectively. These excess electrons were transferred from n^+ InP when the ZnCdSe layer was deposited on it.

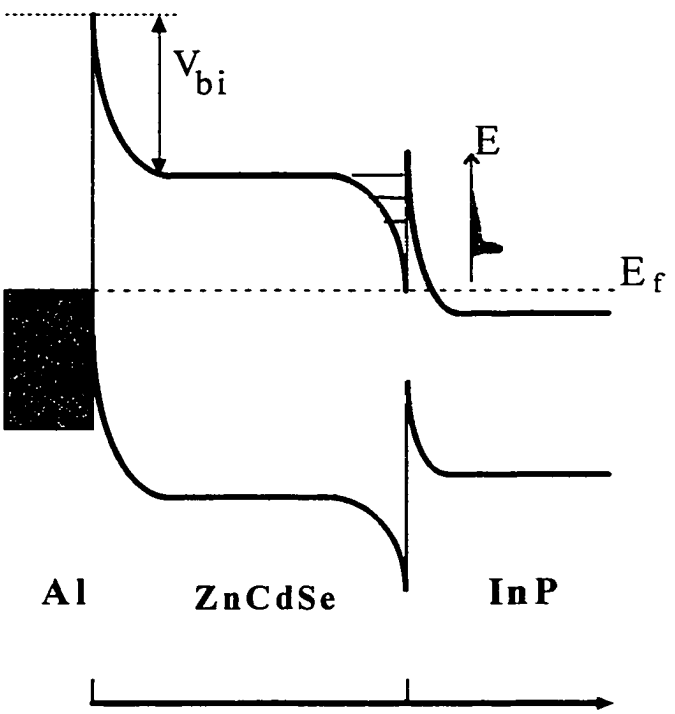

Figure 4-12. Band diagram of ZnCdSe/InP heterostructure illustrating the quantum electron confinement near the heterointerface. There are three subband states observable using the CV profiling techniques

Two main conclusions can be drawn from this observation of quantum carrier confinement. First, since the

electron accumulation is observed in the ZnCdSe side by depleting electrons in the InP side, the band alignment is of type II, that is, the conduction band edge of InP is above that of ZnCdSe, the same is true for the valence band. A schematic diagram for the band line-up near the ZnCdSe/InP heterointerface is shown in Fig. 4-12. From this diagram, a quasi-triangular quantum well (barrier) in the ZnCdSe (InP) side can be seen. The type of band line-up for n-ZnCdSe/n^+-InP is different than that of n-ZnSe/n-GaAs which is of type I.[80] Type II band alignment between n- InP and n-ZnCdSe might be more desirable than for type I band line-up for electron injection in blue-green laser diodes fabricated using ZnCdSe/InP based materials.

Second, the height of the quantum barrier, which is equal to the band offset between ZnCdSe and InP can be estimated using the measured electron density ratios between the two excited state and the ground state. Let the energies of ground state, first, and second excited states be E_0 , E_1, and E_2, respectively. Since the electrons in the conduction band are in thermal equilibrium at a given bias and should obey Fermi-Dirac distribution with a Boltzmann high energy tail as depicted in Fig. 4-12, then the relationship of $n_i \sim \exp(-E_i / K_B T)$ is valid for three spatially displaced two-dimensional subbands. From this relationship, $\Delta E_{10} = E_1 - E_0 = 33$ meV, $\Delta E_{20} = E_2 - E_0 = 51$ meV,

and $\Delta E_{21} = E_2 - E_1 = 18$ meV are calculated. If we assume E_2 is about ΔE_{21} away from the top of the barrier and $E_1 \sim \Delta E_{10}$ usually true for a triangle quantum well,[81] then, the absolute value of ΔE_c between ZnCdSe and InP is estimated to be $\Delta E_{21} + \Delta E_{20} + \Delta E_{10} = 102$ meV. This value for the conduction band offset of n-ZnCdSe and n^+-InP is about 6 times smaller than that for n-ZnSe and n^+-GaAs. More precise determination of ΔE_c requires a self-consistent solution of coupled Poisson's and Schrodinger's equations.

In summary, we have observed the effect of quantum confinement on electrons accumulated near the ZnCdSe/InP heterointerface by the CV profiling technique. Three subband states are identified. Based on the spatial location of the accumulated electrons, the band line-up between ZnCdSe and InP is shown to be of type II. The value for the conduction band offset ΔE_c is estimated to be -102 meV. This study suggests that it is feasible to fabricate blue-green laser diodes based on ZnCdSe/ZnCdMgSe quantum well structures grown on lattice-matched n^+-InP substrates.

CHAPTER 5

Red-Green-Blue (R-G-B) Photo-pumped Lasing from ZnCdMgSe/ZnCdSe QW Laser Structures

Since the over-all purpose of our program is to grow quantum well current injection (pn junction) lasers and emitters, it is useful to understand the properties of the ZnCdSe/ZnCdMgSe quantum wells to investigate the electron and wave confinement of the laser structures for various wavelengths and to optimize the laser structures. In this chapter, I will present my work on this subject.

5-1. Emission of ZnCdSe/ZnCdMgSe quantum wells

We have grown a set of nearly lattice-matched ZnCdSe/ZnCdMgSe quantum well structures, all with the same structure but with different ZnCdSe quantum well thickness. As shown in figure 5-1, the structure[20] consists of a 1 μm thick $Zn_xCd_yMg_{(1-x-y)}Se$ barrier layer, a ZnCdSe quantum well with thickness from 5 to 80 Å, a top 1000 Å $Zn_xCd_yMg_{(1-x-y)}Se$ barrier

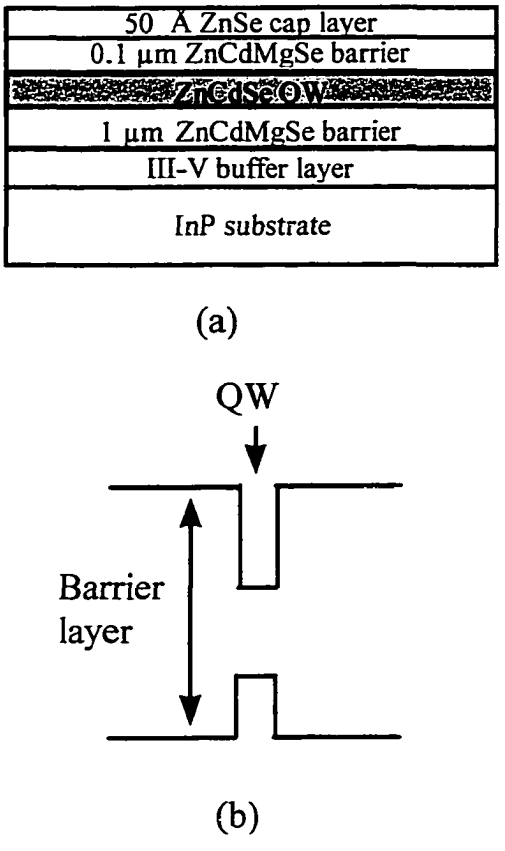

Figure 5-1. The schematic of the quantum well structure.

layer and a 50 Å ZnSe cap layer. The $Zn_xCd_yMg_{(1-x-y)}Se$ layers are well lattice-matched ($\Delta a/a \leq 0.15\%$) to the InP substrates, with a bandgap ranging between 3.0 and 3.1 eV at 10K. For this group of samples, in order to facilitate the growth, the ZnCdSe quantum well is slightly strained, with $\Delta a/a$ of about -0.5% lattice mismatch.

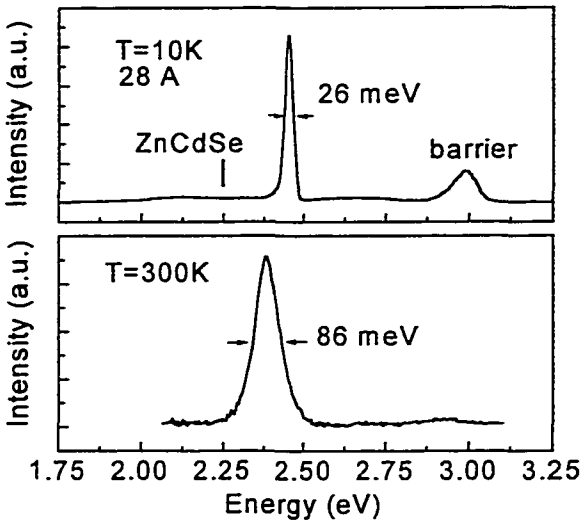

Fig. 5-2. PL spectra for a ZnCdMgSe/ZnCdSe quantum well (28 Å thick) at (a) 10 K and (b) 300 K.

The low temperature PL spectrum of a QW structure is shown in Fig. 5-2(a). The PL signal from the 1 μm thick ZnCdSe layer with the same strain as the quantum well exhibited a bandgap of 2.278 eV and is marked on the spectrum by a bar. The band gap for the $Zn_xCd_yMg_{(1-x-y)}Se$ barrier layer was detected at 2.980 eV. The emission from this nominally 28 Å thick QW was detected at 2.450 eV indicating a quantum shift of 172 meV. An emission linewidth of 26 meV suggests that the interfaces at the QW are smooth and abrupt. Room temperature PL for the same sample is shown in Fig. 5-2(b). Strong room temperature emission supports the high quality of the sample.

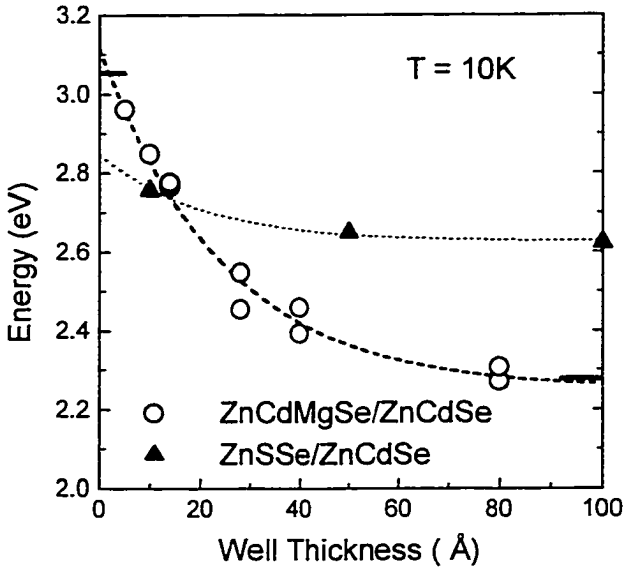

Fig. 5-3. Emission range of ZnCdMgSe/ ZnCdSe quantum well structures on InP.

The emission energy estimated from the 10K PL of the quantum well samples as a function of quantum well thickness is shown in figure 5-3. Each data point represents a different growth run. The bar on the left axis of the plot indicates the band gap position of the quaternary barrier layers. The band gap position of a thick ZnCdSe with the composition used in the quantum well is indicated by another bar on the right axis of the plot. A dashed line connecting the data (open circles) is drawn to highlight the range over which the emission energy varies. Similar data[82] from strained-layer ZnCdSe/ZnSSe QWs grown on GaAs substrates are also shown. The comparison shows that there is a much larger tunability range of the QW emission wavelength for our new materials. By varying the well thickness, the emission wavelength of our structures can be varied from 2.28 to 2.95 eV, measured at 10K, this corresponds to 2.2 to 2.85 eV at room temperature, covering nearly all the visible range. Another attractive feature of the new

QW laser is the large confinement energy of about 250 meV even in the blue range (~2.76 eV). This large carrier confinement energy is a desirable feature for good laser performance.

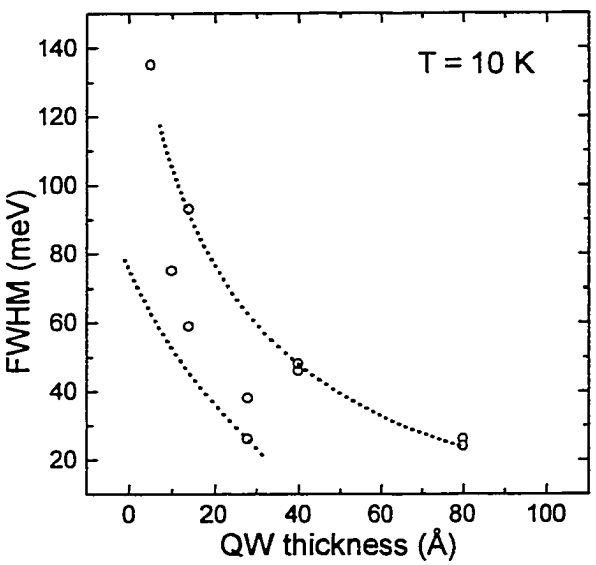

Figure 5-4. Full width at half maximum of QW emission lines as a function of QW thickness.

From the width of the PL emission lines we can get an assessment of the quality of our QW structures. Figure 5-4 shows a plot of the FWHM of the PL emission lines measured at 10K as a function of QW thicknesses for the same set of samples in Fig. 5-3. As can be seen, the linewidths vary from one sample to another especially for QW less than 40 Å thick, suggesting differences in the QW interface roughness. PL measurements in several spots within a sample do not exhibit variations in the PL linewidths, suggesting that the roughness is uniform within a sample. In spite of the fluctuations, the data in Fig. 5-4 indicate that for some of our structures narrow PL lines and, thus, smooth interfaces were achieved.

In conclusion, we have grown nearly lattice-matched ZnCdSe/ZnCdMgSe QW structures on InP substrates. Low temperature PL emission range from 2.960 to 2.307 eV at 10 K was obtained by varying the QW thickness between 5 and 80 Å. High luminescence efficiency at 10 K and at room temperature was observed from these samples. Sharp luminescence lines, consistent with good quality interfaces were obtained in many samples. These QW structures could serve as the active region of entirely lattice-matched laser structures which are expected to be less prone to degradation than the current reported ZnSe based laser diodes.

5-2. Optically pumped visible lasers

Based on the QW studies described above, we have demonstrated[21, 22] the optically pumped operation at room temperature of a set of new ZnCdSe/ZnCdMgSe separate-confinement single-QW lasers grown lattice-matched to InP substrates that emit in the range covering the red, green and blue regions. The schematic of the structure used for the optically pumped lasers is shown in Figure 5-5. Shown on the top is the layer structure while the bottom shows the bandgap profile. As shown in figure 5-5, the structure consisted of 1 μm thick $Zn_xCd_yMg_{(1-x-y)}Se$ barrier layers with a nominal

bandgap of 3.0 eV, 2000 Å thick $Zn_xCd_yMg_{(1-x-y)}Se$ waveguiding layers with a nominal bandgap of 2.7 eV, the ZnCdSe active layer and a 100 Å thick ZnSe cap layer. In the blue-yellow range, the ZnCdSe layer was grown lattice-matched to the InP substrate, the emission wavelength was varied by changing the active layer thickness. In the red range, the composition of ZnCdSe active layer was adjusted. Typical strain by adding excess Cd in the ZnCdSe layer in order to get emission at ~610 nm is ~ 1.2% to the InP substrates, which is similar to the strain in the active layer in ZnCdSe/ZnMgSSe based laser structures.[83]

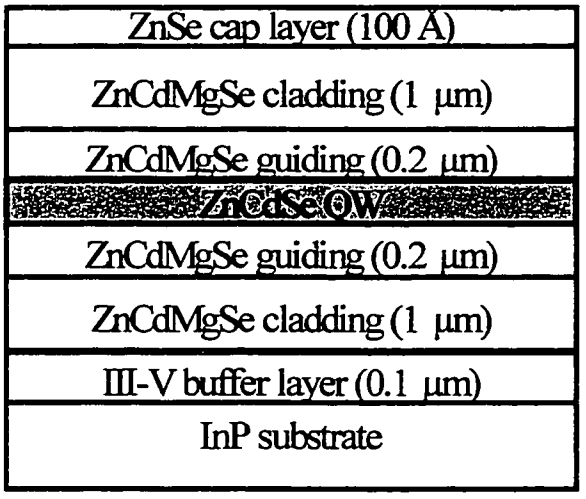

(a)

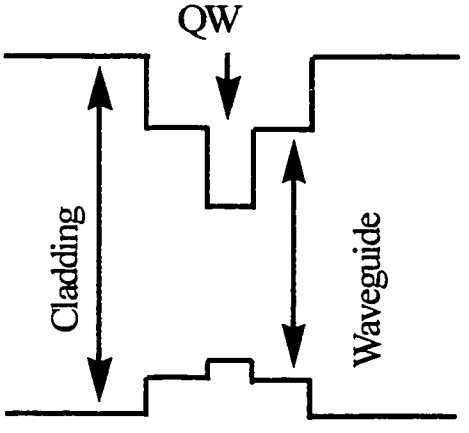

(b)

Figure 5-5. The schematic of the structure for optical pumped lasers. (a) shows the layer structure while (b) shows the bandgap profile.

In order to make sure the cladding, waveguiding and active layers have the desired bandgap or emission energy, we need to find a way to measure the emission energy from all the layers in the laser structure. PL is one way to measure the emission energy, but because our excitation energy is well above the barrier bandgap, PL can only give the information near the surface (~4000 Å). Since the laser structures have a very thick cladding layer (~ 1 μm) on the top, the PL of our laser structures usually only give us the emission peak of the top cladding layer.

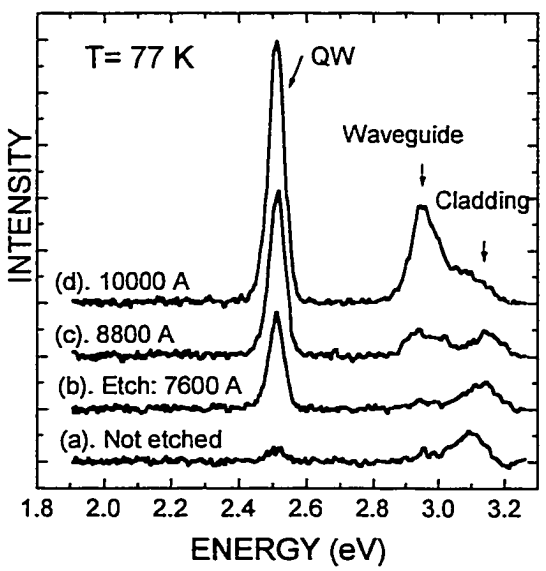

Fig. 5-6. PL spectra at different stages of etching for a laser structure.

We found that bromine and methanol solution in a suitable concentration can etch the $Zn_xCd_yMg_{(1-x-y)}Se$ layer very smoothly and that the etch rate could be controlled. We used a bromine and methanol solution to etch a few pieces of the same laser structure for different etching times, then measured the PL on the etched pieces. The concentration of the etching solution used was ~ 6 drops bromine/100 ml methanol which gave an etching rate of ~ 40 Å/s. The etching

solution was kept in an ice-bath at 0°C to better control the etch rate. The etching time was selected so that we could observe the process of eventually etching away of top cladding, waveguiding and QW layers from the PL measurements. Figure 5-6 shows the 77K PL spectra of the laser structure at different stages of the etching. Curve (a) is from the unetched piece. The main emission peak is at ~3.1 eV, from the top cladding layer. The emission peaks from the waveguide and QW layers are very weak and hard to observe. Curve (b) is from the piece with ~7600 Å etched away from the top layer. In this case, the QW emission becomes the strongest peak. Continuing the etching [curve (c), ~8800 Å etched away], the emission from the QW becomes even stronger. The emission peak from the waveguide layer is almost as strong as that from the cladding layer. After etching away ~ 10000 Å, which means the top cladding layer is totally removed, the PL spectrum shows very strong emission peaks from the QW and waveguide layers. The emission peak from the cladding layer almost disappeared. Thus, by using the etching combined with PL measurements, we can reveal the details of our laser structures.

We have grown several laser structures for optical pumping. The samples were thinned to about 100 μm thick and cleaved into 1-mm-wide bars for photo-pumping. The experimental setup for photo-pumping was similar to that described in Ref. 84. A frequency tripled Nd: YAG laser

pumped dye laser was used as the pump source. The pulse width and repetition rate of dye laser output were 7 ns and 20 Hz, respectively. To ensure the largest concentration of photo-generated carriers in the vicinity of QW, the wavelength of the dye laser was tuned to the photon energy near the bandgap of the waveguide layer at room temperature. The pump beam was focused onto the surface of the wafer to create a stripe geometry excitation region along the (110) direction. A variable attenuator was used to control the pumping intensity. The edge emission of the laser bar was collected by a microscope objective and focused into an optical multichannel analyzer to analyze the spectral characteristics. A boxcar integrator was used to measure the pumping power and output light power.

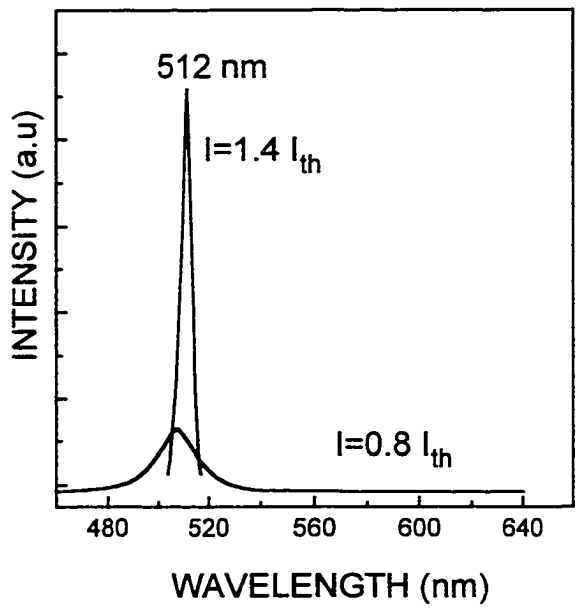

Fig. 5-7. The spectra of the edge emission below and above the lasing threshold.

Initially a laser structure was grown and its lasing was investigated in detail. The spectra of the edge emission below and above the lasing threshold are shown in figure 5-7. We observed the clear lasing behavior: the peak became much narrower when the pumping intensity is higher than the threshold. The lasing emission is red-shifted relative to the spontaneous emission, which is expected because the gain reaches maximum in the red-side of the spontaneous emission peak. The power input-output plot shown in figure 5-8 exhibited a clear turn-on of the power output above the threshold. The relationship between the output intensity and the pumping intensity exhibits a typical superlinear relation below the lasing threshold and a linear relation above the threshold. The threshold occurs at a pumping power density of 160 kw/cm^{-2}. From the temperature dependence of the threshold power density, we calculated the characteristic temperature of the laser: T_o =

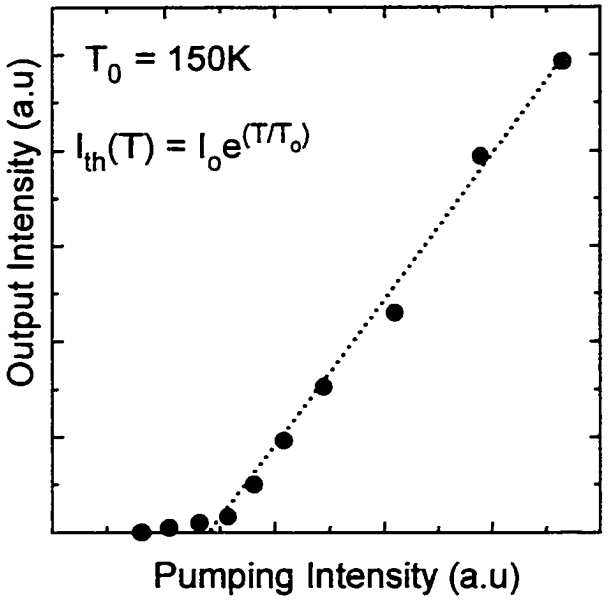

Fig. 5-8. The output intensity vs the pumping intensity.

150K, which is comparable to previously reported values for ZnCdSe/ZnMgSSe lasers.[85, 86]

Table I shows the parameters of three additional laser structures grown to investigate the full emission range. The QW emission wavelengths were obtained from the 77K PL spectra. The QW mismatch given in Table I was estimated from x-ray measurements of a 1 μm thick reference layer grown under the same growth condition as the QW. The QW thickness was calculated from the growth time of the QW and the growth rate of the reference sample. By using lattice-matched ZnCdSe layers and changing the QW thickness, the emission range was varied from green to near blue (samples A and B). By using a mismatched (pseudomorphic) ZnCdSe layer as the QW, the emission of the QW was in the red (sample C).

Table I. Parameters of three laser structures with emission from blue to red

Sample	QW thickness (nm)	QW Mismatch (%)	QW Emission wavelength at 77K (nm)
A	2.8	0	473
B	4.0	0	516
C	12.0	1.2	590

Figure 5-9 shows the intensity of optically pumped lasing versus the emission wavelength when the pumping intensity is above the threshold. The pumping wavelength is ~ 460 nm. The laser emission wavelengths obtained at room temperature are 497, 540, and 604 nm for samples A, B and C, respectively, covering the range from near blue to red. The stimulated emission peaks have a typical linewidth of about 5nm, about 5 times less than the emission peaks before the lasing. Thus, stimulated emission in the blue, green and red has been obtained from these three nearly identical ZnCdSe/ZnCdMgSe structures grown on InP substrates. This result demonstrates the potential for fabricating integrated full color display elements from these materials. To date, no other single set of semiconductor

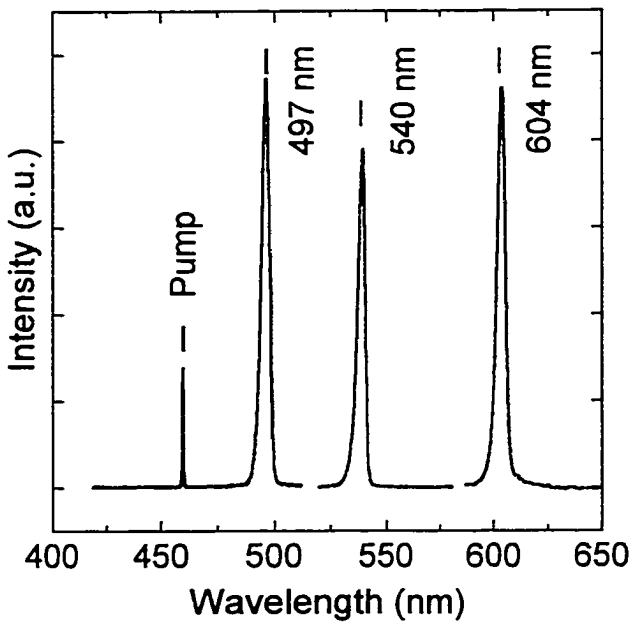

Fig. 5-9. Lasing emission from three ZnCdSe/ ZnCdMgSe laser structures with emission wavelength from 497 nm to 604 nm, covering the range from blue to red.

materials has been demonstrated to produce light emitters operating throughout the entire visible range.

As a conclusion, we have obtained room temperature photo-pumped lasing from three ZnCdMgSe/ZnCdSe based laser structures grown on InP. The structures are nearly identical, except for variations in the thickness and/or composition of the QW layer. Lasing emission in the red, green and blue (R-G-B) region was obtained. Our results demonstrate the potential for these materials as integrated full color display devices.

5-3. Improved optically pumped lasers

We have observed optically pumped lasing in almost the entirely visible range from near blue to red. So far, the emission range is between 497

nm to 604 nm. In this section, I will report the results to push the range further to blue and red. In order to extend the range to blue (for example, 460 nm), the QW thickness has been made very narrow. The wave confinement factor and the carrier confinement energy will be small. Thus, we need to increase the band gaps of the cladding and waveguide layers and to optimize the band structure of the laser. We also need to push the emission range further to the red (~ 630 nm, where He-Ne lasers are commonly used). Additional Cd in the QW will achieve this, but this will increase the lattice-mismatch and reduce the critical thickness of the active layer. We will explore the limits of our structure in this region.

The early laser structures we have reported above were grown without the Zn-irradiation and ZnCdSe buffer layer, so the material quality was not optimum. Since the growth of these initial structures, the quality of $Zn_xCd_yMg_{(1-x-y)}Se$ has been improved dramatically by using Zn-irradiation and incorporating the initial low-temperature grown ZnCdSe buffer layer. The defect density for $Zn_xCd_yMg_{(1-x-y)}Se$ with bandgap of 3.0 eV has been reduced from 10^9 cm^{-2} to mid-10^4 cm^{-2}. The range of Mg composition, for which the ZnCdMgSe layers have the same quality as ZnCdSe layers, has been greatly extended. To complete our study, we have grown the laser structures for optically pumped lasers by using these techniques. Very high bandgap (~ 3.15

eV) $Zn_xCd_yMg_{(1-x-y)}Se$ layers were used as the cladding layers in the structures for blue lasers.

The improved structure is the same as in figure 5-5. The difference is that before the growth of II-VI, the substrate with the III-V buffer layer was exposed to the Zn beam for 15 seconds at 170°C, then a 1 min ZnCdSe interfacial layer was grown (see Section 3-3-2E). After that, growth was interrupted for ~ 6 minutes to increase the growth temperature to 270°C and start the growth of the $Zn_xCd_yMg_{(1-x-y)}Se$ cladding layer. In this study, the thickness of waveguide layer was reduced to 1000 Å. The thickness of the cladding layer was also reduced to 3000 Å in order to ensure that there is no relaxation of the unintentional mismatch. Since it is very hard to grow the exactly lattice-matched materials ($\Delta a/a$ is controlled to ≤ 0.2 %).

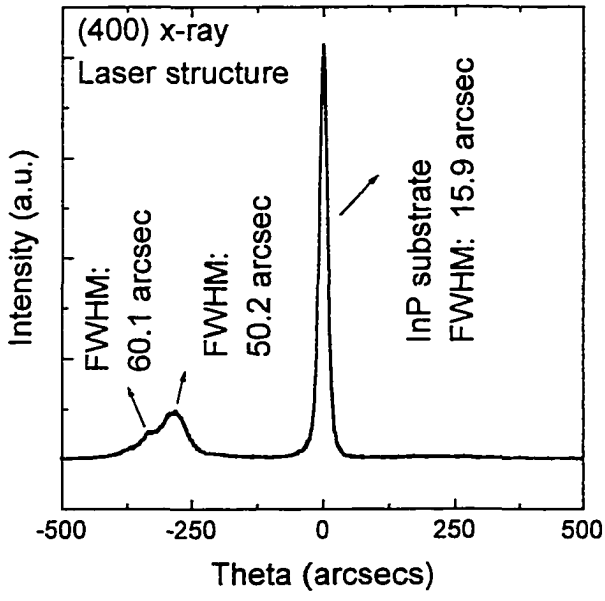

Figure 5-10. Double crystal x-ray rocking curve in the (400) reflection for a laser structure.

Figure 5-10 shows the (004) double x-ray rocking curve of a laser structure with a QW thickness of 80 Å. Besides the dominant peak assigned to the InP substrate, there are two other peaks which are very close. From results obtained from a 1 μm thick InGaAs reference sample, we expect that the InGaAs buffer layer is exactly matched to the InP substrate. So these two peaks are assigned to II-VI layers, most possibly from the cladding and waveguide layers. These two peaks are strong and narrow, with FWHM of 60.1 and 50.2 arcsec, suggesting very good material quality. EPD for this sample shown in Fig. 5-11 was measured in ~4×10^4 cm^{-2} range. We have also measured the {511}a and b double x-ray rocking curves of this sample. From the peak separation, we have calculated the perpendicular and parallel lattice mismatch, which are 0.201% and -0.03%, respectively. From the (004) x-ray curve, calculated perpendicular lattice-match is 0.221%, consistent with the results from the {511} measurements. Thus, the parallel lattice mismatch is very small, almost 0, suggesting that the entire structure is pseudomorphic.

Figure 5-12 shows 77 K PL spectra of three laser structures grown under these conditions. As the thicknesses of cladding and waveguide layers have been reduced, we can observe the PL emission peaks from cladding, waveguide and QW layers without etching. Fig. 5-12(a) shows the PL for a laser structure with QW emission at 2.012 eV, in the red range. The QW

thickness is ~ 60 Å. The 1 μm thick reference ZnCdSe layer with the same growth condition as the QW layer has a bandedge emission at 1.968 eV. We used large lattice-mismatch to reduce the QW size to avoid the lattice-relaxation while still keeping the emission in the red range. The emission peak from the QW is very narrow (~12.6 meV), suggesting good layer quality (The EPD of this sample is ~ 1×10^6 cm^{-2}). Fig. 5-12(b) shows the PL for a laser structure with QW emission at 2.195 eV, in the yellow range. The QW thickness is ~ 80 Å. In these two structures [(a) and (b)], the bandgap for cladding layer was set at ~3.0 eV while for waveguide layer it was set at ~ 2.8 eV. The difference between them is ~200 meV. The 77K PL for the structure emitting in the blue range is shown in Fig. 5-12(c). In order to increase the confinement energy, the bandgap of cladding and waveguide layers was increased by ~ 0.15 eV, to 3.13 and 2.93 eV, respectively. The EPD of this sample is ~ 8×10^5 cm^{-2}, suggesting good quality. The QW thickness is only ~ 20 Å in this sample. The QW emission is at 2.739 eV, in the blue range. The width of the peak is 56.8 meV. There is a second smaller emission peak at 2.618 eV. This may be due to the quantum well thickness fluctuation or the interface roughness. Since the thickness of the QW in this sample is only ~20 Å, the effect of quantum well thickness fluctuations or interface roughness will be relatively large and may cause a second emission.

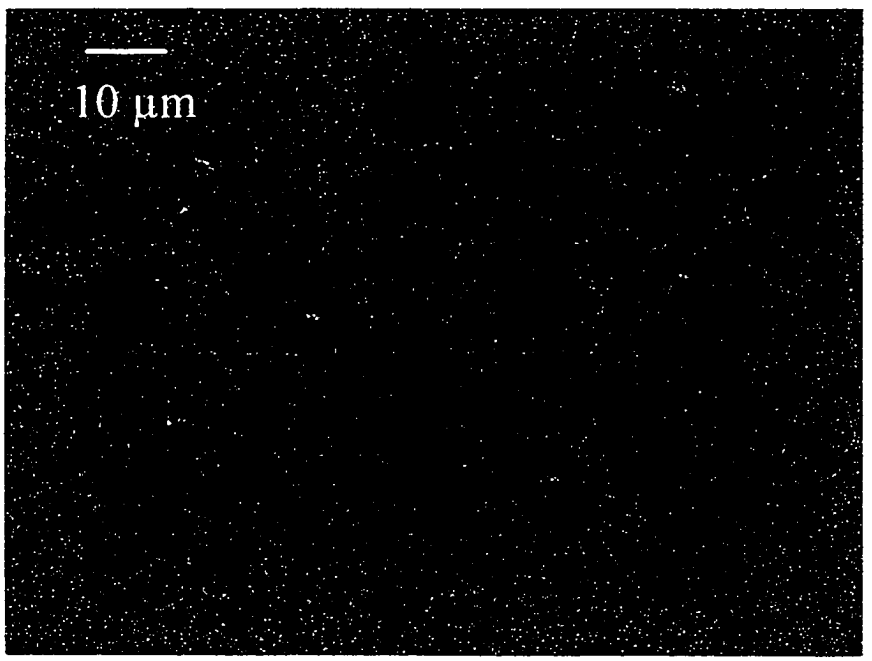

Figure 5-11. The Nomarski micrograph of the etched surface of ZnCdSe/ZnCdMgSe laser structure. The EPD is $\sim 4\times10^{4}$ cm^{-2}.

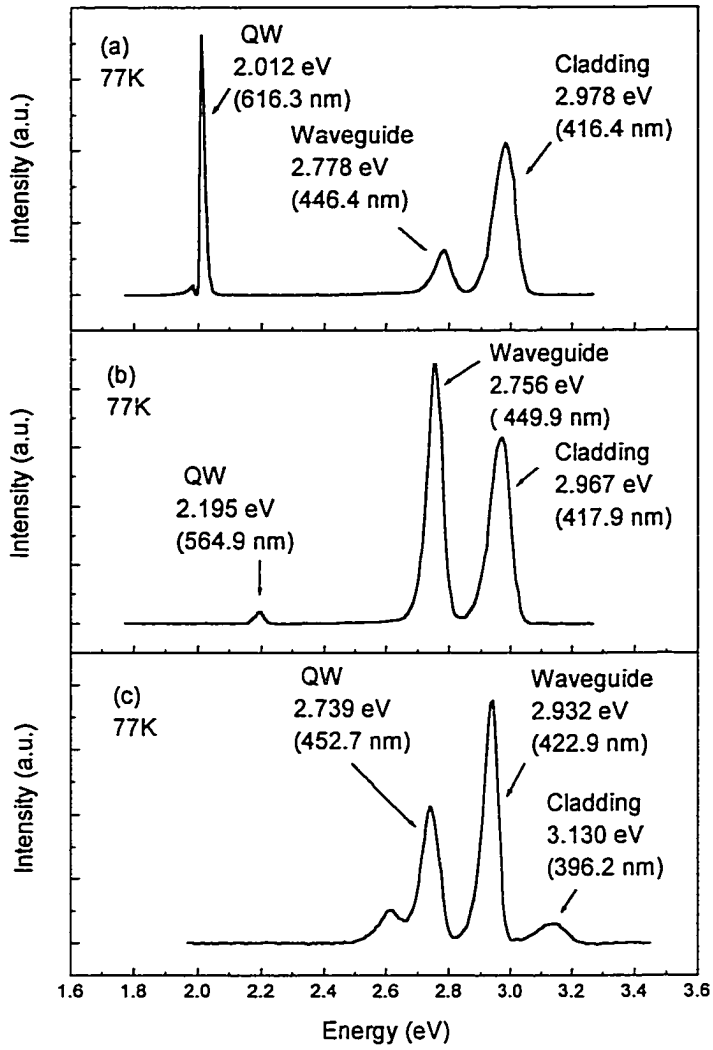

Figure 5-12. PL spectra at 77 K for three laser structures with QW emission from red to blue.

We have obtained laser emission from all these structures. Figure 5-13 shows the optically pumped laser emission spectra from a laser with structure

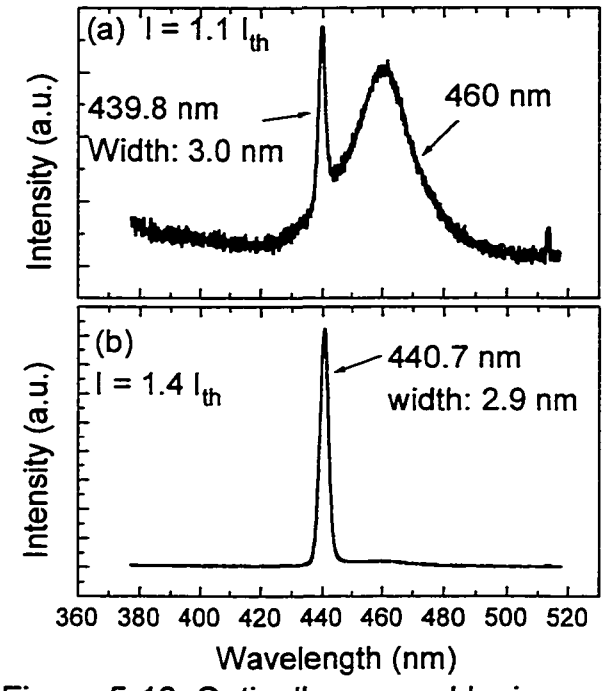

Figure 5-13. Optically pumped lasing spectra from one of the laser structures with emission in the blue range.

C. Fig. 5-13(a) shows the spectrum when the pump intensity is about 1.1 times of the threshold intensity. Both the stimulated and spontaneous emission peaks can be observed. An interesting behavior observed is that the stimulated emission is blue-shifted relative to the spontaneous emission, which is different from the behavior of the laser structures we have described in section 5-2, where the stimulated emission is, as expected, red-shifted. Further studies are on going to understand this behavior. The stimulated emission wavelength for this structure is 440 nm. Fig. 5-13(b) shows the spectrum when the pump intensity is about 1.4 times of the threshold intensity. The width of the stimulated emission peak is ~ 3 nm, narrower than the ~ 5 nm observed in the laser structures reported in section 5-2.

In summary, we have grown laser structures with improved material quality as demonstrated by the reduced defect densities and stronger,

narrower DCXRC peaks. We have extended the material properties further into the blue and red region of the spectrum. Laser emission from these structures has been obtained. The width of the laser emission is narrow, consistent with the quality improvements in these structures. Unexpected blue shifts in the stimulated emission are under further investigations.

5-4. Degradation study of ZnCdSe/ZnCdMgSe QW structures

Since the first introduction of a ZnSe based blue-green diode by Haase et al. in 1991,[87] the life time in cw mode at room temperature has reached 100 hours.[4] Device degradation, by the formation of nonradiative centers during current injection, is the main limit to the lifetime. It is well established that the degradation originates at pre-existing defects (mainly stacking faults) and propagates by the formation on <100> dark line defects (DLDs) in the active layer.[88-91] Considerable research has been directed toward the microstructural origins of <100> DLDs that form during degradation of II-VI blue-green light emitters. For example, Guha et al[88] suggested that DLDs consist of point defects or small point defect complexes, based on their TEM study. The presence of ~ 1.5% compressive strain in the ZnCdSe active layer

is suspected to be a contributing factor. Since our yellow-blue QW and laser structures are totally lattice-matched, it is of interest to study the degradation behavior in our ZnCdSe/ZnCdMgSe structures.

In this work, we have used strong electron beam irradiation to degrade the ZnCdSe/ZnCdMgSe QW structures and used cathodoluminescence (CL) to observe the appearance of DLDs.[92] The CL measurements employed a JEOL JSM-6400 SEM equipped with parabolic mirror light collecting optics and computer controlled SPEX 340S spectrometer with a GaAs photomultiplier tube (PMT) detector. The output of the PMT can be used in raster scan mode to form images. In this study,[93] the luminescence from the QW was used for the imaging. The samples used in this study were grown with InGaAs buffer layer and ZnCdSe interfacial layer. The QW structure consists of a 3000 Å $Zn_xCd_yMg_{(1-x-y)}Se$ barrier layer, a ZnCdSe quantum well, then a top 1000 Å $Zn_xCd_yMg_{(1-x-y)}Se$ barrier layer and a 50 Å ZnCdSe cap layer. The barrier layers are well lattice-matched to the InP substrates, with a bandgap of ~3.0 eV at 77K.

In order to illustrate the appearance of DLDs, figure 5-15 shows the monochromatic CL micrograph taken at room temperature for a ZnSe based laser structure grown at Philips Laboratories after degradation with an electron beam. The data are from L. L. Chao et al.[92] The luminescence from

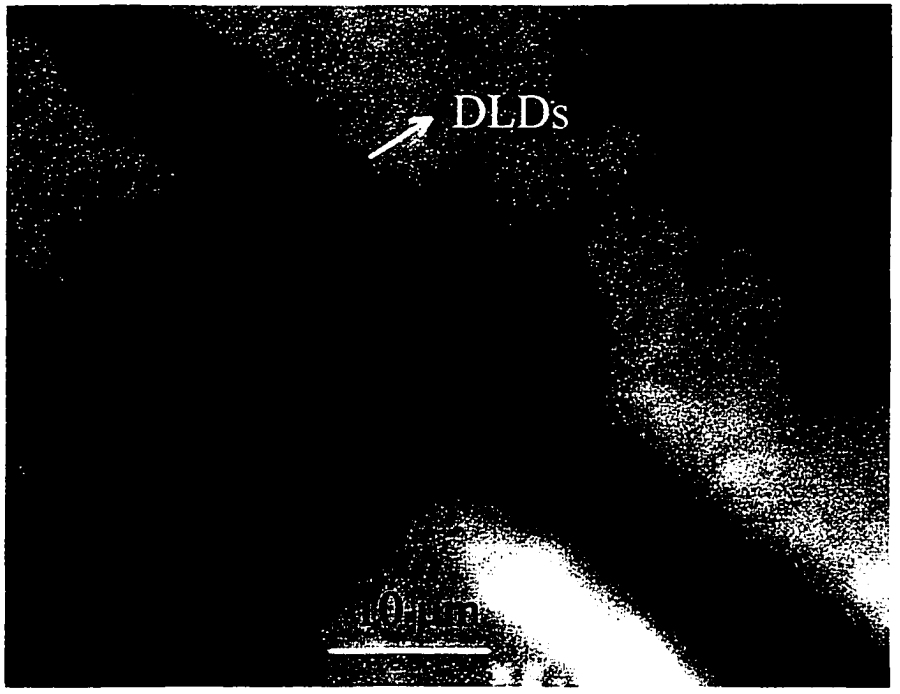

Figure 5-14. The monochromatic CL micrograph taken at room temperature for a ZnSe based laser structure grown at Philips Lab. after degradation. The figure is from L. L. Chao.[92]

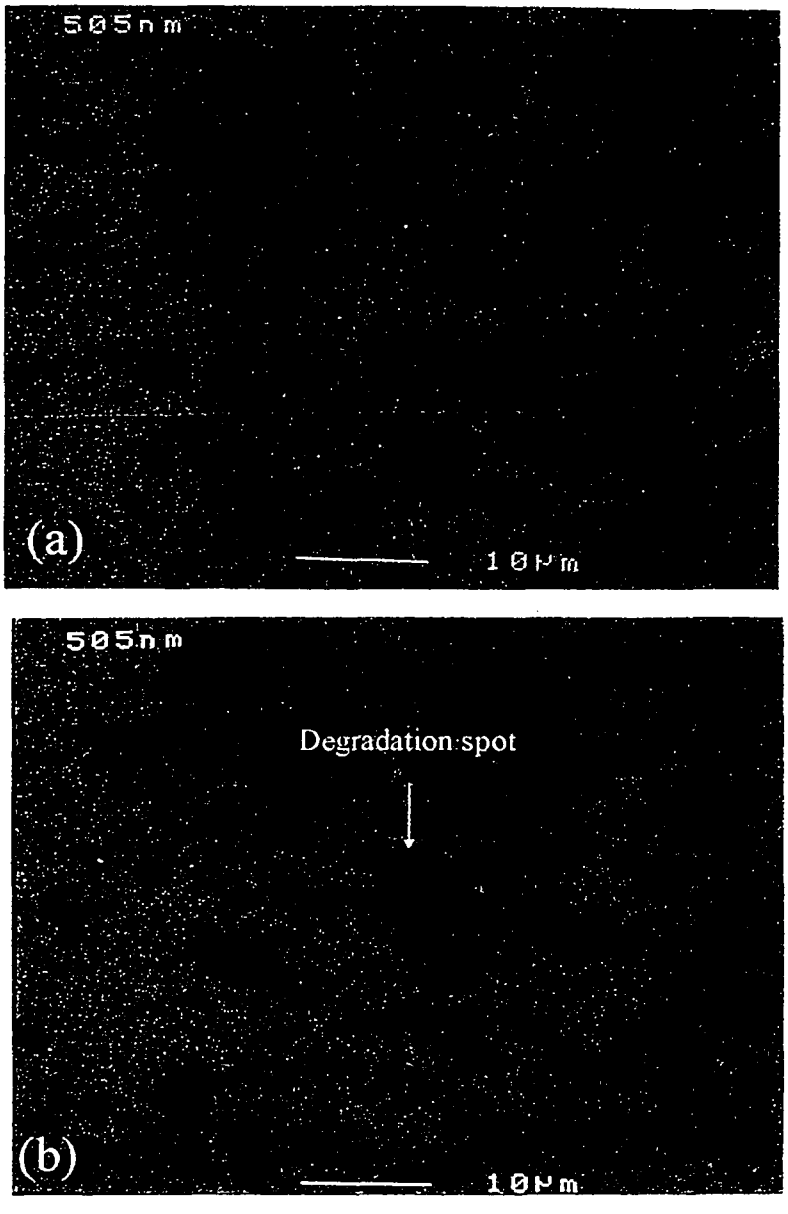

Figure 5-15. The monochromatic CL micrograph taken at room temperature for a lattice-matched ZnCdSe/ZnCdMgSe QW structure before the degradation (a) and after degradation (b).

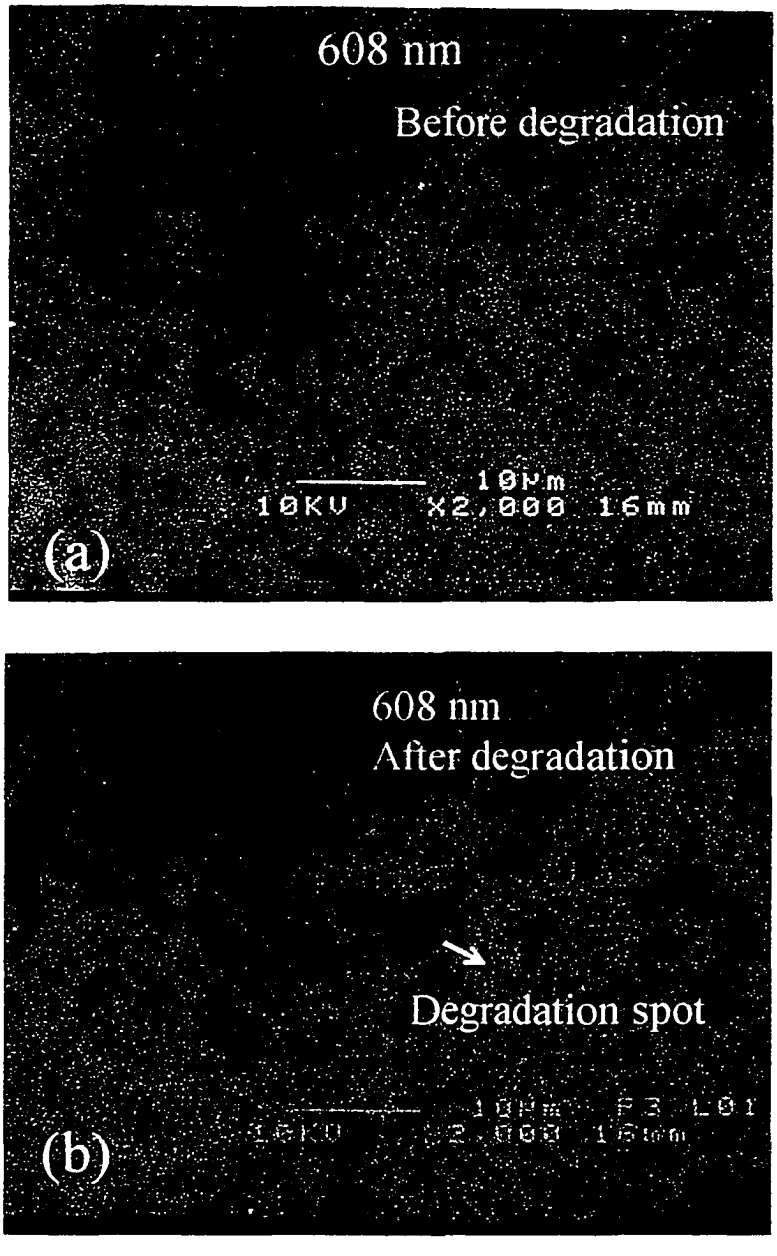

Figure 5-16. The monochromatic CL micrograph taken at room temperature for a lattice-matched ZnCdSe/ZnCdMgSe QW structure before the degradation (a) and after degradation (b). The ZnCdSe QW layer has ~ 1.5 % strain in this sample.

the QW was at 521 nm. This image clearly shows pairs of DLDs originating from the laser stripe.

Figure 5-16(a) shows the monochromatic CL micrograph taken at room temperature for a ZnCdSe/ZnCdMgSe QW structure before degradation. The 20 Å thick ZnCdSe QW is lattice-matched to the InP substrate. The luminescence from the QW was at 505 nm. In this image, we observed dark points (DPs). The density of DPs is in the 10^6 cm^{-2} range, consistent with the EPD results of this sample. The monochromatic CL micrograph for the same sample after degradation is shown in figure 5-16(b). The scale is the same as in (a). The large dark spot is the area that was degraded by the e-beam. It is clear that even though the area has been damaged, there are no DLDs observed. In order to investigate whether strain played a role in this degradation behavior, we have grown a ZnCdSe/ZnCdMgSe QW structure with ~ 1.5% compressive strain in the active layer. This strain is comparable to that in the sample of Fig. 5-14. The thickness of the QW was set to ~ 40 Å to make sure the layer was not relaxed. Figure 5-17(a) shows the monochromatic CL micrograph of this structure before degradation. The luminescence from the QW was at 608 nm. DPs with density in the 10^7 cm^{-2} range were observed (EPD measurements for this sample gave defect density of 8×10^6 cm^{-2}). Figure 5-17(b) shows the

monochromatic CL micrograph for this QW structure after degradation. The degraded spot was clear. However, there were no DLDs observed even at these highly strained QWs. Thus, the absence of DLDs in our $Zn_xCd_yMg_{(1-x-y)}Se$ system appears not to be related to the absence of strain in the structures. Further investigations are been pursued to understand the degradation behavior of our materials.

In a summary, we have made preliminary studies of the degradation behavior of ZnCdSe/ZnCdMgSe QW structures with and without strain in the QW layer. No dark line defects (DLDs) were observed during the degradation for both cases. This is in contrast to the behavior of ZnSe/GaAs based laser structures reported in the literature. No relationship between strain and DLDs was observed for our structures. Without the generation of DLDs during degradation, lasers made from ZnCdSe/ZnCdMgSe structures on InP may be less prone to degradation than the currently reported ZnSe/GaAs laser structures.

CHAPTER 6

New applications for $Zn_xCd_yMg_{(1-x-y)}Se$ /InP system

We have reported the results of C-V measurements in section 4-3. In this chapter, we will report the results of current voltage (I-V) measurements on the same structure from 77 K to room temperature. A strong negative differential resistance (NDR) under forward bias was observed for temperature higher than 145 K.[94] The peak-to-valley current ratio at room temperature was measured to be 30. In the reverse bias region the device behaves as a Schottky diode. NDR devices based on resonant tunneling in double-barrier structures have attracted much interest since the pioneering work of Tsu, Esaki, and Chang.[95] This new observation may render II-VI semiconductor compound structures grown on InP substrates technologically useful for millimeter-wave applications. It was also found that the structure can be set either to highly conductive or nonconductive state within a given probing voltage region, which can be used as nonvolatile memories. A model device was proposed and demonstrated.[96] In the following, I will report these results in detail.

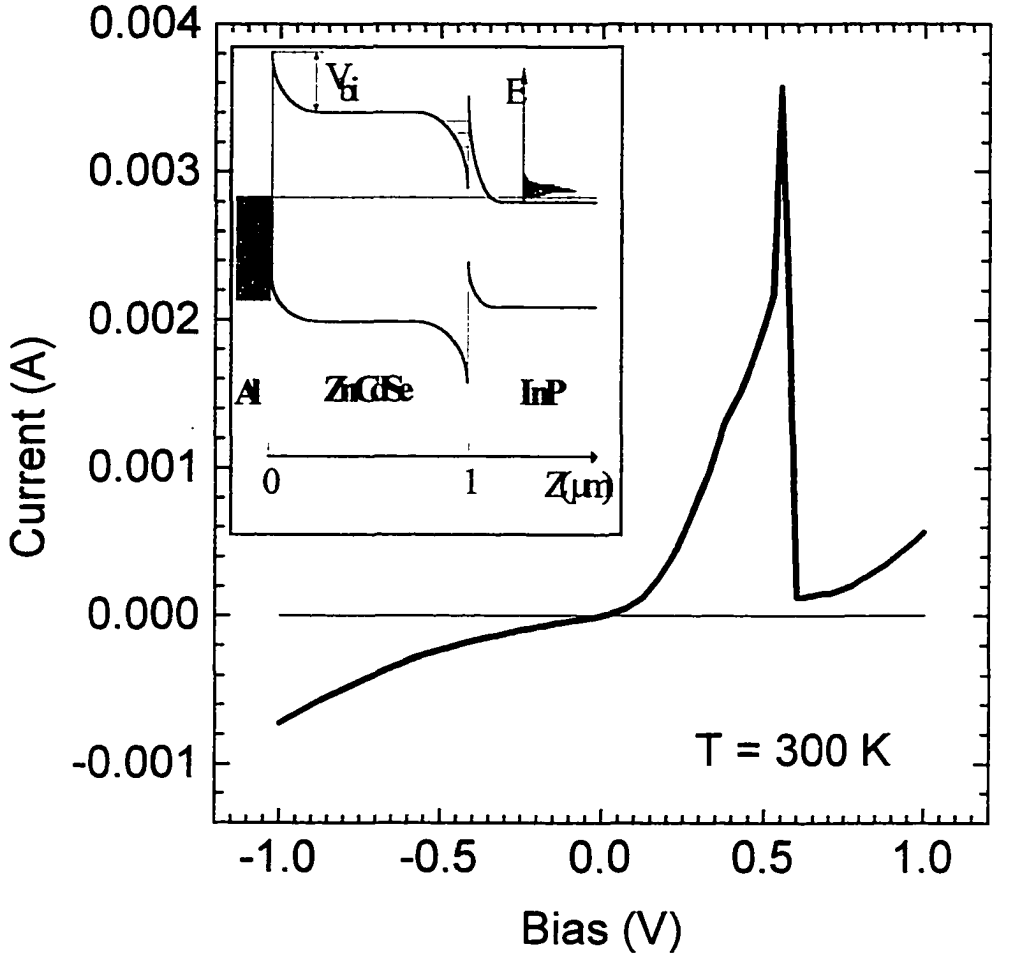

Figure 6-1. Current-voltage curve of the Al/ZnCdSe/InP device at room temperature. The inset is a sketch of the energy band diagram of the device structure.

6-1. Room temperature differential negative resistance in an $Al/Zn_{0.61}Cd_{0.39}Se/n^{+}$-InP device

In this section, we report on the current-voltage (I-V) characteristics of $Al/Zn_{0.61}Cd_{0.39}Se/n^{+}$-InP devices from 77 K to room temperature. These devices are based on the same structure described in chapter 4-3. For low temperature measurements, the device was placed onto the cool finger of a cryostat. The I-V data were taken by a computerized HP4142B source/monitor unit.

Figure 6-1 shows the I-V characteristics obtained from one of our devices measured at room temperature. Three features in this I-V curve can be observed. First, there is an obvious strong resonant peak at $V_p = 0.554$ V with a peak current value of $I_p = 3.57$ mA and a deep valley at $V_v = 0.605$ V with a valley current of $I_v = 0.12$ mA. The peak-to-valley current ratio ($\gamma = I_p / I_v$) is 30. This γ value determines the maximum output power and dc-to-ac conversion efficiency when the device is to be used for millimeter-wave application. This is a remarkably high value for this new resonant tunneling device in comparison with the γ value of 30 for the best studied double-barrier structure.[97] Another figure of merit for a tunneling diode is the speed index,

which is defined as the ratio of the peak current to the capacitance at the valley voltage, I_p / C_v. A large speed index is required for fast switching.[98] For the present device, the value for the speed of index is 0.01 mA/pF. This value is about three orders of magnitude smaller than that of a Ge Esaki diode. Since I_p / C_v is proportional to the conductivity of ZnCdSe layer, the speed of index can be substantially increased by intentional n-type doping of this layer.

Second, there appear to be two shoulders at 0.398 and 0.519 V in addition to the main resonant peak at 0.550 V. This feature is consistent with our previous C-V study in which three states (subbands) in the triangle quantum well near the hetero-interface of ZnCdSe and InP were observed. As schematically shown in the inset of Fig. 6-1, when the applied bias increases from 0 to 0.398 V, the population of electrons in the ground state increases from its equilibrium value. The electrons at the high energy tail in the ground state contribute to the measured current. As the bias increases from 0.398 to 0.519 V, the first excited state starts to contribute to the resonant current. When the bias further increases from 0.519 to 0.550 V, the second excited state plays an important role in the resonant current. When the bias exceeds 0.550 V the resonant current sharply dropped to the current valley since the conduction band edge of InP is above the second excited state.

Third, the I-V curve in the reverse bias region behaves as a leaky Schottky diode. The relatively large leakage current may arise from a significant number of threading dislocations due to a slight lattice mis-match between the ZnCdSe layer and InP substrate. This large leakage current may be reduced by more precisely controlling the alloy composition of ZnCdSe layer.

In order to gain a good understanding of the underlying mechanism of the observed DNR in our device, we measured the I-V curves at various temperatures as displayed in Fig. 6-2. For clarity, the I-V curve at 77 K is plotted in the inset of Fig. 6-2. The NDR did not appear until the device temperature was raised to above 145 K. This anomalous feature may be explained by the following two arguments. First, it may indicate that the electrons in the triangle quantum well that tunnel from the InP substrate do not elastically contribute to resonant current. A phonon-assisted process might be responsible for exciting electrons inside the triangle quantum well to the conduction band edge of ZnCdSe. This scenario is different from that in a conventional double-barrier structure in which phonon-assisted resonant tunneling contribution is small.[99] Second, the triangular quantum well may be not sufficiently populated by electrons when $T < 145$ K. Therefore, the resonant enhancement on current can not be observed.

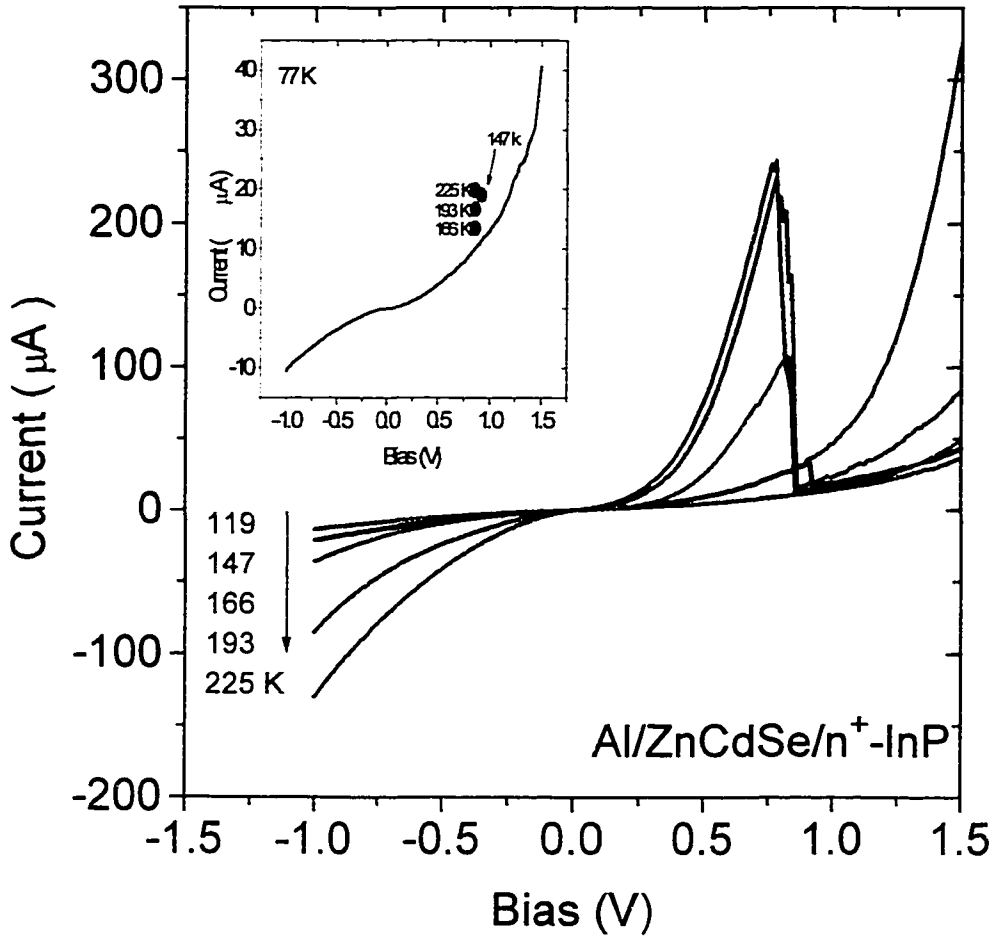

Figure 6-2. Current-voltage curves of the Al/ZnCdSe/InP device at various temperature.

Two additional observations can be made from the data in Fig.6-2. The reverse current at a given bias increases while the resonant peak position (V_p) decreases as the device temperature increases. The increase of reverse current at a given bias may arise from the increase of the thermionic emission current flow from the Al contact to the ZnCdSe epilayer. At this time, it is difficult to quantitatively explain how the V_p position shifts slightly to lower bias voltage as the device temperature increases. More precise modeling of the measured resonant current requires a self-consistent solution of the coupled Poisson's and Schrodinger's equations.

In summary, we have observed a strong NDR phenomenon in an Al/ZnCdSe/InP Schottky diode. At room temperature, the peak-to-valley current ratio is 30. This study suggests that it is feasible to fabricate useful resonant tunneling diodes based on ZnCdSe/ZnCdMgSe layer structures grown lattice-matched on n^+-InP substrates.

6-2. A novel concept for non-volatile memories

There are two main existing technologies for non-volatile memories. One is the floating gate technology which produces Electrically Erasable Programmable Read Only Memories (EEPROM) and Flash Memories (FM). The other is the ferroelectric capacitor based technology which yields

Ferroelectric Random Access Memories (FRAM). The proposed non-volatile memory cell in this study relies on an unique combination of a Schottky junction with tunable barrier height and an adjacent electron potential well. It has the following features: low operating voltage and current, no standby currents, direct fast overwrite capability, and integrable with high electron mobility InP or GaAs transistors and possibly with the main-stream Si transistors.

The proposed memory cell is based on a simple principle, which is to make a device to be either in highly conductive (on-state) or nonconductive state (off-state) within a given probing voltage region. Both states remain unchanged for extremely long periods of time even without an applied power. They can be changed from one state to the other and updated as the application requires it.

The approach to demonstrate the principle can be described using a *model* semiconductor device. The energy band diagrams of such a device in the off-state and the on-state are shown in Fig. 6-3(a) and (b), respectively. The device consists of six regions: metal contact, Schottky barrier, electron transport, electron potential well, hetero-interface barrier, and n^+-semiconductor substrate. As shown in Fig. 6-3(a), the reverse current (negative bias with respect to the substrate) is small since the image lowering

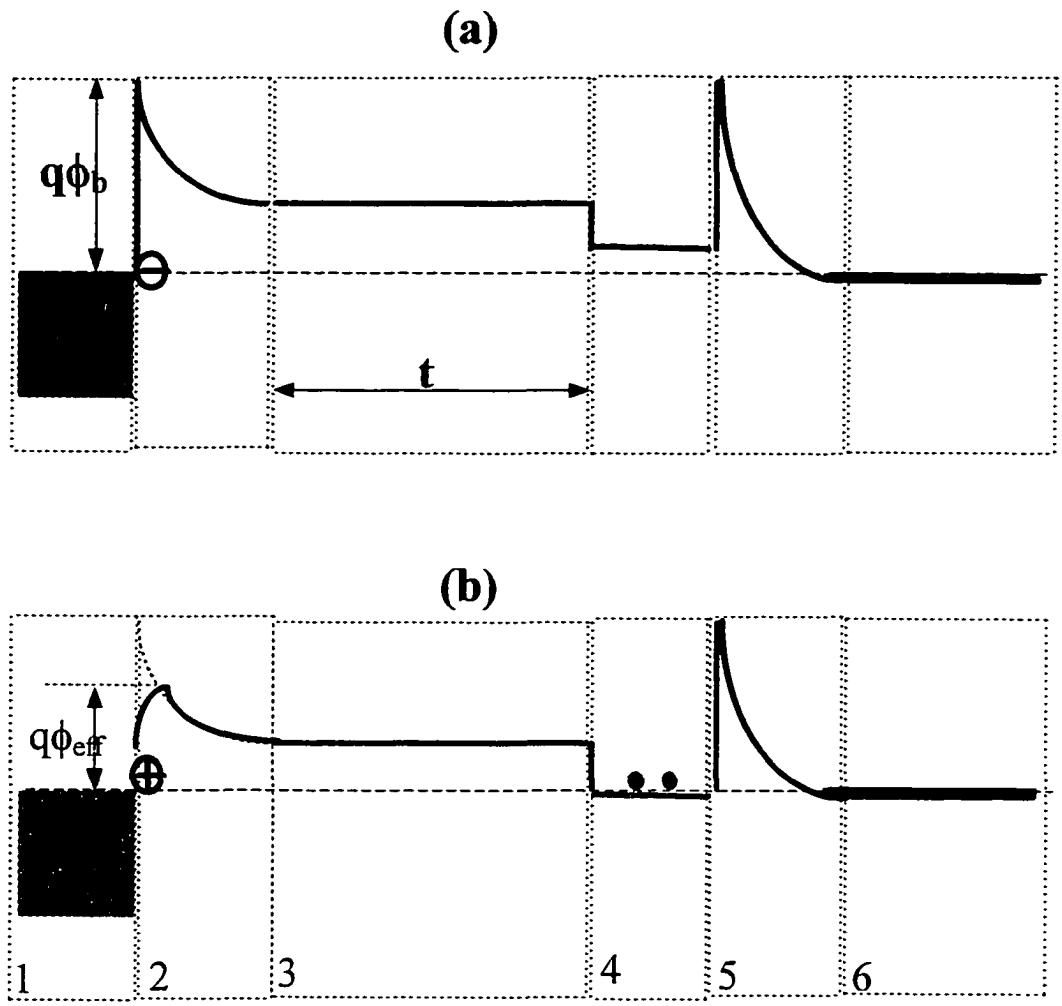

Figure 6-3. Conduction-band diagrams for the proposed model device for solid-state electrical memory cells, (a) in the off-state, and (b) in the on-state. The device consists of six regions: (1) metal contact, (2) Schottky barrier, (3) electron transport region, (4) electron potential well, (5) heterointerface barrier, and (6) n^+ -semiconductor substrate.

effect on the Schottky barrier height is negligible for ionized donor densities on the order of 10^{14} to 10^{15} cm^{-3} (unintentionally doped II-VI or III-V semiconductors). The forward current can be designed to be small by introducing a hetero-interface barrier near the interface of region 4 and 5. Therefore, both reverse and forward currents in off-state are small for a given probing voltage region (e.g., within ± 1 volt). The *model* device is in a non-conductive state.

To electrically turn the *model* device on from the off-state, we first discuss how one can electrically control the Schottky barrier height which is an energy barrier for injecting electrons from a metal contact to an adjacent semiconductor. A simplified expression for the image lowering potential energy is given by[100]

$$q\Delta\phi = 10.6\,[\mathbf{N_d}^+ \textit{(in } 10^{14}\ cm^{-3}) (\mathbf{V_b} - \mathbf{V_a}) \textit{(in volts)}]^{1/n} \textit{(meV)}, \qquad (6\text{-}1)$$

where the constant 10.6 is calculated using the value of 8.7 for the dielectric constant of the semiconductor $Zn_{0.61}Cd_{0.39}Se$ as an example, $\mathbf{N_d}^+$ is the ionized donor density, $\mathbf{V_b}$ is the built-in potential, $\mathbf{V_a}$ is the applied bias (negative under reverse bias), and the value of **n** depends on the assumption used for the space charge distribution (4 for an one-sided abrupt junction approximation). It is known that the reverse current of a Schottky diode at a

given temperature is *exponentially* dependent on the effective barrier height, $q\phi_{eff} = q\phi_b - q\Delta\phi$. The ingenuity of the proposed memory device is to make use of the tunable nature of a Schottky barrier height through the image lowering effect. As shown in the Eq.(1), the value of $q\Delta\phi$ can be turned on when $\mathbf{N_d}^+ \neq 0$ and be turned off when $\mathbf{N_d}^+ \approx 0$. DX centers[101] are useful for this application. They provide an electric-field-controlled source of ionized donors. When a critical reverse bias (e.g., V_n) is applied, two electrons for each DX center near the interface will be emitted to the conduction band and will drift away from the interface leaving behind a large number of normal ionized donors as indicated by a "+" sign in Fig.6-3(b). The condition of $\mathbf{N_d}^+ >> 0$ holds. This results in a large image lowering effect on the barrier height of the Schottky contact.

To turn the device on from the off-state, we can apply a negative bias slightly large than $|V_n|$ (dc or pulse) so that electrons located near the metal/semiconductor interface will be emitted to the conduction band and drift towards the electron potential well through the electron transport region and be confined there. As a result of this charge transport, both reverse and forward current will be increased. The increase of the reverse current is due to a smaller effective Schottky barrier height, $q\phi_{eff}$, caused by the image

lowering effect. The forward current increase is due to a resonant tunneling current enhancement arising from the confined electrons in the potential well as schematically shown by two filled circles in Fig. 6-3(b). It should emphasized that the novelty of the proposed memory device manifests itself from the fact that the electric field controlled electron emission from the DX centers causes an increase of *not only* the reverse current *but also* the forward current.

To turn the device off from the on-state, a critical positive bias V_p is required to release the electrons confined in the potential well. These electrons will be swept back to the metal/semiconductor interface and be captured by the ionized DX centers when the electron energy exceeds the capture energy barrier, E_c.

The *model* device is sustained either at the on-state or the off-state even when the external power is removed. For the on-state, the electrons left from the metal/semiconductor interface are confined in the electron potential well. The device will stay in the on-state as long as electrons remain confined. For the off-state, the electrons are released from the potential well and are captured by the charge centers near the metal/semiconductor interface. The device will stay in the off-state as long as the probing voltage is less than $|V_n|$, i.e., $|eV_n| < E_e$ (emission barrier height).

To demonstrate the proposed concept for non-volatile memories, we have measured more than 100 hetero-structure devices fabricated using 15 different wafers with different $Zn_xCd_yMg_{(1-x-y)}Se$/InP epilayer structures grown on n^+-InP substrates. The room temperature I-V data taken from a device (D13) fabricated from one wafer (A567) are displayed in Fig.6-4. The layer structure is Al/ZnCdSe(5nm)/ZnCdMgSe(0.75μm)/ZnCdSe(1nm)/InP(200 nm) /n^+-InP. The applied bias starts at -1.5 V and increases towards 1.5 V. The device is initially in a low resistance state. When the applied bias reaches slightly over 1 V, the current sharply jumps to a current value less than 1 nA as shown in the inset of the Fig.6-4. The device has made a transition from low to high resistance state. Moving continuously from ~ 1 to 1.5 V, the device stays at the high resistance state. The device remains at the high resistance state when the applied bias changes its moving direction from 1.5 toward -1.5 V. At about -1.5 V, the device switches back to the low resistance state. The device can be either in the on- or off-state even when the applied bias is removed. The value of the current at 0.75 V is 1.218 mA for the on-state and 0.242 nA for the off-state. This remarkable current difference between the on- and off-state with a ratio of 5 million at a given applied bias gives us a real possibility

to develop a new solid state electrical memory technology based on this type of bi-resistance devices. The value of V_n at which the device makes a transition from the off-state to the on-state is in a range of - 0.25 to - 2.5 V and the value of V_p at which the device makes a transition from the on-state to the off-state is in a range of 0.25 to 2 V. Both V_p and V_n depend on the detailed structure parameters and device temperature. It should be pointed out that the DX centers in the ZnCdMgSe layer are not intentionally doped. The Al atoms may have diffused into ZnCdMgSe and become the DX centers there.

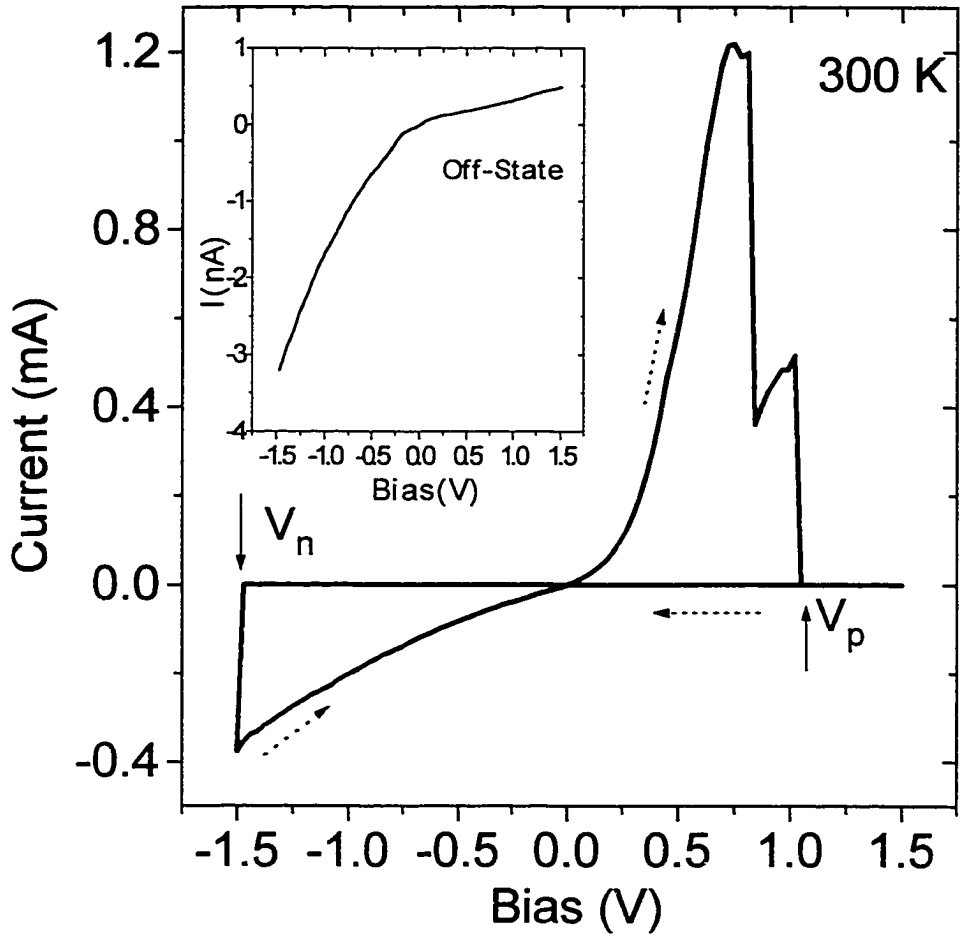

Figure 6-4. I-V curve of the Al/ZnCdSe(5 nm)/ ZnCdMgSe (0.75 μm/ZnCdSe (1 nm)/InP (200 nm)/InP (n^+) device at room temperature. The inset shows the I-V curve in the off-state.

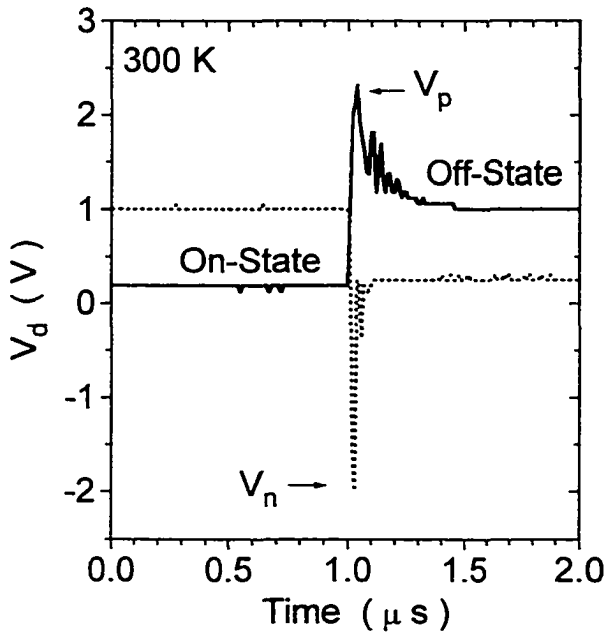

Figure 6-5. Transient switching profiles measured at room temperature. The solid curve is for the on-to-off switching while the dotted curve is for the off-to-on switching.

Preliminary transient experiments have been carried out to measure the speed of on-to-off and off-to-on switching for the device D13. A narrow electrical pulse with a width of ~100 ns was applied to the bi-resistance device which is in series with a normal resistor. The device voltage [V_d (t)] was measured as a function of time using a LeCroy digital oscilloscope. Fig.6-5 shows the transient switching profiles for on-to-off (solid-curve) and off-to-on (dot-curve) at room temperature. The value for V_n and V_p indicated in the figure is consistent with that measured in the dc case. A resolution limited short switching time of less than 100 ns was measured for the off-to-on transition. For the on-to-off transition, the switching time is about 100 ns. This on-to-off state transition time might be limited by the large device size. Although the number of on-to-off and off-to-on repetitions can be theoretically infinite for the

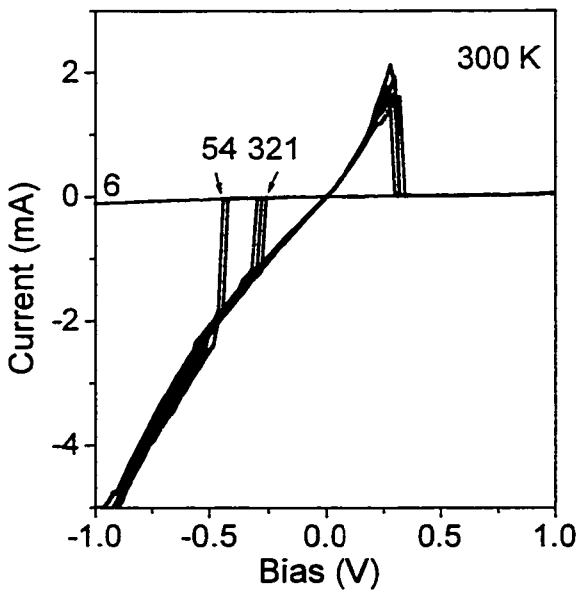

Figure 6-6. Continuously recorded I-V curves in a sequence of 1-6 for the Al/ZnCdSe/InP device at room temperature.

model device, the endurance for the current devices has not yet been fully characterized. For the limited data, we have found it is much easier to *continuously* repeat the I-V hysteresis for devices having smaller V_n and V_p values. Fig. 6-6 displays the continuously recorded I-V hysteresis (±1 V, current limit 5 mA) in a sequence of 1 to 6 at room temperature from another device (D5) fabricated from the A326 wafer with the layer structure of ZnCdSe(1.1 μm)/InP(100 nm)/n^+-InP. The variation of V_p is from 0.30 to 0.34 V while the variation of V_n is from - 0.25 to - 0.44 V for up to the 5^{th} repetition. At the 6^{th} repetition, the value of V_p exceeds the prefixed measurement limit of - 1 V resulting in the termination of hysteresis.

In summary, we have proposed a novel concept for non-volatile memory and presented a proof-of-concept demonstration using $Zn_xCd_yMg_{(1-x-y)}Se$ materials

grown on n^+-InP substrates. This study suggests that it is feasible to fabricate a new class of non-volatile memory cells based on our *model* device.

CHAPTER 7

SUMMARY

The main purpose of the research in my dissertation is to grow very high quality $Zn_xCd_yMg_{(1-x-y)}Se$ materials on InP substrates that will enable the design of an improved II-VI visible laser or emitter and to demonstrate the possibility to fabricate lasers or LEDs emitting in the entire visible range from such a single set of materials. The following is the summary of my work:

1. **Growth conditions of $Zn_xCd_yMg_{(1-x-y)}Se$ layers**

- We have constructed mathematical expressions to describe the dependence of bandgap and lattice constant on the compositions. From these expressions and using the bandgap data measured by PL and lattice constant evaluated from x-ray diffraction, we can calculate the compositions of $Zn_xCd_yMg_{(1-x-y)}Se$ layers grown. Conversely, this enables

us to predict the composition of the layer that will provide a desired bandgap and lattice constant.

- We have established and optimized the growth conditions for lattice matched $Zn_xCd_yMg_{(1-x-y)}Se$ materials with the desired bandgaps. In the optimized growth conditions, the incorporation of Mg affects the lattice constant only slightly, the lattice match condition is controlled mainly by the Cd to Zn flux ratio. The required bandgap is satisfied by changing primarily the Mg cell temperature.

2. **Quality improvements of $Zn_xCd_yMg_{(1-x-y)}Se$ materials**

- We have established a chemical etching technique to measure the defect density of $Zn_xCd_yMg_{(1-x-y)}Se$ materials. We found that a hydrobromic acid and acetic acid solution worked well for the etch pit density measurements of $Zn_xCd_yMg_{(1-x-y)}Se$ layers. The accuracy of the etchant for revealing stacking faults and dislocations was verified by plan-view TEM.
- The quality of $Zn_xCd_yMg_{(1-x-y)}Se$ materials has been improved dramatically by using a III-V buffer layer, Zn-irradiation, initial low temperature growth, a ZnCdSe interfacial layer and growth interruption. The defect density of $Zn_xCd_yMg_{(1-x-y)}Se$ materials has been reduced from 10^{10} cm^{-2} to

~ 5×10^4 cm^{-2}. The full width at half maximum (FWHM) of double crystal x-ray rocking curves has been reduced to ~ 50-70 arcsec.

3. **Properties of $Zn_xCd_yMg_{(1-x-y)}Se$ epilayers grown on InP substrates**

- We have measured double crystal x-ray rocking curves in both (400) and {511} reflections to evaluate the quality and strain state of $Zn_xCd_yMg_{(1-x-y)}Se$ epilayers. The results showed that our $Zn_xCd_yMg_{(1-x-y)}Se$ epilayers with 0.85 μm thickness and ~0.589% perpendicular lattice-mismatch $[(\Delta a/a_s)_\perp]$ are still pseudomorphic, which is a larger mismatch than typically tolerated. We propose that the material hardness may be enhanced by the high Mg content.
- We have performed PL measurements at various temperatures for a set of $Zn_xCd_yMg_{(1-x-y)}Se$ materials with Mg fraction ranging from 0 to 0.53 and obtained the dependence of bandgap on temperature, as well as donor binding energies.
- We observed quantum carrier confinement near the $Zn_{0.51}Cd_{0.39}Se$/InP heterointerface from capacitance voltage profiling. Type II band alignment for this interface was determined. The conduction band offset was estimated to be -102 meV.

4. **Red-Green-Blue (R-G-B) photo-pumped lasing from ZnCdMgSe/ZnCdSe QW laser structures**

- Nearly lattice matched ZnCdMgSe/ZnCdSe QW structures with various QW widths were grown on InP substrates with 10 K PL emission range from 2.307 to 2.960 eV. These QW structures could serve as the active region of entirely lattice-matched laser structures.
- Laser structures were grown that exhibit photo-pumped lasing with emission in the range from blue to red. The results demonstrate the potential for these materials as integrated full color display devices.
- Preliminary studies of the degradation behavior of ZnCdSe/ZnCdMgSe QW structures with and without strain in the QW layer were performed. No dark line defects (DLDs) were observed during the degradation for both cases. No relationship between strain and DLDs was observed for our structures.

5. **New applications of $Zn_xCd_yMg_{(1-x-y)}Se$ /InP system**

- Current voltage (I-V) measurements were performed on $Al/Zn_{0.61}Cd_{0.39}Se/n^+$-InP devices. A very strong room temperature

differential negative resistance behavior was observed, which is useful in millimeter-wave applications.

- It was found that the Al/$Zn_xCd_yMg_{(1-x-y)}Se$/n^+-InP devices can be set to either a highly conductive or a nonconductive state within a given probing voltage region, which can be used as nonvolatile memories. A model device has been demonstrated.

As a conclusion, the growth conditions for lattice matched $Zn_xCd_yMg_{(1-x-y)}Se$ materials with desired bandgaps have been established and optimized. The material quality has been improved significantly by using the techniques of III-V buffer layer, Zn-irradiation, low temperature growth, ZnCdSe interfacial layer and growth interruption. The defect density of $Zn_xCd_yMg_{(1-x-y)}Se$ materials has been reduced from 10^{10} cm^{-2} to ~ 5×10^4 cm^{-2}. We have demonstrated the optical pumped lasing at room temperature of a set of ZnCdSe/ZnCdMgSe based separate-confinement single-QW lasers grown lattice-matched to InP substrates that emit in the range covering the red, green and blue regions. We have also demonstrated other potential applications of this material system in microwave and memory devices.

CHAPTER 8

LIST OF PUBLICATIONS

1. JOURNAL PUBLICATIONS:

1. L. Zeng, Y. Guo, B. X. Yang, A. Cavus, W. Lin, Y. Y. Luo, Y. C. Chen, M. C. Tamargo, "Red-Green-Blue (R-G-B) optically pumped ZnCdMgSe/ZnCdSe lasers grown on InP substrates" submitted to Appl. Phys. Lett.
2. W. Lin, A. Cavus, L. Zeng, M. C. Tamargo, " N-type doping of lattice-matched ZnCdSe and ZnCdMgSe epitayers on InP using ZnCl", accepted to publish by J. Appl. Phys.
3. L. Zeng, B. X. Yang, M. C. Tamargo, E. Snoeks and L. Zhao, "MBE growth of highly improved ZnCdMgSe epilayers on InP substrates by incorporating a thin ZnCdSe interfacial layer", Appl. Phys. Lett. 72(11), 1317 (1998).
4. Kai Shum, J. Zhou, W. Zhang, L. Zeng and M. C. Tamargo, "A concept for nonvolatile memories", Appl. Phys. Lett. 71(17), 2487 (1997).
5. L. Zeng, B. X. Yang, I. Baryshev, M. C. Tamargo, J. Z. Wan, F. H. Pollak, E. Snoeks and L. Zhao, "Determination of defect density in ZnCdMgSe layers grown on InP using a chemical etch", J. Appl. Phys. 82(7), 3306 (1997).

6. Kai Shum, J. Zhou, W. Zhang, L. Zeng and M. C. Tamargo, "Room temperature differential negative resistance in an Al/ZnCdSe/n^+-InP device", Appl. Phys. Lett. 71(6), 815 (1997).
7. E. Snoeks, L. Zhao, B. Yang, A. Cavus, L. Zeng, and M. C. Tamargo, "Structural quality of pseudomorphic $Zn_{0.5}Cd_{0.5}Se$ Layers grown on an InGaAs or InP buffer layer on (001) InP Substrates", J. Cryst. Growth, 179, 83 (1997).
8. E. Snoeks, S. Herko, L. Zhao, B. Yang, A. Cavus, L. Zeng, and M. C. Tamargo, "Improvement in Quality of Epitaxial $Zn_{0.5}Cd_{0.5}Se$ Layers Grown on (001) InP Substrates by Using an InP Buffer Layer", Appl. Phys. Lett. 70(17), 2259 (1997).
9. Y. Guo, G. Aizin, Y. C. Chen, L. Zeng, A. Cavus, M. C. Tamargo, "Photo-pumped ZnCdMgSe/ZnCdSe Blue-Green Quantum-Well Lasers grown on InP", Appl. Phys. Lett. 70(11), 1351 (1997).
10. L. Zeng, A. Cavus, B. X. Yang , M. C. Tamargo, N.Bambha, A. Gray and F. Semendy, "Molecular Beam Epitaxial Growth of Lattice-Matched ZnCdMgSe Quaternaries on InP Substrates", J. Cryst. Growth, 175, 541(1997).
11. A. Cavus, L. Zeng, B. X. Yang , N. Dai, M. C. Tamargo, N.Bambha, A. Gray and F. Semendy, "Molecular Beam Epitaxial Growth of High Quality ZnCdSe Layers on InP Substrates", J. Cryst. Growth, 175, 558 (1997).
12. Kai Shum, L. Zeng, N. Dai and M. C. Tamargo, "Observation of quantum carrier confinement of near $Zn_{0.61}Cd_{0.39}Se$/InP heterointerface", Appl. Phys. Lett., 69(27), 4200(1996).

13. A. Cavus, L. Zeng, M. C. Tamargo, N.Bambha, F. Semendy and A.Gray, "ZnCdMgSe/ZnCdSe Quantum Wells on InP Substrates for Visible Emitters", Appl. Phys. Lett. 68(24), 3446 (1996).

14. M. C. Tamargo, A. Cavus, L. Zeng, N. Dai, N.Bambha, A. Gray, F. Semendy, W. Krystek and F. H. Pollak, "MBE Growth of Lattice-Matched ZnCdMgSe Quaternaries and ZnCdMgSe/ZnCdSe Quantum Wells on InP Substrates", J. Elect. Mater. 25, 259 (1996).

15. M. C. Tamargo, A. Cavus, L. Zeng, N. Dai, N.Bambha, A. Gray, F. Semendy, W. Krystek and F. H. Pollak, "Molecular Beam Epitaxial Growth of Lattice-Matched Wide Bandgap II-VI Alloys and Heterostructures on InP Substrates", in Semiconductor Heteroepitaxy: Growth, Characterization and Device Applications, editors B. Gil and R. L. Aulombard, World Scientific (1995).

16. W. Krystek, L. Malikova, F. H. Pollak, M. C. Tamargo, N. Dai, L. Zeng, A. Cavus, "Contactless electroreflectance study of temperature dependence of fundamental band gap of ZnSe", Vol. 88, Acta Physica polonica A, 1013(1995).

2. CONFERENCE PRESENTATIONS:

1. L. L. Chao, H. Xing, and G. S. Cargill III, L. Zeng and M. C. Tamargo, "Absence of Dark Line Defect Formation During the Degradation of ZnCdMgSe/ZnCdSe Quantum Well Structures on InP Substrate", Bulletin of the American Physical Society, vol. 43, No. 1, 718 (1998). APS March Meeting, Los Angeles, CA. March 16-20, 1998.

2. M. C. Tamargo, L. Zeng, B. X. Yang, "MBE growth of highly improved ZnCdMgSe epilayers on InP substrates by incorporating a thin ZnCdSe interfacial layer", 16th Annual North American Conference on Molecular Beam Epitaxy, Ann Arbor, Michigan, October, 1997.
3. L. Zeng, B. X. Yang, B. Shewareged, M. C. Tamargo, J. Z. Wan, F. H. Pollak, E. Snoeks and L. Zhao, "Etch Pit Density Characterization of ZnCdMgSe Grown on InP Substrates", 1997 Electronic Materials Conference, Fort Collins, Colorado, June, 1997.
4. L. Zhao, E. Snoeks, B. Greenberg, L. Zeng, B. X. Yang, A. Cavus, and M. C. Tamargo, "Effect of MBE Grown (ZnCd)Se Buffer Layer on the Structure of (ZnCdMg)Se Films Grown on (001) InP", Spring Meeting of the Materials Research Society, San Francisco, CA, March 31 - April 4, 1997.
5. L. Zeng, B. X. Yang, A. Cavus, M. C. Tamargo, Y. Guo, Y. C. Chen, "Photo-pumped Red, Green and Blue (R-G-B) ZnCdMgSe/ZnCdSe lasers grown on InP substrates", APS Match Meeting, Kansas city, 17-21 Match, 1997, Kansas city, MO.
6. L. Zeng, A. Cavus, B. X. Yang , M. C. Tamargo, Y. Guo, G. Ayzin, Y. C. Chen, N. Bambha, A. Gray and F. Semendy, "MBE Growth of Lattice-

Matched ZnCdMgSe Quaternaries on InP Substrates", International MBE-IX Conference, Malibu, California, Aug. 1996.

7. M. C. Tamargo, Y. Guo, L. Zeng, A. Cavus, B. Yang, G. Aizin, Y.C. Chen and N. Dai, "Lasing in ZnCdMgSe Structures Lattice-Matched to InP Substrates" 1996 Electronic Materials Conference, Santa Barbara, CA, June, 1996.

8. M. C. Tamargo, A. Cavus, L. Zeng, B. X. Yang, F. Semendy, A. Gray, N. Bambha, , E. Snoeks and L. Zhao, "Heteroepitaxial Growth of Wide Bandgap II-VI alloys on InP Substrates", Spring Meeting of the Materials Research Society, San Francisco, CA, April, 1996.

9. L. Zeng, A. Cavus, N. Dai, M. C. Tamargo, W. Krystek, F. H. Pollak, N. Bambha, and F. Semendy, "MBE Growth of ZnCdMgSe Quaternary Alloys and ZnCdMgSe/ZnCdSe Quantum Wells on InP Substrates", 1995 Electronic Materials Conference, Charlottesville, VA, June, 1995.

REFERENCES:

1. G. E. Thomas, Philips Tech. Rev. 44, No.2, 51 (1988).

2. Shuji Nakamura and Gerhard Fasol, The Blue Laser Diode, Springer (1997).

3. K. Koga, T. Yamaguchi, Prog. Crystal Growth and Charact. 23, 127 (1991).

4. S. Taniguchi, T. Hino, S. Itoh, K. Nakano, N. Nakayama, A. Ishibashi and M. Ikeda, Electron. Lett. 32, 552 (1996).

5. Shuji Nakamura et al, 2nd International Conference on Nitride Semiconductors, Tokushima, Japan, October 30, 1997. And *Nitride News*, Compound Semiconductor, Nov./Dec. 4 (1997).

6. M. C. Tamargo, A. Cavus, L. Zeng, N. Dai, N. Bambha, A. Gray, F. Semendy, W. Krystek and F. H. Pollak, in Semiconductor Heteroepitaxy: Growth, Characterization and Device Applications, editors B. Gil and R. L. Aulombard, World Scientific (1995).

7. M. C. Tamargo, A. Cavus, L. Zeng, N. Dai, N. Bambha, A. Gray, F. Semendy, W. Krystek and F. H. Pollak, J. Elect. Mater. 25, 259 (1996).

8. T. Morita, A. Kikuchi, I. Nomura, and K. Kishino, J. Elect. Mater. 25, 425 (1996).

9. K. Naniwae, H. Iwata, N. Kuroda, K. Yashiki, M. Kuramoto, T. Suzuki, J. Cryst. Growth. 159, 36(1996).

10. M. C. Tamargo, M. J. S. P. Brasil, R. E. Nahory, R. J. Martin, A. L. Weaver, and H. L. Gilchrist, Semicond. Sci. Technol. 6, A8 (1991).

11. F. S. Turco-Sandroff, R. E. Nahory, M. J. S. P. Brasil, R. J. Martin, R. Beserman, L. A. Farrow, J. M. Worlock and A. L. Weaver, J. Cryst. Growth 111, 762 (1991).

12. M. C. Tamargo, R. Hull, L. H. Greene, J. R. Hayes, and A. Y. Cho, Appl. Phys. Lett. 46, 569(1985).

13. A. Waag, The invited talk in the APS March Meeting, Kansas City, MO. 17-21 March, 1997.

14. E. Snoeks, L. Zhao, B. Yang, A. Cavus, L. Zeng, and M. C. Tamargo, J. Cryst. Growth, 179, 83(1997).

15. E. Snoeks, S. Herko, L. Zhao, B. Yang, A. Cavus, L. Zeng, and M. C. Tamargo, Appl. Phys. Lett. 70, 2259(1997).

16. N. Dai, A. Cavus, R. Dzakpasu, M. C. Tamargo, F. Semendy, N. Bambha, D. M. Hwang, and C. Y. Chen, Appl. Phys. Lett. 66(20), 2742 (1995).

17. A. Cavus, L. Zeng, B. X. Yang , N. Dai, M. C. Tamargo, N. Bambha, A. Gray and F. Semendy, J. Cryst. Growth, 175, 558(1997).

18. L. Zeng, A. Cavus, B. X. Yang , M. C. Tamargo, N. Bambha, A. Gray and F. Semendy, J. Cryst. Growth, 175, 541(1997).

19. L. Zeng, B. X. Yang , M. C. Tamargo, E. Snoeks, and L. Zhao, Appl. Phys. Lett. 72(11), 1317(1998).

20. A. Cavus, L. Zeng, M. C. Tamargo, N. Bambha, F. Semendy and A. Gray, Appl. Phys. Lett. 68(24), 3446 (1996).

21. Y. Guo, G. Aizin, Y. C. Chen, L. Zeng, A. Cavus , M. C. Tamargo, Appl. Phys. Lett. 70(11), 1351(1997).

22. L. Zeng, Y. Guo, B. X. Yang, A. Cavus, W. Lin, Y. Y. Luo, Y. C. Chen, M. C. Tamargo, submitted to Appl. Phys. Lett.

23. W. Lin, A. Cavus, L. Zeng and M. C. Tamargo, accepted to publish by J. Appl. Phys.

24. P. E. Luscher and D. M. Collins, Prog. Crystal Growth Charact. Vol. 2, 15(1979).

25. M. C. Tamargo, J. L. de Miguel, F. S. Turco, B. J. Skromme, M. H. Meynadier, R. E. Nahory, D. M. Hwang and H. H. Farrell, SPIE vol. 1037, 73 (1988).

26. A. Y. Cho and J. R. Arthur, Prog. Solid State Chem. 10, 157 (1975).

27. A. Y. Cho, J. Vac. Sci. Technol. 8, S31 (1971).

28. H. B. Bebb and E. W. Williams. In Semiconductors and Semimetals. Editors R. K. Willardson and A. C. Beers. Academic Press, vol. 8, 1972.

29. M. A. G. Halliwell: Prog. Crystal Growth and Charact. 19, 249 (1989).

30. Jacques I. Pankove, Optical Processes in Semiconductors, Dover Publications, Inc, 1975.

31. H. C. Casey, JR and M. B. Panish, Heterostructure Lasers, Academic Press, 1984.

32. H. Okuyama, K. Nakano, T. Miyajima, and K. Akimoto, J. Cryst. Growth, 117, 139(1992).

33. A. Kamata and H. Mitsuhashi, J. Cryst. Growth 142, 31 (1994).

34. T. Koyama, T. Yodo, H. Oka, K. Yamashita, and T. Yamasaki, J. Cryst. Growth 91, 639 (1988).

35. G. D. U'Ren, M. S. Goorsky, G. Meis-Haugen, K. K. Law, T. J. Miller, K. W. Haberern, Appl. Phys. Lett. 69(8), 1089 (1996).

36. C. C. Chu, T. B. Ng, J. Han, G. C.Hua, R. L. Gunshor, E. Ho, E. L. Warlick, and L. A. Kolodziejski, Appl. Phys. Lett. 69(5), 602 (1996).

37. L. Zeng, B. X. Yang , B. Shewareged, M. C. Tamargo, J. Z. Wan, Fred H. Pollak, E. Snoeks, and L. Zhao, J. Appl. Phys. 82, 3306 (1997).

38. K. Akita, T. Kusunoki, S. Komiya and T. Kotani, J. Cryst. Growth 46, 783 (1979).

39. Heinz K. Henisch, in Imperfections and active centers in semiconductors, the Macmillan, New York (1964) 321.

40. D. Li, and M. D. Pashley, J. Vac. Sci. Technol. B 12(4), 2547(1994).

41. S. Rouvimov, E. D. Bourret, J. Washburn, and Z. Liliental-weber, Appl. Phys. Lett. 68, 346 (1996).

42. B. J. Wu, J. M. DePuydt, G. M. Haugen, G. E. Hofler, M. A. Haase, H. chen, S. Guha, J. Qui, L. H. Kuo and L. Salamnca-Riba, Appl. Phys. Lett. 66, 3462 (1995).

43. H. H. Farrell, M. C. Tamargo, J. H. de Miguel, F. S. Turco, D. M. Hwang, and R. E. Nahory, J. Appl. Phys. 69, 7021 (1991).

44. S. Guha, H. Munekata, and L. L. Chang, J. Appl. Phys. 73, 2294(1993).

45. J. M. Gaines, J. Petruzzello, and B. Greenberg, J. Appl. Phys. 73, 2835 (1993).

46. G. J. Davies, R. Heckingbottom, H. Ohno, C. E. C. Wood, and A. R. Calawa, Appl. Phys. Lett. 37(3), 290 (1980).

47. R. F. C. Farrow, J. Phys. D. 8, L87 (1975).

48. K. Y. Cheng, A. Y. Cho, W. R. Wagner, and W. A. Bonner, J. Appl. Phys. 52, 1015 (1981).(22) D.E. Aspnes, M.C. Tamargo, M.J.S.P. Brasil, R.E.Nahory and S.A. Schwarz, Appl. Phys. Lett., 64, 3279 (1994).

49. B.X. Yang, L. He and H. Hasegawa, J. Elect. Mater., 25, 379 (1996).

50. D.E. Aspnes, M.C. Tamargo, M.J.S.P. Brasil, R.E.Nahory and S.A. Schwarz, Appl. Phys. Lett., 64, 3279 (1994).

51. G. Hollinger, D. Gallet, M. Gendry, C. Santinelli, and P. Viktorovitch, J. Vac. Sci. Technol. B8, 832 (1990).

52. T. B. Ng, C. C. Chu, G. C. Hua, J. Han, R. L. Gunshor, E. Ho, E. L. Warlick, L. A. Kolodziejski, and A. V. Nurmikko, presented at the Ninth International Conference on MBE, Malibu, 1996.

53. A. Madhukar, T. C. Lee, M. Y. Yen, P. Chen, J. Y. Kim, S. V. Ghaisas, and P. G. Newman, Appl. Phys. Lett. 46(12), 1148(1985).

54. D. Hull and D. J. Bacon, *Introduction to Dislocations*. International Series on Materials Science and Technology (Pergamon, Oxford, 1984), vol. 37.

55. M.C. Tamargo, J.L. de Miguel, D. M. Hwang, and H.H. Farrell, J. Vac. Sci. Technol., B6, 784 (1988).

56. L.H. Kuo, K. Kimura, T. Yasuda, S. Miwa, C. G. Jin, K. Tanaka and T. Yao, Appl. Phys. Lett., 68, 2413 (1996).

57. S. Guha, H. Munekata, and L. L. Chang, J. Appl. Phys. 73, 2294 (1993).

58. T. Morita, A. Kikuchi, I. Nomura, and K. Kishino, J. Elect. Mater. 25, 425 (1996).

59. J. M. Gaines, J. Petruzzello, and B. Greenberg, J. Appl. Phys. 73, 2835 (1993).

60. C. C. Chu, T. B. Ng, J. Han, G. C. Hua, R. L. Gunshor, E. Ho, E. L. Warlick, and L. A. Kolodziejski, Appl. Phys. Lett. 69(5), 602 (1996).

61. J. Qiu, Q.-D. Qian, R.L. Qunshor, M. Kobayashi, D. R. Menace, D. Lie and N. Oust, Appl. Phys. Lett., 56, 1272 (1990).

62. A. Segmüller, I. C. Noyan, V. S. Speriosu: Prog. Crystal Growth and Charact. 18, 21 (1989).

63. A. T. Macrander, G. P. Schwartz, and G. J. Gualtieri, J. Appl. Phys. 64, 6733 (1988).

64. Lev I. Berger, Semiconductor Materials, PP 190, CRC Press, 1997.

65. P. J. Dean, P. J. Wright and B. Cockayne, J. Phys. C: Solid State Phys., 16, 3493 (1983).

66. E. Hal Bogardus and H. Barry Bebb, Phys. Rev. 176, 993 (1968).

67. P. J. Dean, Phys. Rev. 157, 655 (1967).

68. P. J. Dean, D. C. Herbert, C. J. Werkhoven, B. J. Fitzpatrick, and R. N. Bhargava, Phys. Rev. B23, 4888 (1981).

69. W. Krystek, L. Malikova and F. Pollak, M. C. Tamargo, N. Dai, L. Zeng, A. Cavus, Acta Physica Polonica A, 88, 1013 (1995).

70. L. Malikova, W. Krystek, F. Pollak, N. Dai, A. Cavus and M. C. Tamargo, Phys. Rev. B54(3), 1819 (1996).

71. S. Logothetidis, M. Cardona, P. Lautenschlager and M. Garriaga, Phys. Rev. B34, 2458 (1986).

72. P. Lautenschlager, M. Garriaga, S. Logothetidis, and M. Cardona, Phys. Rev. B35, 9174 (1987).

73. A. S. Nasibov, P. V. Shapkin, J. V. Korostelin, J. A. Vlasov, L. S. Markov, A. I. Maslov, and D. L. Fedorov, Solid State Communications, v78, 521 (1991).

74. S. D. Baranovskii and A. L. Efros, Sov. Phys. Semicond. 12(11), 1328 (1978).

75. A. S. Nasibov, Yu. V. Korostelin, P. V. Shapkin, L. G. Suslina, D. L. Fedorov and L. S. Markov, Solid State Communications, 71, 867 (1989).

76. D. L. Fedorov, S. A. Permogorov, A. S. Nasibov, P. V. Shapkin, and Yu. A. Korostelin, Phys. Solid State 35, 1065 (1993).

77. Kai Shum, L. Zeng, N. Dai, and M. C. Tamargo, Appl. Phys. Lett. 69(27), 4200 (1996).

78. O. Thomas, D. Kahng, and R. C. Manz, J. Electrochem. Soc., 109, 1055 (1962).

79. E. F. Schubert, R. F. Kopf, J. M. Kuo, H. S. Luftman, and P. A. Garbinski, Appl. Phys. Lett., 57, 497 (1990).

80. J. Rennie, Y. Nishikawa, S. Saito, M. Onomuta, and G. Hatakoshi, Appl. Phys. Lett., 68, 2971 (1996).

81. H. -J. Gossmann and E. F. Schubert, Criti. Rev. in Solid State and Materials Sci. 18(1), 1 (1993).

82. Y. Wu, K. Ichino, Y. Kawakami, S. Fujita, and Sg. Fujita, Jpn. J. Appl. Phys. 31, 3608 (1992).

83. The composition (x) of the active $Zn_xCd_{(1-x)}Se$ layer in ZnCdSe/ZnMgSSe based laser structures is ~ 0.8. By using Vegard's law and the lattice constants of ZnSe (5.667 Å) and CdSe (6.076 Å), the lattice-constant of the active layer can be obtained to be 5.749 Å, which means the lattice-mismatch of the active layer to GaAs substrates is ~ 1.7%.

84. C. A. Zmudzinski, Y. Guan, and P. S. Zory, IEEE Photonics Technol. Lett. 2, 94 (1990).

85. J. M. Gaines, R. R. Drenten, K. W. Haberern, T. Marshall, P. Mensz, and J. Petruzzello, Appl. Phys. Lett. 62, 2462 (1993).

86. H. Okuyama, F. Hiei, and K. Akimoto, Jpn. J. Appl. Phys. 31, L340 (1992).

87. M. A. Hasse, J. Qiu, J. M. DePuydt, and H. Cheng, Appl. Phys. Lett. 59, 1272 (1991).

88. S. Guha, H. Cheng, M. A. Hasse, J. M. DePuydt, J. Qiu, B. J. Wu, and G. E. Hofler, Appl. Phys. Lett. 65, 801 (1994).

89. M. Hovinen, J. Ding, A. Salokatve, A. V. Nurmikko, G. C. Grillo, L. He, J. Han, M. Ringle and R. L. Gunshor, J. Appl. Phys. 77, 4150 (1995).

90. K. Nakano, S. Tomiya, M. Ukita, H. Yoshida, S. Itoh, E. Morita, M. Ikeda, and A. Ishibashi. J. Electron. Mater. 25, 213 (1995).

91. J. Petruzzello, K. Haberern, S. Herko, T. Marshall, S. Guha, G. U'Ren, and G. M. Haugen, J. Cryst. Growth 159, 573 (1996).

92. L. L. Chao, G. S. Cargill III, and C. Kothandaraman, T. Marshall, E. Snoeks, M. Buijs, K. Haberern, and J. Petruzzello, G. M. Haugen and K. K. Law, Appl. Phys. Lett. 70 (5), 535 (1997).

93. L. L. Chao, H. Xing, and G. S. Cargill III, L. Zeng and M. C. Tamargo, Bulletin of the American Physical Society, vol. 43, No. 1, 718 (1998). APS March Meeting, Los Angeles, CA. March 16-20, 1998.

94. Kai Shum, J. Zhou, W. Zhang, L. Zeng, and M. C. Tamargo, Appl. Phys. Lett. 71, 815 (1997).

95. R. Tsu, L. Esaki, and L. L. Chang, Appl. Phys, Lett. 22, 562 (1973).

96. Kai Shum, J. Zhou, W. Zhang, L. Zeng, and M. C. Tamargo, Appl. Phys. Lett. 71, 2487 (1997).

97. E. R. Brown, T. C. L. G. Sollner, C. D. Parker, d. W. Goodhue, and C. L. Chen, Appl. Phys. Lett. 55, 1777 (1989).

98. S. M. Sze, *Physics of Semiconductor Devices*, 2nd ed., Wiley, New York, 1981.

99. W. Cai, T. F. Zheng, P. Hu, B. Yudanin, and M. Lax, Phys. Rev. Lett. **64**, 418 (1989).

100. Sheng S. Li, *Semiconductor Physical Electronics*, Plenum Press, New York, 1993, ISBN 0-306-44157-8.

101. P. M. Mooney, J. Appl. Phys. 61, R1 (1990).

IMAGE EVALUATION TEST TARGET (QA-3)

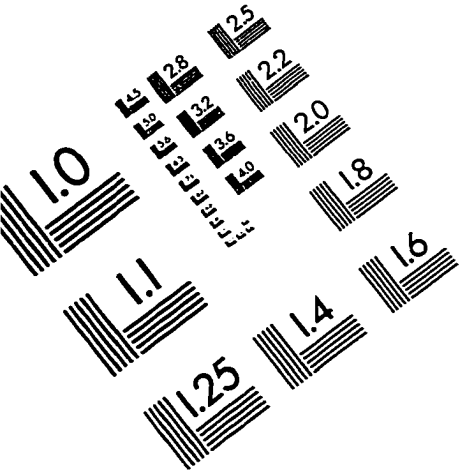

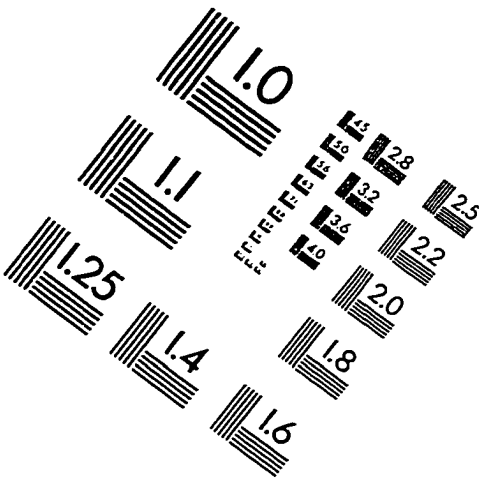

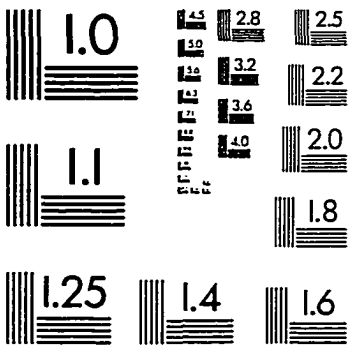

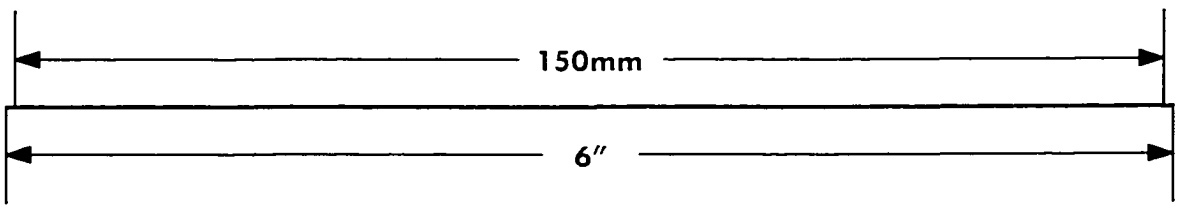

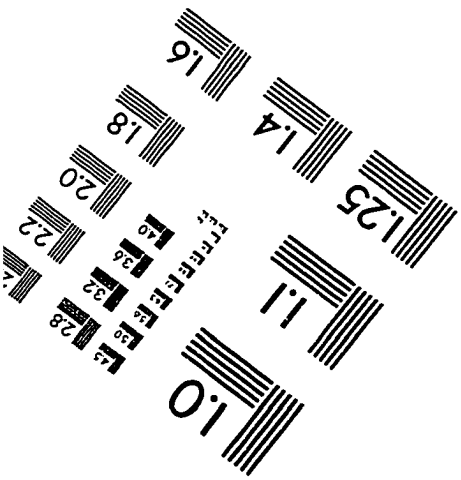

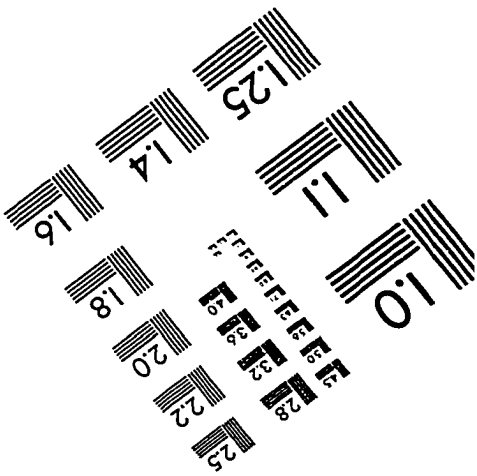

APPLIED IMAGE, Inc
1653 East Main Street
Rochester, NY 14609 USA
Phone: 716/482-0300
Fax: 716/288-5989